Resin-gel synthesis and characterisation of copper and titanium mixed metal oxides nanoparticles

University of the Witwatersrand, Johannesburg

Farai Dziike Mutambara

Supervised by Dr P. J. Franklyn

FEBRUARY 2013

RESIN-GEL SYNTHESIS AND CHARACTERISATION OF COPPER AND TITANIUM MIXED METAL OXIDE NANOPARTICLES

Farai Dziike Mutambara

Degree of Master of Science by research only:

A Dissertation submitted to the Faculty of Science, School of Chemistry, University of Witwatersrand in fulfillment of the requirements for the degree of Master of Science.

Johannesburg 2014

Declaration

I declare that this Dissertation is my own, unaided work. It is being submitted for the Degree of Master of Science at the University of the Witwatersrand, Johannesburg. It has not been submitted before for any degree or examination at any other University.

_____

_____day of _____2014

Abstract

The resin-gel method of synthesis successfully produced compounds of mixed metal oxides of copper titanium oxide powders of the form $Cu_xTi_yO_Z$ with different compositions. These include Cu_3TiO_5, Cu_3TiO_4, Ti_3Cu_3O, Cu_2Ti_4O, $Cu_2Ti_2O_5$ and Cu_2TiO_3. Heat-treatment of the powders at 300°C, 500°C, 700°C and 900°C for 1 hour was performed to determine the full composition/temperature phase diagram. The target particle size was in the 10-nanometer range, and for most of the samples, this size was achieved. Powder x-ray diffraction and transmission electron microscopy were the main techniques used to study the crystallization of these materials and their transformation to other polymorphic phases under different temperatures. Phase-match, particle size analysis and TEM imaging determined the properties and characteristics of the respective crystallographic phases of these materials. TEM analysis showed that some powders agglomerated while others exhibited both regular and irregular morphologies and polydisperse particle size distribution. Only a single unique phase was identified, but its structure could not be determined.

This project is dedicated to my dearest wife and sweetheart Betty and our little boy, Augustus Bill who came into this world on March 27, 2012.

Acknowledgements

For his prudent and intelligent ideas, encouragement, patience, motivation, persistence and unwavering support, I extend my heartfelt thanks and sincere gratitude to Dr P. J. Franklyn. The time he dedicated and the immense assistance he gave saw me through this research work to successful completion. I greatly appreciate the financial assistance extended to me in times of need through his initiatives.

I also extend many thanks to Prof. Dave Billing for his resourcefulness, patience and tolerance in making it possible for me to have uninterrupted access and use of the XRD D5000 for extended periods. Thanks to Wilson and Mitchelle for technical assistance, Natsai who assisted with the interpretation of Eva data and my colleagues in the catomat group who assisted in various ways.

Contents

Declaration iii
Abstract iv
Acknowledgements vi
List of tables vii
Symbols and Abbreviations viii
Chapter 1: Introduction 1
1.1 Titanium dioxide 2
1.2 Copper oxide 4
1.3 Polymorphism 5
1.4 Synthesis Methods in Nanoscience and Nanotechnology 11
1.4.1 Sol-gel method 11
1.4.2 Co-precipitation method 12
1.4.3 Microemulsion method 12
1.4.4 Solid-State Reaction (SSR) method. 13
1.4.5 Colloidal Emulsion method 13
1.4.6 Hydrothermal Synthesis method. 14
1.4.7 The Pechini Method 15
1.5 Aims and Objectives 19
1.6 Project Justification 20
1.7 The Scope of the Research 20
Chapter 2: Experimental 21
2.1 Synthesis of Titanium-Copper-Oxides (TCO) 21
2.2 Sample treatment and Analyses 24
Chapter 3: Results and Discussion 28
3.1 PXRD Analysis 28
3.1.1 Trends in peak patterns 28
3.1.2 Effect of percentage composition on peak patterns 37
3.1.3 Effect of Temperature variation on Peak Patterns 38
Chapter 4: Results and Discussion 68
4.1. Particle Size Analysis 68
4.2. Phase Purity 75
Chapter 5: Results and Discussion 78
5.1. Transmission Electron Microscopy (TEM) Analysis 78
Chapter 6: Conclusion 91
Chapter 7: Further Research 93
References 95

List of tables

Table 1. 1: Common synthesis methods of titanium dioxide and resultant phases. 8
Table 2. 1: Values calculated for percentage ratios of Ti to Cu……....24

Symbols and Abbreviations

TCO	Titanium copper oxides
CA	Citric acid
PEG	Polyethylene glycol
nm	nanometers
Psi	pound per square inch
Å	Angstrom
EDTA	Ethylene diamine tetra acetic acid
CuAc	Copper acetate
PVC	Polyvinyl chloride
AA	Absolute alcohol
BEST	Barium europium strontium titanate
PXRD	Powder X-ray diffractometer
TEM	Transmission Electron Microscope
HRTEM	High Resolution Transmission Microscope
SEM	Scattering Electron Microscope
hcp	Hexagonally close packed
fcc	Face-centered cube
PST	Lead strontium titanate

Chapter 1: Introduction

Mixed-metal oxides have been synthesised using a wide range of methods. During the past few decades, several wet chemical, non-conventional methods have found extensive uses in the synthesis of nanosized particles. Methods such as sol-gel, self-propagating high-temperature synthesis and hydrothermal techniques serve as alternatives to dry mixed-oxides synthesis.[1] Pechini-type *in situ* polymerizable complex methods are well known and widely used for the preparation of homogeneous bulk multi-component metal oxides such as $Li_xTi_2(PO_4)_3$, $(Ba,Sr)TiO_3$ and $Pb_xTi_ySr_2O_X$.[2;3]

The use of water-soluble ammonium citratoperoxotitanate (*IV*) metal complex instead of alkoxides as a precursor allows the preparation of monophase material.[1;4] Metal-metal oxides mostly involving titanium have been synthesised by conventional solid-state reaction methods that require high temperatures (~ 1200°C) for very long times (24 hr)[5;6] and result in the obvious loss of some precursor metals. Sol-gel routes with metal alkoxides as starting precursors prepared fine powders and thin films of lithium titanium phosphate (LTP), barium strontium titanate (BST) and lead titanium strontium oxide (PTS).[7] However, this route and other methods involving water as a solvent, pose a serious disadvantage involving some metals, in that the metal alkoxides are extremely sensitive to moisture, showing high reactivity towards hydrolysis, which affects the hydroxylation process.[2;7]

The Pechini method includes a combined process of metal complex formation and *in situ* polymerization. An α- hydroxycarboxylic acid such as citric acid (CA) is used to form stable complexes and their polyesterification with a polyhydroxy alcohol such as ethylene glycol (EG) which forms a polymeric resin.[8] This polymeric resin serves to immobilise the metal complexes in rigid organic polymer networks and reduce segregation to ensure compositional homogeneity. Calcination of the polymeric resin may generate pure multi–component phases of metal oxides. The method eliminates the element of moisture and the

consequential effect of high reactivity of some precursor metals towards hydrolysis. The Pechini-type polymerisable complex method gives provisions for controlling the viscosity and the molecular weight of the polymer by simply varying the ratio of the α-hydroxycarboxylic acid to the polyhydroxy alcohol and the synthetic temperature. This in turn has a direct effect on the size of the nanoparticles produced.[9] An adaptation of the Pechini method is that of resin-gel, where the polymer is included directly, making for less complex reaction conditions during synthesis.

In this work, the resin-gel method of synthesis has applications in the synthesis of titanium-copper-oxide nanoparticles. This method is a modification of the common Pechini-type in-situ polymerisable complex method. Resin-gel involves coordination of metal complexes with polyethylene glycol (PEG) to form a polymeric resin leading to possible mixtures with pure multi-component metal oxide phase at many different metal ratios. Titanium and copper are transition metal elements with incomplete d sub-shells. The cations also have incomplete d sub-shells in ionic reactions. These elements are in period four of the periodic table, referred to as 3d-transition metals and are known for their characteristic properties, including ferromagnetism and low dielectric constant. [10]

1.1 Titanium dioxide

Titanium (Ti) is an element with atomic number 22. It is a transition metal characterized by low density, luster and corrosion-resistance and has a silver color.[11] Titanium is a dimorphic allotrope with a hexagonal alpha form changing into a body-centered cubic beta lattice form at 882°C.[12] Ti occurs naturally as a mineral. Ilmenite ($FeTiO_3$) is widely recovered by heating TiO_2 or ilmenite with Cl_2 and carbon to produce $TiCl_4$ in a reaction,

$$TiO_2 + 2C + Cl_2 \rightarrow TiCl_2 + 2CO.$$

Titanium chloride is reduced using either sodium or magnesium to give pure titanium and the chloride salts as follows:

$$TiCl_2 + 4Na \rightarrow Ti + 4NaCl$$

$$TiCl_2 + 2Mg \rightarrow Ti + 2MgCl$$

Titanium resembles platinum in its chemical resistance and has an ability to withstand attack by dilute sulphuric acid and hydrochloric acid, as well as chlorine gas, chloride solutions and most organic acids. In concentrated acids, titanium is readily soluble to form titanium salts.[12] Titanium readily forms an oxide in air to give titanium dioxide (TiO_2) which acts as a protective oxide coating, a property used in corrosion resistance. This oxide layer is initially 1-2 nm thick and continues to thicken slowly up to 25 nm in about four years.[13] Figure 1.1 below shows the structure of TiO_2.

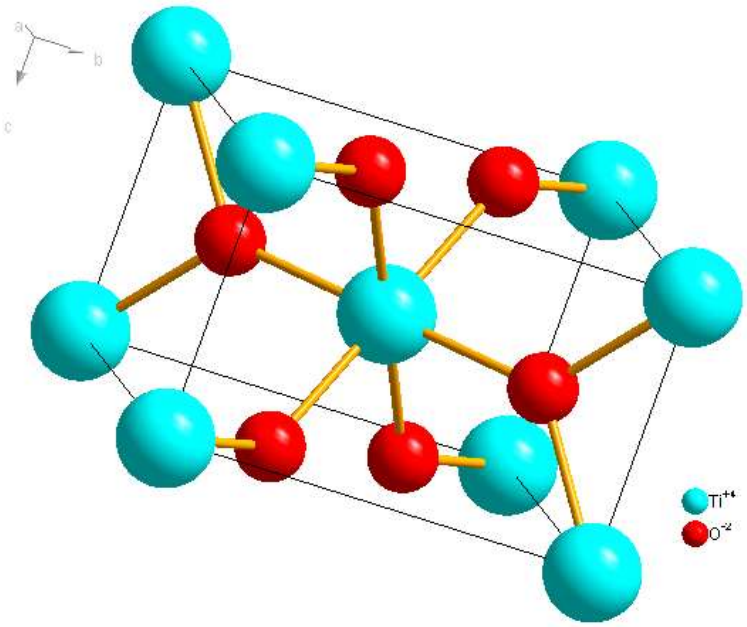

Figure 1.1: Geometry of titanium *(IV)* oxide solid-state structure.[14]

Titanium is characterised by a high tensile strength of about 63 000 psi that is equal to the tensile strength of some steel alloys but up to 45 % lighter. Titanium is 60 % more dense but more than twice as strong as the commonly used aluminium alloy. At temperatures above 450°C titanium loses strength, becomes brittle, paramagnetic, and has low electrical and thermal conductivity.[14]

Ti does not melt in open air because it combusts before the melting point is reached to form titanium dioxide. It follows that titanium can only melt in a

vacuum. For example, it burns in pure nitrogen gas at 800°C to form titanium nitride, rendering it a brittle material.[15] Titanium occurs naturally as an oxide called titania (TiO_2). Titania exists naturally in different polymorphic phases, with rutile, anatase and brookite the three most common. The rutile titanium (*IV*) oxide occurs most abundantly and has a crystalline structure as shown in Figure 1.1 above. This material has a high refractive index and is extensively used in paints, paper pigments, sunscreens and plastics to increase their whiteness and opacity.[16]

1.2 Copper oxide

Copper occurs naturally as sulphide compounds. The principal ores of copper are chalcopyrite ($CuFeS_2$) and copper glance (Cu_2S). Extraction of copper from its ore is by a two-step reaction. The first step is the heating of the impure copper (l) sulphide in air so that part of it reacts to form copper (l) oxide.

$2Cu_2S + 3O_2 \rightarrow 2Cu_2O + 2SO_2$

The copper oxide has crystalline structure as shown in Figure 1.2 below.

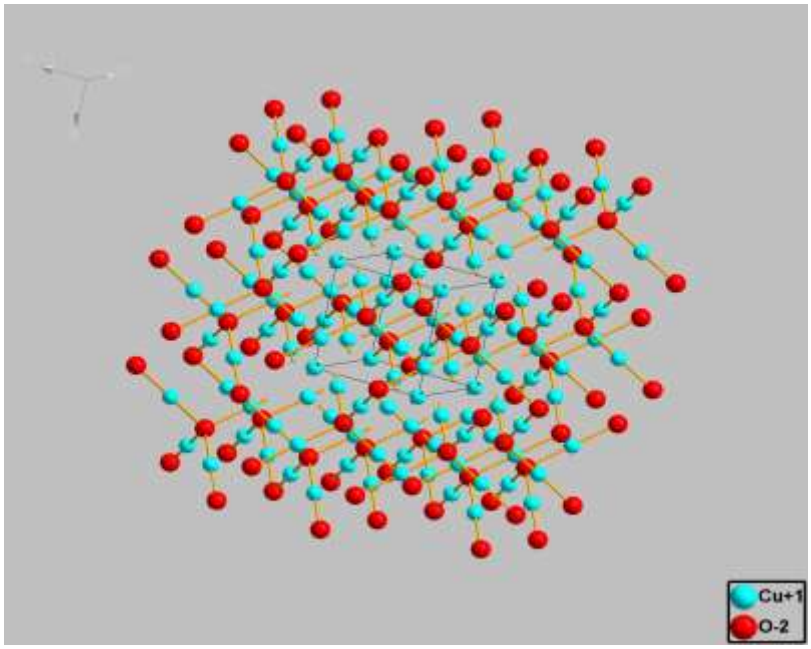

Figure 1.2: Crystalline structure of copper *(I)* oxide showing orientation of copper ions with respect to oxygen ions.

The copper *(I)* oxide, mixed with copper *(I)* sulphide is then strongly heated in the absence of air to form copper and sulphur dioxide.[14]

$$2Cu_2O + Cu_2S \rightarrow 6Cu + SO_2.$$

Copper is malleable and ductile, shows thermal and electrical conductance, and marked resistance to corrosion and has the ability to form alloys.[17]

1.3 Polymorphism

This is the observation that a given material may adopt different crystal forms, under different conditions of pressure and temperature. It follows that transition metals show several solid-solid phase transitions as they are heated and the atoms adopt a new packing arrangement. It is often found that the most closely packed phases are thermodynamically favored at low temperatures and the less closely packed structures are favored at high temperatures. Thus, polymorphism is a common consequence of the low directionality of metallic bonding.[17] Figure 1.3.1 below shows this phenomenon in cuprous oxide and how it comes into effect at different temperatures.

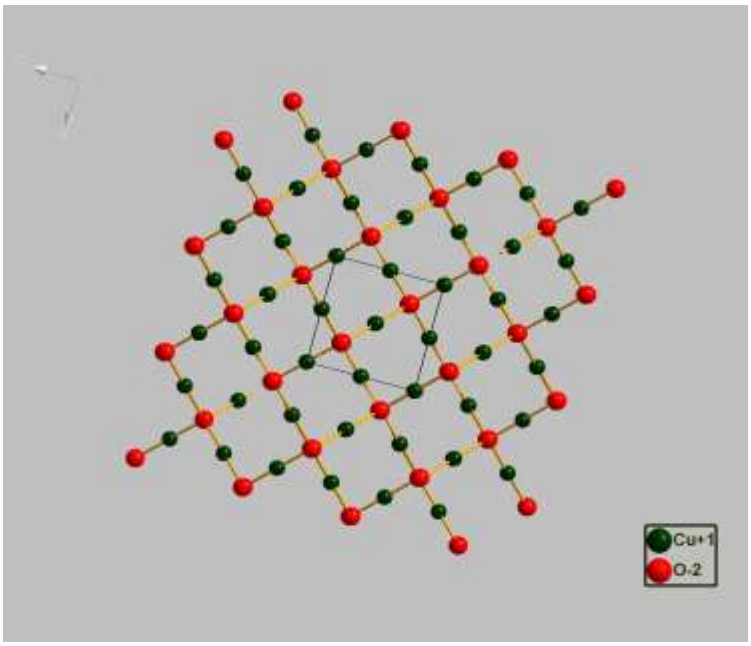

Figure 1. 3: Drawing of cuprous oxide (Cu_2O) structure type emphasizing the relation to antiflourite structural type and the extended lattice demonstrating the diamond like lattice connectivity.[18]

Polymorphism is principally applicable in describing characteristic structures of ionic solids. Many of the polymorphic structures are derived from the arrays in which the anions or cations stack together in face-centered cubes (fcc) or hexagonally-close packed (hcp) patterns. Their respective counterions occupy the

octahedral or tetrahedral holes in the lattice.[14] The structures used to describe crystallographic phases of ionic solids include the antiflourite, cesium chloride, fluorite, nickel arsenide, perovskite, rock salt, rutile, sphalerite, anatase, brookite and wurtzite crystal structures. These structures are named after the prototypes of the substances that give their names to the structure.[19] For example, rutile takes its name from a mineral form of TiO_2 and its unit cell is as shown in Figure 1.4 below.

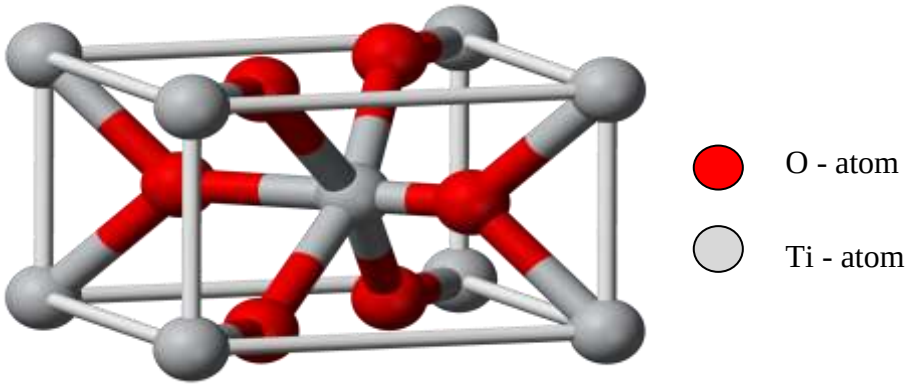

Figure 1. 4: Rutile - unit cell 3d – balls of titanium *(IV)* oxide.[20]

Rutile is an example of an hcp anion lattice with the cations occupying only half the octahedral holes as represented in Figure 1.5 below.

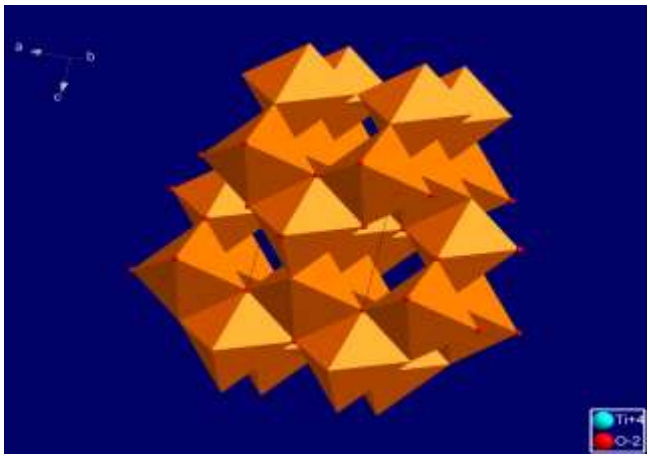

Figure 1. 5: Rutile hexagonal close packing showing each ti atom surrounded by six O atoms and each o atom surrounded by three Ti atoms.[17]

The perovskite structure takes its name from $CaTiO_3$ hence used to describe solids of the general form ABX_3 such as $BaTiO_3$ and $SrTiO_3$ [21] as shown in Figure 1.6 below.

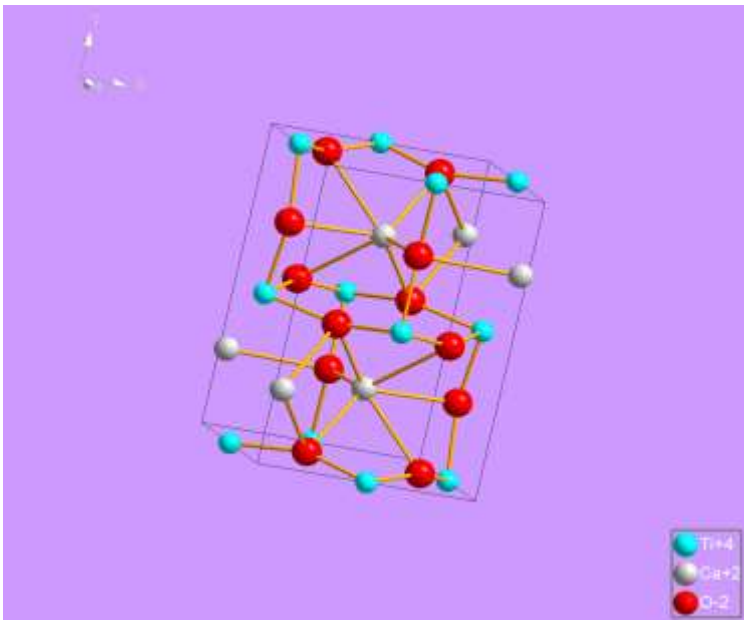

Figure 1. 6: The perovskite cubic structures with the ca atoms surrounded by 12 O atoms and the b atoms surrounded by 6 Ti atoms as shown in .[21]

In this research, the characterisation process seeks to determine the crystallographic phases of the mixed metal oxides of titanium and copper. Several studies determined the various parameters that affect crystal structure transformations and the nature and magnitude of their effects.[22] Detailed studies on titanium oxide polymorphs investigated the systematic transformation of pure metastable anatase (tetragonal) to the more stable rutile (tetragonal) and the transformation of brookite (orthorhombic) to rutile. Figure 1.7 below shows the rutile and anatase crystal structures. Anatase transforms irreversibly to rutile at elevated temperatures. This transformation does not have a unique temperature and the processes that are involved in the transformation as well as the methods to inhibit or promote this transformation are still under comprehensive study. The transformation of anatase to rutile is a reconstructive transformation involving changes in secondary coordination.[23] This implies that from a structural perspective, this could be due to the greater ease of the short-range ordered TiO_6 octahedra in arranging into long-range ordered anatase structure, owing to the less-constrained molecular construction of anatase relative to rutile. Alternatively, from a thermodynamic perspective, the more rapid recrystallization of anatase could be due to the lower surface free energy of this polymorph, despite the lower Gibbs free energy of rutile.[24] That is, the higher surface free energy of rutile

crystallites may favour the crystallisation of anatase. It should be noted that it is possible to form rutile under near room temperature conditions.[25; 26; 27; 28] Hydrothermal methods of synthesis, which can facilitate the precipitation of crystalline TiO_2 directly from a liquid phase, can be controlled to precipitate rutile. Aside from this method, rutile is obtained only through high-temperature treatment. Table 1 below summarizes the phases that can result from various synthesis methods at room temperature and at elevated temperatures.

Synthesis method	**Mechanism**	**Phases formed**				**References**
		Amorphous	**Anatase**	**Rutile**	**Anatase + rutile**	
Room temperature hydrolysis of $TiCl_4$	Precipitation from room temperature solutions of $TiCl_4$	✓				[85, 86]
Room temperature sol–gel synthesis	Hydrolysis of $TiCl_4$ or an organo-metallic compound	✓				[87–90]
Flame pyrolysis of $TiCl_4$	Combustion of $TiCl_4$ with oxygen; used in industrial processes		✓		✓	[91–93]
Solvothermal/ hydrothermal	Precipitation of TiO_2 from aqueous or organic solution at elevated temperatures		✓	✓	✓	[66, 84, 94–99]
Chemical vapor deposition	Spraying of Ti-bearing solution	✓	✓	✓	✓	[100, 101]
Physical vapor deposition	Deposition of evaporated Ti and its subsequent oxidation	✓	✓	✓	✓	[21, 102]

Table 1. 1: Common synthesis methods of TiO_2 and resultant phases.[24]

Accompanying these polymorphic transformations are changes in particle size, crystallite size, surface area and lattice dimensions. These characteristics are subject to the method of synthesis and temperature variation.[24, 25] It was found that

stabilities of the TiO_2 polymorphs, the kinetics of their phase transformation, and the processes involved in controlling them is essential to the ability to obtain single-phase or multiphase microstructures. An increase in temperature gave rise to growth of particles. Anatase powder heated for a period of 3hrs at 400, 600, 800 and 1000°C saw marked increases in particle size in the 600-1000°C region. This was also accompanied by decrease in surface area and a transformation to rutile as samples were heated to higher temperatures.[26, 27, 28, 29]

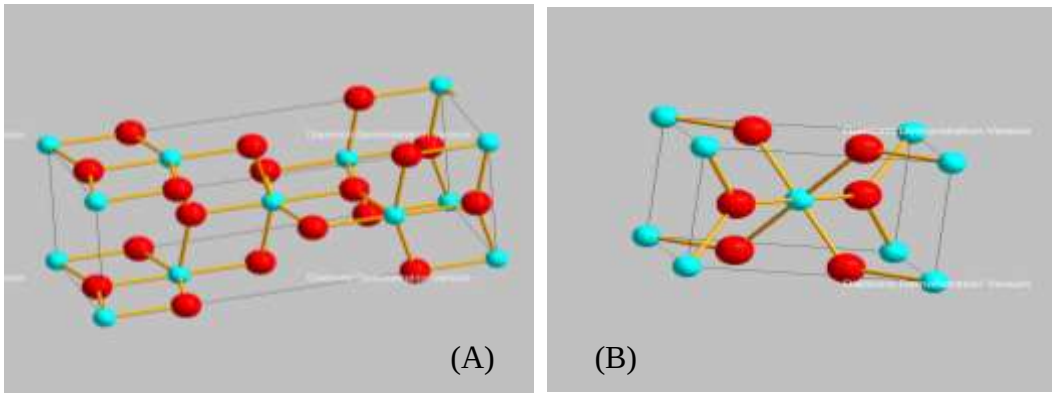

Figure 1.7: Polymorphic transformation of anatase (A) to rutile (B)[30]

Rutile and anatase are two polymorphic structures of TiO_2 based on distorted close-packed or eutectic anion arrays. The rutile structure assumes a tetragonal variant of the orthorhombic $CaCl_2$ structure [31]. This arrangement allows the possible ways of filling half of the octahedral holes of a hexagonal close - packed array of oxide ions to give a system with the MO_2 stoichiometry. Three metal atoms in a distorted trigonal-pyramidal geometry coordinate the oxide ions. The rutile transformation leads to a structure where these pyramids have become rigorously planar with a unique O-Ti-O angle of about 99^0. Hence, the metal octahedra are not regular, and four short and two long Ti-O distances occurred, irrespective of the temperature of the structural determination.[32]

The anatase structure exhibits a cubic close-packed array of oxide ions. The manner of distortion around the Ti atom is similar to that of rutile TiO_2 sustainable mostly at low temperatures. The octahedron in anatase shares four edges compared to the two in rutile. Consequently, there are short O-O distances in both polymorphs susceptible to changes under greater thermal expansion. It

follows that the rutile and anatase structures are regarded as frameworks built from oxygen-oxygen struts such that the smaller expansion of the shared O-O edges than the unshared ones produces the observed anisotropy.[30,31]

Copper *(I)* oxide is called cuprous oxide or cuprite (Cu_2O) which appears either yellow or red depending on the size of the particles. The copper centers are 2-coordinated and the oxides are tetrahedral as shown in Figure 1.8 below. The structure thus resembles the main polymorphs of SiO_2 and both structures feature interpenetrated lattices.[20, 32] Cu_2O crystallises in a cubic structure with a lattice constant a_1 = 4.2696 Å. The Cu atoms arrange in a fcc sub-lattice, the O atoms in a bcc sub-lattice. The unit cell contains 4 Cu atoms and 2 O atoms with one sub-lattice shifted by a quarter of the body diagonal.[21]

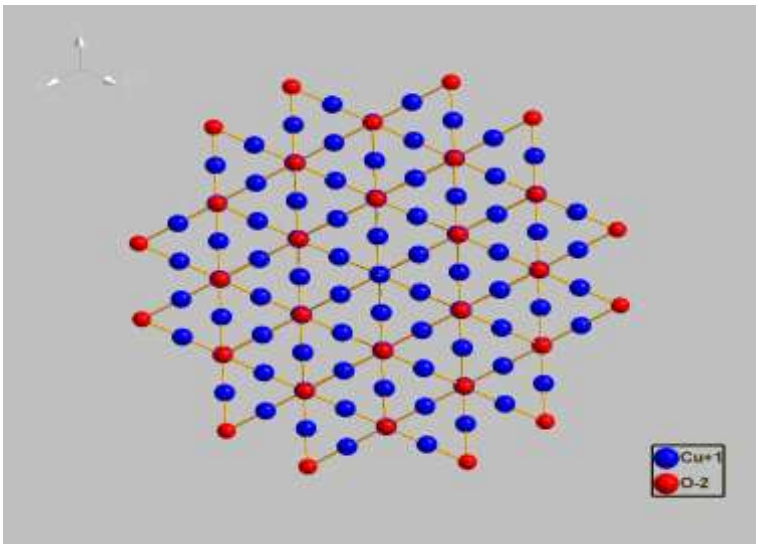

Figure 1. 8: Cuprous oxide (Cu_2O)[21] crystalline phase.

Copper (II) oxide is called cupric oxide (CuO) and is the higher oxide of copper. As a mineral, it is known as tenorite. This structure belongs to the monoclinic crystal system with a crystallographic point group of 2/m. The Cu-atom is coordinated by 4 O-atoms in an approximately square planar configuration.[14]

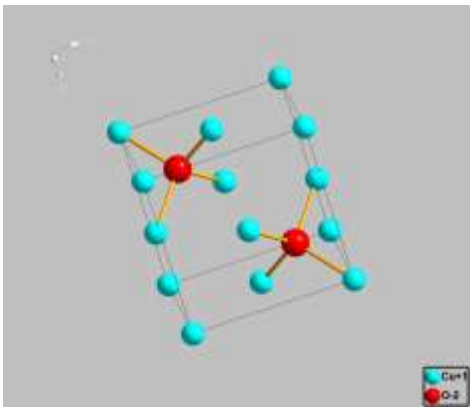

Figure 1. 9: The unit cell of copper *(II)* oxide [20, 21,32]

1.4 Synthesis Methods in Nanoscience and Nanotechnology

Nanoscience and nanotechnology are quickly advancing and the synthesis of nanoparticles has seen a wide range of modifications in the methods used to prepare them. Conventional methods of synthesis of nanoparticles include wet chemical methods. These include sol-gel, co-precipitation, hydrothermal, colloidal emulsion technique, microemulsion, solid- state reaction, chemical vapor decomposition, reversed micelle and solvothermal methods.[1;3] The methods presented complications that prompted a shift from their use as synthetic methods in nanoscience and nanotechnology.[15] The following sections discuss these methods of synthesis as a basis for justifying and understanding the need to modify them or use alternative methods in the synthesis of nanoparticles.

1.4.1 Sol-gel method

This method begins with the formation of a liquid solution of suspended reagents (a sol) that is aged and dried to form a semi-solid suspension of particles in a liquid (a gel), that is finally calcined, resulting in a mesoporous solid or powder. There are four distinct steps to the sol-gel technique. The formation of the gel initiates the technique. The aging to fine-tune the gel properties follows this. Thirdly, the drying to remove the solvent from the gel and the calcination to set the physical and chemical properties of the solid.[1] The sol-gel technique was used as an alternative method of preparation of lithium titanium phosphate ($LiTi_2$

$(PO_4)_3$ shortened LTP as a fine powder and thin film with metal alkoxides as starting precursors.[2] However, the alkoxides were prone to extreme moisture sensitivity and high reactivity towards hydrolysis and LTP transformed to multiphase compound at high temperatures. This phenomenon rendered sol-gel technique non-ideal in the synthesis of the LTP nanoparticles.[2;3] This is a significant problem with sol-gel, as it is suitable only over a narrow range of conditions.

1.4.2 Co-precipitation method

This is a wet-chemical synthetic route used to prepare nano-sized particles. This route allows a good mixing of starting components for the benefit of achieving homogeneity and the possibility of reaching lower formation temperatures.[3] The success of this route depends on the nature of salts and precipitants as well as synthesis conditions. In the synthesis of yttrium aluminum garnet (YAG), ammonium hydrogen carbonate exceeded ammonia and urea for the production of less agglomerated, well sinterable YAG nanopowders via co-precipitation.[13] However, the carbonate precursor loosely agglomerated. In order to reduce this agglomeration of the powder, dispersing agents such as sodium dodecyl sulfate, polyethylene glycol, hydroxyl propyl cellulose and ammonium sulfate were added.[5;11] Washing with ethanol only led to less agglomeration than washing with both water and ethanol. The strict control of synthesis parameters, especially pH values during precipitation and aging, is crucial for the production of pure phases of nanoparticles in co-precipitation synthesis.[3] Again this technique is suitable only for a narrow range of metal compositions.

1.4.3 Microemulsion method

A novel microemulsion technique involves dissolving one of the reactants in the continuous organic phase in an aqueous solution of the second reagent. For example, crystalline titanium oxide nanoparticles of two different phases (rutile and anomalous pseudobrookite) were prepared from a microemulsion technique.[13] Rutile TiO_2 formed in the aqueous core. The reaction in the organic phase gave rise to crystalline anomalous pseudobrookite TiO_2 nanoparticles.[10]

The latter is thermally unstable and converts to rutile on high temperature treatment.[7] Water-in-CO_2 microemulsion was also used to alternatively prepare titanium dioxide nanoparticles, as CO_2 is non-toxic, non-flammable, highly volatile, relatively inexpensive and environmentally manageable. Microemulsion provide a micro-heterogeneous medium for the generation of nanoparticles. The surfactant–stabilized micro-cavities provide a cage-like effect that influences particle nucleation, growth and agglomeration.[10]

1.4.4 Solid-State Reaction (SSR) method.

This involves the mixture and reaction of solid metal carbonates, nitrates or phosphates at high heat temperatures (>1000°C) for long processing times until reactants form new products at different phases and stoichiometric combinations.[2] The products formed are powders of particles. Lithium titanium phosphate (LTP) was prepared using the general solid-state reaction (SSR) method to explore the ion dynamics and their potential use in various applications due to their grain interior high ionic conductivity at room temperature.[2;12] Similarly; Lead-Strontium titanate nanoparticles were also prepared by the SSR method.[11] This involved the mixture and reaction between $PbCO_3$, or PbO, $SrCO_3$ and TiO_2 at a high temperature to form (Pb, Sr) TiO_3 powders.[13] However, these powders obtained by this method present several problems such as undesirable stoichiometry, contamination by impurities and polydisperse particle size distribution.[15]

1.4.5 Colloidal Emulsion method

This method is similar to the generation of nanoparticles in the chemical co-precipitation method. However, it involves the addition of a capping agent that allows for size control of the nanoparticles and prevents agglomeration of the nanoparticles.[19] It follows that any molecule that adsorbs onto the nanoparticles has the potential to act as a capping agent. The experimental procedure is a simple combination of the metal source, a reducing agent, and a capping agent put together in a mixing.[11] Bimetallic and other colloidal nanoparticles can be

prepared by co-reduction. The colloidal synthesis method has been successfully tailored to allow for particle size and composition control, as well as shape control.[1;16] The problem with colloidal emulsion is that it is suitable only over a narrow range of conditions.

1.4.6 Hydrothermal Synthesis method.

Known more generally as solvothermal synthesis, hydrothermal synthesis has been used extensively in the preparation of pure ceria and titania.[5] This is largely because the solvothermal reactions are necessary to give fine control over crystal growth in which precipitation at room temperature gives smaller particles, and these particles show a range of sizes and shapes.[32] The hydrothermal and solvothermal approach is based on the use of aqueous and or organic additives such as ethylene diamine tetra acetic acid (EDTA), polyethylene glycol (PEG) and sodium dodecyl sulfate (SDS) introduced into the reaction and refluxed with or without pressure to manipulate the nucleation and growth in hydrothermal and solvothermal reactions.[34]

The two-step method enabled synthesis of ZnO nanopowders. Initially, a zinc nitrate aqueous solution mixed with ammonium carbonate (precipitating agent) and stirred thoroughly, produced precursor powders of metal oxides. The metal oxides are added to a cetyltriethylammonium bromide (CTAB) aqueous solution. NaOH was introduced to adjust the *pH* value of the solution. This was then reacted at 220°C in an oven for 18 hrs.[35] It not effective in mixed metal oxide synthesis as the method allows the element of moisture and the consequential effect of high reactivity of the precursor metals towards hydrolysis.

1.4.7 The Pechini Method

This method has recently found a widespread use in the preparation of nanoparticles as an alternative to the conventional methods of synthesis some of which are highlighted above.[15] The Pechini method is a useful powder preparation technique used in the fabrication of highly dispersed mixed oxides or oxide solid solutions of perovskite, spinels and garnets for their ability of certain weak α-hydroxycarboxylic acids to form polybasic acid chelates.[17] This method has been modified in its use in the preparation of a wide range of nanoparticles. It follows that the Pechini method can be described as an *in-situ* polymerizable complex method that offers substantial advantages over any other method used in the synthesis of nanoparticles.[19]

The Pechini-type method has an advantage in that it allows the formation of several oxides with good stoichiometric control and small particle size in the study of structural and morphological characteristics of nanopowders with different compositions.[20;21] The modified Pechini method allows a molecular mixing of constituents leading to a good chemical homogeneity, an increase in the rate of reaction and a decrease of the temperature of crystallisation. It also produces high purity nanoparticles.[14;33]

The Pechini method is also widely used for the preparation of pure mixed oxide nanopowders due to the low costs of precursors, low synthesis temperature and ionic homogeneity at molecular level. It ensures good reproducibility in the properties of the ceramic.[34] This method proceeds via two reactions involved in the preparation process.[35] Firstly, there is formation of a complex between an organic acid, such as citric acid or EDTA, with the precursor metals. This is followed by the esterification reaction with ethylene glycol. The polymeric organic net produced by the esterification reaction is to reduce any segregation of the cations.[36] This technique has been used in the synthesis of many ceramic nanoparticles and materials. The synthesis of these materials varied in the organic acid, esterification alcohol and the desirable precursor metals used.

Barium-strontium titanate (BST), (Ba, Sr)TiO_3 solid solution was formed as nanopowders by Pechini method from titanium isopropoxide, barium and

strontium carbonates, using citric acid as a chelating agent and ethylene glycol as an esterification agent. PXRD patterns for the BST showed single-phase composition for all the samples.[37] Similar studies were conducted on the preparation of lithium titanium phosphate (LTP), $LiTi_2$ $(PO_4)_3$ material[2], to explore the ionic dynamics and their potential use in various applications due to their grain interior high ionic conductivity at room temperature. The LTP was prepared using the Pechini-type in situ polymerizable complex method. This involved the use of water-soluble ammonium citratoperoxotitanate (*IV*) metal complex, which is highly stable in water. This study revealed that the main function of the CA and EG is to provide a polymeric network to hinder cation mobility that maintains local stoichiometry and minimizes precipitation of unwanted phase. [12]

Citric acid (CA) improves the uniform distribution of the cations in both solution and resin. The EG increases the potential heat of combustion produced during calcination. It follows that the smallest particle size is obtained when the CA/Ti ratio is small. This phenomenon arises when cations are close to each other and when cation diffusion is not necessary to induce chemical reaction. The lower the molar ratio EG/CA, the higher was the rate of crystallite growth. The best ratio to obtain pure and nanosized particles are CA/Ti = 1 and EG/CA = 1 and to maintain a particle size smaller than 100 nm, the calcination temperature has to be lower than 1000°C.[8]

Lead titanate is another ceramic oxide of interest characterized by unique ferroelectric, dielectric and luminescent properties with a tetragonal structure at room temperature. The ferroelectric material exhibits a low dielectric constant, high pyroelectric coefficient and strong spontaneous polarization. However, the large tetragonal strain and high Curie temperature on the material limit its industrial use. This drawback was overcome by doping $PbTiO_3$ with different lanthanides and alkaline earth metals. Strontium was used to partially replace Pb atoms to give lead strontium titanate (PST), (Pb, Sr) TiO_3 powders.[13]

The PST powders were prepared by solid-state reaction (SSR) at high temperatures. This method presented several problems including undesirable

stoichiometry, contamination by impurities and polydisperse particle size distribution. For this reason, the Pechini-type method was used, due to its advantages for the formation of several oxides with good stoichiometric control and small particle size. The PST nanoparticles were studied for structural and morphological characteristics of the order of (Pb_{1-x} Sr_x) TiO_3 powders with different compositions. Patterns from the XRD showed diffraction peaks corresponding to pure $PbTiO_3$ phase. Peaks with Sr content up to x = 0.1 were indexed to the perovskite- type tetragonal structure.[13,38] Ethylenediaminetetraacetic acid (EDTA) was used as a chelating agent in a Pechini-type method of preparation of barium europium titanate (BET) ceramic powders with formula: $yBa_{6-3x}Eu_{8+2x}Ti_{18}O_{54}$.

The crystallisation behavior was determined together with the microstructure characterisation of the ceramics and its microwave properties were explained by its crystal structure. Barium europium strontium titanate (BEST), ceramic powders were synthesised via the EDTA-gel route. The gel was composed of EDTA dissolved in ammonium hydroxide solution, to which butyl titanate was added gradually with continuous stirring. The solution was heated at 80°C on a hot plate and nitric acid was added to the stirred solution to adjust the pH to 4. The PXRD results show that the single crystal lattice type of the BEST powders prepared by the sol-gel route belongs to the orthorhombic system and its phase transformation is a function of temperature. Compared with the conventional solid-state reaction process, a Pechini-type method produced two phases of BEST ceramic powders formed at a lower temperature and crystallized without any other lattice.[39]

Europium-lanthanum oxide (Eu-La_2O_3) nanoparticles were prepared using the modified. The procedure involved dissolution of the Eu_2O_3 in hot ammonia to generate $Eu(NO_3)_3$. This was mixed with La $(NO_3)_3.6H_2O$ and dissolve in distilled water. EDTA was added to the solution with a molar ratio = 1. Ethylene glycol was added with a molar ratio = 2 while stirring and heating the solution. The precursor resin generated was calcined at 573K for 3hrs to obtain the precursor powders. The precursor powders were further calcined at different

temperatures between 573 and 1273K in air for 2hrs to obtain nanocrystals of Eu:La_2O_3.

The crystalline structure of the nanocrystals was analyzed by powder x-ray diffraction. Detailed studies revealed that precursor powders are amorphous when calcined at temperatures in the range of 573 – 773K. The XRD result showed parameters smaller than those of pure La_2O_3. The decrease in the unit cell parameters is attributed to the introduction of Eu in the structure of the crystals since the ionic radius of Eu is smaller than that of La in a 7-fold oxygen coordination.[40] Metal titanates based oxides including metals such as Ni, Co, Zn, Cu and Pb are universally known as inorganic functional materials with many diverse applications.[26] These compounds have an ilmenite structure in a trigonal system. The ilmenite structured materials prefer octahedral coordination with alternating cation layers occupied by metal and Ti alone as in $NiTiO_3$ and $CoTiO_3$.[41]

Synthesis using the conventional solid state reaction in the preparation of $NiTiO_3$ and $CoTiO_3$ requires high temperature treatment over 1000°C for an extended period until intermediate phases disappear.[42] However standard methods of mechanically mixing oxides and or carbonates followed by calcination and ball milling are not adequate for many advanced applications.[43] There are problems with poor sintering behavior, non-homogeneity and inaccurate control of cation ratios and stoichiometry. This method also leads to large strong powder agglomerates, undesirable phases, abnormal grain growth and poor reproducibility.[44] A modified Pechini method was used to synthesise these ilmenite powders with the aim of preparing fine powders with good distribution. These fine powders revealed particularly optical and electrical properties in comparison with bulk material.[6]

$NiTiO_3$ and $CoTiO_3$ powders were prepared along a synthetic procedure as summarised in Figure 1.4.7 below.

Citric acid + Ethanol	Titanium (IV) n-butoxide + ethanol	Ni / Co acetate + ethanol

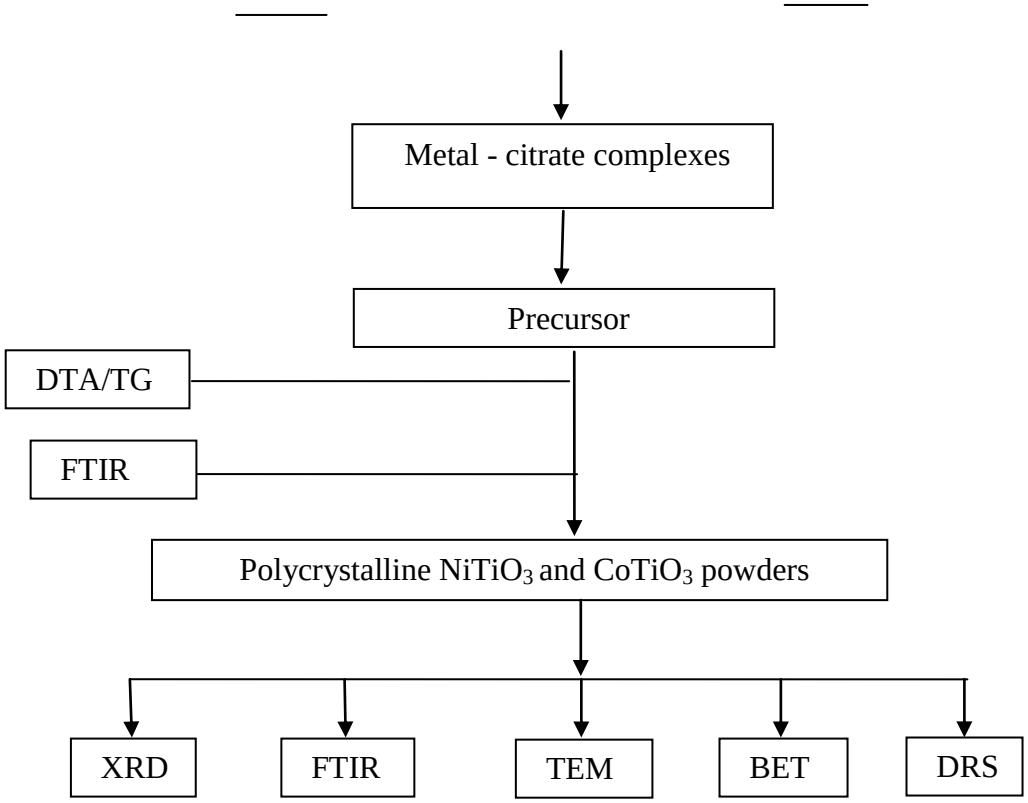

Figure 1. 10: Schematic flowchart of the synthesis of ilmenite powders by the modified Pechini method.[9]

Fine $NiTiO_3$ and $CoTiO_3$ powders of pure phase were prepared as summarized in Figure 1.10 above. The precursor metals were dissolved in ethanol at room temperature. Citric acid was slowly added to the solution, stirring to form a metal-chelate.[1] The high purity titanium (*IV*) n-butoxide was added to the solution and well stirred to ensure a homogeneous distribution of ions. The resulting solution was heated with stirring at 80°C for 1-2 h.[9] The temperature was slowly increased to 140°C to facilitate esterification and polymerization. This was then heated at 300 – 350°C for 2 h to promote pyrolysis, which yields a black powder precursor called powder precursor. The final precursor powder was subjected to calcinations in open air for 2 hr. at temperature between 550 and 1050°C to obtain $NiTiO_3$ and $CoTiO_3$ powders. [9]

1.5 Aims and Objectives

The main aim of this project is to synthesise non-stoichiometric copper-titanium oxides or titanium-copper oxides using a hypothermal synthetic method called

the Resin-gel method, also to determine the structures of the nanosized phases of the mixed-metal oxides formed and their stabilities with respect to different morphological conditions. The nanosized phases of the mixed-metal oxides should be characterised extensively using PXRD, SEM and LRTEM to determine their properties, including purity of the phases. The research project also seeks to

- Synthesise copper-titanium-oxide nanoparticles.
- Use the novel Resin-gel method, a modified Pechini method of synthesis.
- To ascertain the optimum stable form between rutile and anatase cell structures as host matrices to copper.

1.6 Project Justification

The overriding technical issue in the synthesis of metal-metal oxides is to optimise synthetic conditions to target ceramic properties, which greatly affect the characteristics of the powders. The synthetic techniques directly influence the nanoparticles' characteristics such as particle size, morphology, purity, and chemical composition. Resin-gel synthesis' key element is the use of low temperature of crystallisation but allowing a molecular mixing of constituents with controlled chemical homogeneity, purity, morphology, and phase composition of the powders.

1.7 The Scope of the Research

This research investigates the synthesis and characterisation of titanium cuprate or copper titanate using the Resin-gel method of synthesis, an extension and generalization of the modified Pechini *in-situ* polymerizable method. The intention was to look for the formation of non-stoichiometric phases of mixed-metal oxides. The basic hypothesis is that a mixture of long chain polymer (polyethylene glycol) forms a stable solution of the precursor metal ions. The working theory is that the metal ions coordinate with the polymer, which prevents any co-precipitation. Evaporation of the solvent from the system leaves behind a hard wax that combusts until it reaches a spontaneous combustion temperature and the polymer incinerate. This produces generally mixed metal oxide nanoparticles. This also enables accessing of non-stoichiometric phases.

Chapter 2: Experimental

2.1 Synthesis of Titanium-Copper-Oxides (TCO)

Copper acetate (CuAc) is a shiny deep blue fine powder. It readily dissolves in an organic solvent. CuAc was weighed on an electronic balance in increasing amounts as shown in table 2.1 below and each added to 30.00 ml of ethanol in beakers to form clear blue solutions. 30.00 ml of polyethylene glycol solid, measured equal to the total volume of the mixed solutions of the metal ions ratios was added to each beaker. Titanium chloride was introduced to supplement the percentage composition ratio of copper. It was measured using a pipette fitted with pro pipette.

The mixture was gently heated on a hot plate, while stirring to dissolve the polymer and create a clear homogenous gel. The gels were left under a 200 W incandescent lamp to evaporate the water to form a resin. The resin with the copper and titanium ions was transferred into ceramic crucibles just above half full and heated to ignition. A sand bath was used in which 8 crucibles were loaded at a time. The bath was then heated using a ring burner with the temperature of the sand bath monitored using a thermocouple. Around 100°C, the burner was temporarily turned off to allow the bath, sand and crucibles to reach a thermal equilibrium. This gradual heating was done until all of the gel liquefied.

Once the gel was liquid, the flame was increased to maximum and the system was rapidly heated to 350°C at which point ignition was initiated using a Bunsen burner. The burner ring was turned off and the temperature monitored. The crucible contents were left to burn until the flames all died out, leaving a grey to black residue.

Figure 2.1 is a flowchart of the steps in the synthesis of copper-titanium mixed metal oxide precursor nanopowders. It therefore outlines the resin-gel method of synthesising fine powders of pure phases of mixed metal oxides.

The fine precursor powders of pure phase were synthesized by the resin-gel polymerisable method as summarised in the figure below.

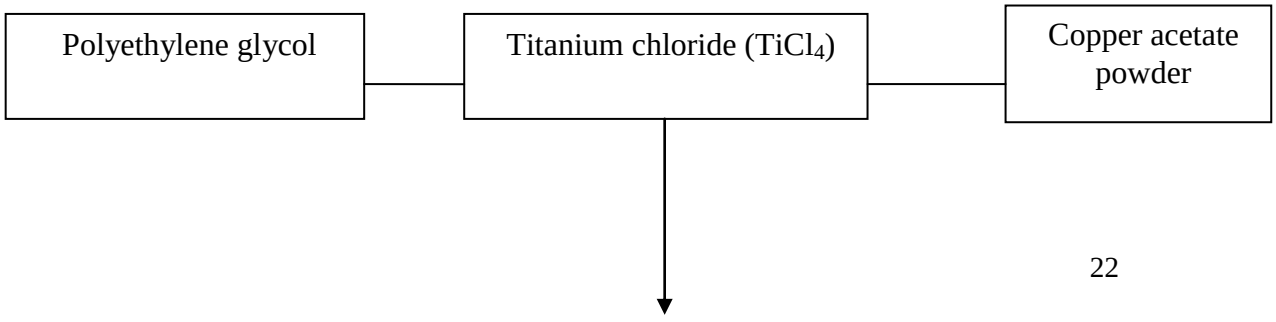

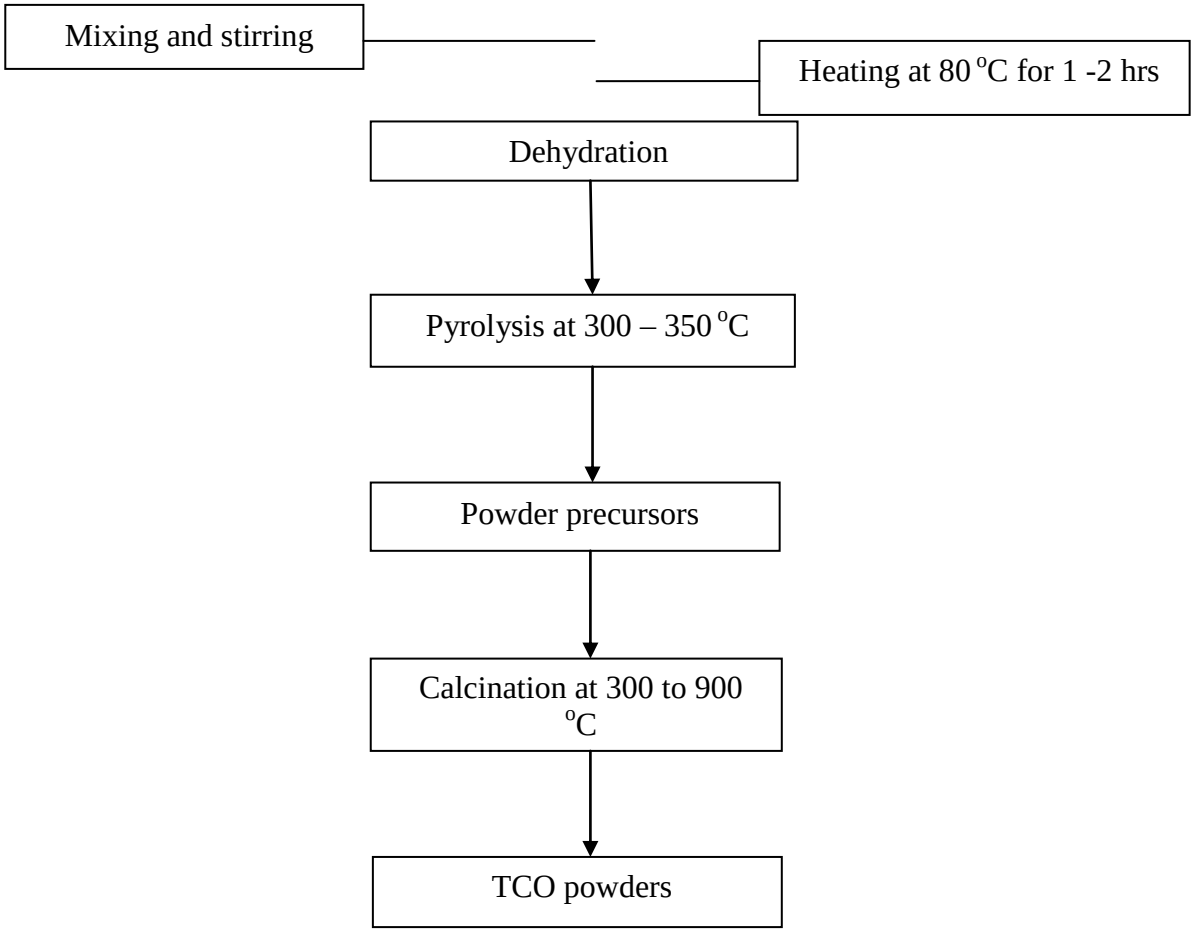

Figure 2. 1: Flowchart of the preparation of TCO powder by a resin – gel – type hypothermal polymerizable complex method [2].

Table 2.1 below is a table of values used to prepare a series of 22 samples of the titanium-copper oxide nanoparticles at the respective percentage ratios. This series of samples was used to determine the ideal copper to titanium ratio that will allow the formation of stable ceramic nanopowders. The samples were prepared carefully using the above outlined procedure, put in PVC sample bottles, and stored in a dark cupboard.

Vol. $TiCl_4$ (ml)	% Ti ratio	% Cu ratio	CuA (g)
2	100	0	0
1.9	95	5	0.18164
1.8	90	10	0.36328
1.7	85	15	0.54492
1.6	80	20	0.72656
1.5	75	25	0.9028
1.4	70	30	1.08984

1.3	65	35	1.27148
1.2	60	40	1.45312
1.1	55	45	1.63476
1	50	50	1.8164
0.9	45	55	1.99804
0.8	40	60	2.17968
0.7	35	65	2.36132
0.6	30	70	2.54296
0.5	25	75	2.7246
0.4	20	80	2.90624
0.3	15	85	3.08788
0.2	10	90	3.26952
0.1	5	95	3.45116
0	0	100	3.6328

Table 2. 1: Values calculated for percentage ratios of Ti to Cu.

2.2 Sample treatment and Analyses

The samples were put through a number of heat treatments and instrumental characterisation. Characterisation was done using PXRD and TEM. Below is an outline of the treatment and characterisation of the nanopowders.

1. PXRD analysed the samples to determine the crystalline structure of the nanocrystals by measuring the diffraction peaks of the different crystalline phases of the nanoparticles.

2. A ⅓ of each sample was separated and calcined at 300°C in a muffle furnace for an hour with the samples arranged systematically to handle systematic errors.

3. The calcined samples were analysed by PXRD again.

4. TEM analysis was done on selected samples to observe the distribution of shape, size and the homogeneity of the nanoparticles.

5. A ⅓ of the remainder of each of the precursor powder samples was separated again and calcined at 500°C in a muffle furnace for an hour.

6. Steps 2 - 4 were repeated at 700 and 900°C with a second batch.

7. Replicate samples were prepared as outlined in Section 2.2 above. The samples were also treated and analysed as in steps 1 to 6 above.

The samples of the nanoparticles were analysed and characterised for the following parameters us the Scherer's equation in Appendix A.

- particle size,
- crystallographic phases,
- stress and strain

The nanopowders produced from the resin-gel method of synthesis will be characterized using the Powder x-ray diffraction (PXRD) and the Transmission Electron Microscopy (TEM) techniques. The PXRD is mainly used to determine parameters such as crystallite size, phase purity and structural determination of nanoparticles using the Scherer's equation in section 3.4 above. PXRD analysis data is also used to explain the radial distribution of the nanoparticles and determine secondary particle characteristics such as defects in the lattice, thermal motion of the atoms in the crystal lattice and to ascertain the ratio of crystallographic phases in a multi-component sample of nanopowders using the Spurr and Myers equation in Appendix A.[35]

Figure 2.2 shows the D5000 X-ray diffractometer used in the analysis of the precursor powders. The figure illustrates the propagation of the X-rays through the sample and how diffracted rays are received and measured by the detector.[45] The data is measured against a 2θ scale and used to plot a pattern of peaks with respect to the intensity of the X-rays diffracted by the sample that identifies the phases of the crystalline particles. Phase identification was accomplished by comparing the data (peaks and relative intensities) from the specimen with peaks and relative intensities from a very large set of "standard" data provided by the International Centre for Diffraction Data (ICDD). The current PDF4 release in use (2006) contains 254,873 Digital PXRD patterns, both experimental and calculated, from almost every known inorganic crystalline material. The research

laboratory in the School of Chemistry Wits university use Eva (from Materials Data) to facilitates the access to this massive and continually growing database.

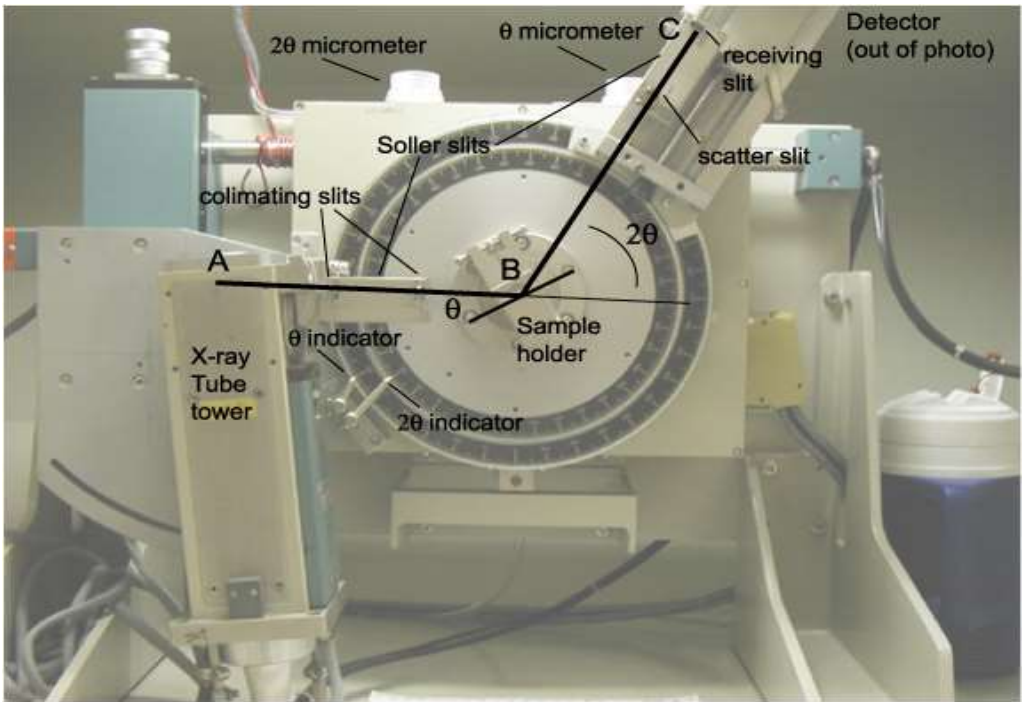

Figure 2. 2: D5000 x-ray diffractometer used in the analysis of the mixed metal oxide nanopowders.

Eva includes an automated search-match function that compares the sample pattern with the ICDD database. With good data from a single-phase sample, Eva's automated search-match program will usually identify the phase successfully with little or no human effort. For most two-phase samples, identification of the dominant phase was successful, but the second required more hunting. With three or more phases (and virtually all bulk rocks), some knowledge of the likely constituents was required to determine the constituents. Fortunately the ability to visually compare the sample patterns to a large number of possible phases was a manageable task. In this research work, the samples were analysed between 10^0 and 90^0 in a 22 minute no spin cycle repeated 5 times.

The TEM was used to measure the particle diameter of the nanoparticles. The basic principle of application involves passing a beam of electrons through a specimen and collecting an image of the particles as they are dispersed under the microscope. From this image, the shape and size of the nanoparticles was also determined.

Chapter 3: Results and Discussion

3.1 PXRD Analysis

3.1.1 Trends in peak patterns

Several researchers use PXRD to characterize reaction products from various methods of preparation of mixed metal oxides.[7] Figures 3.1 to 3.5 below presents PXRD patterns of the precursor powders calcined at different temperatures for an hour in a muffle furnace. Precursor powders formed from different Ti/Cu ratios but the same PEG/AA v/v ratio. Ti percentage composition increased by 5% with the first sample having 0% Ti and the last one with 100% simultaneously with Cu composition decreased by 5% starting from 100% down to 0%.

PXRD analysis found extensive use in the characterization of titanium oxides γ – TiO, δ – TiO, and Ti_2O and titanium –copper oxides.[4, 5, 9] In this research PXRD found use in the analysis of the products of Resin gel synthesis of mixed metal oxides. The PXRD patterns stacked in Figure 3.1 are for the non-calcined precursor powders. The phases of the various mixed metals formed concurrently. The bottom-most pattern is for a sample composed of 0% Ti and 100 % Cu and the top-most pattern is composed of 100% Ti and 0% Cu. In this series, the first peak appearing is at 2θ 16.5^o that is due to CuO crystalline phase. This peak is non-existent at 0 to 20% Ti percentage composition in the series. At 25% Ti, the peak appeared as a small finger at a low intensity and quite narrow at its base. This steadily increased in intensity with an increase in Ti percentage composition. Detailed analysis revealed that this peak reached its maximum peak intensity at 60% Ti: 40% Cu where it had a substantial peak height and a broad base. At 65% Ti, this peak started decreasing in intensity until it was indistinguishable in the last three compositions of the series. This confirms its likely source as that of an unknown non-stoichiometric $Cu_xTi_yO_z$ material. This implies that the unknown $Cu_xTi_yO_z$ phase formed optimally within a range of 25 to 60% Ti and 40 to 75% Cu composition. Outside this range, the pure phases of TiO_2 and Cu oxides preferentially form. It was observed that most of the peaks

were TiO_2 or CuO phases in which more peaks of other phases overlapped together.[11] For example, the peak of mixed $Cu_xTi_yO_z$ was found to be overlapping with both the Anatase (TiO_2) and the Tenorite (CuO) peaks. PXRD only does not reliably suffice to identify the reaction products of the synthesis of mixed metal oxides. Rietveld refinement is applicable with PXRD results in accurately measuring the d – space change in the TiO_2 and CuO phases.[12] Both PXRD and TEM directly characterize and give detailed analysis of the phases.[14]

The second peak in the stacked patterns at 2θ 25.5^o is totally absent in the first sample but appeared as a small peak in the sample at 5% Ti: 95% Cu composition. This implies that the peak is due to the introduction of Ti and detailed analysis identified the peak as due to the anatase TiO_2 polymorphic phase. The peak and all others associated with anatase are initially at low peak height or intensity. They then steadily increased in intensity at every 5% Ti composition increase across the series. The peak base broadened with the increase in Ti percentage composition. This phenomenon persisted across the series such that at 100% Ti composition, a high intensity and broad based peak with no peak shift of the TiO_2 anatase phase appeared identifying a pure phase of the polymorph.

At 0% Ti: 100% Cu, a pair of broad joined peaks occurs at 2θ 35.5^o and 39^o. The joined bases span from 2θ 34^o to 40^o and are matching multiphased composition of mixed metal oxides Cu_xTi_yO and CuO polymorphs.[14] The multiphased oxides identifiable on these peaks include CuO, Cu_4O_3, Cu_2O and metal-metal oxides of copper titanium oxide (Cu_xTi_yO). These phases persisted such that in the first three samples they contributed to the observed increase in peak intensities. At 15% Ti: 85% Cu, the peak intensities showed a gradual decrease at every 5% decrease in Cu percentage composition. It is noticeable that the phases Cu_2O and some forms of Cu_xTi_yO phases disappeared at this composition as shown in Appendices B to F. This implies that the abundance of Cu in the precursor mixture, more of the stable phases of copper oxides formed.[16] The phases, CuO, Cu_4O_3, and two phases of Cu_xTi_yO persisted in the multiphased mixture of the copper-based metal oxides. This pair of copper-based oxide peaks continued decreasing in height or intensity with respect to the peak due to anatase such that

at 45% Ti: 55% Cu, the peak intensities were almost equal. At 50:50 compositions, the anatase (TiO_2) peak surpassed the tenorite (CuO) peaks in intensity. The tenorite peaks gradually continued to decrease in intensity and broaden such that at 90% Ti: 10% Cu, the pair of tenorite peaks merged to give a single short but broad based peak before it completely disappeared at 95% Ti: 5% Cu.

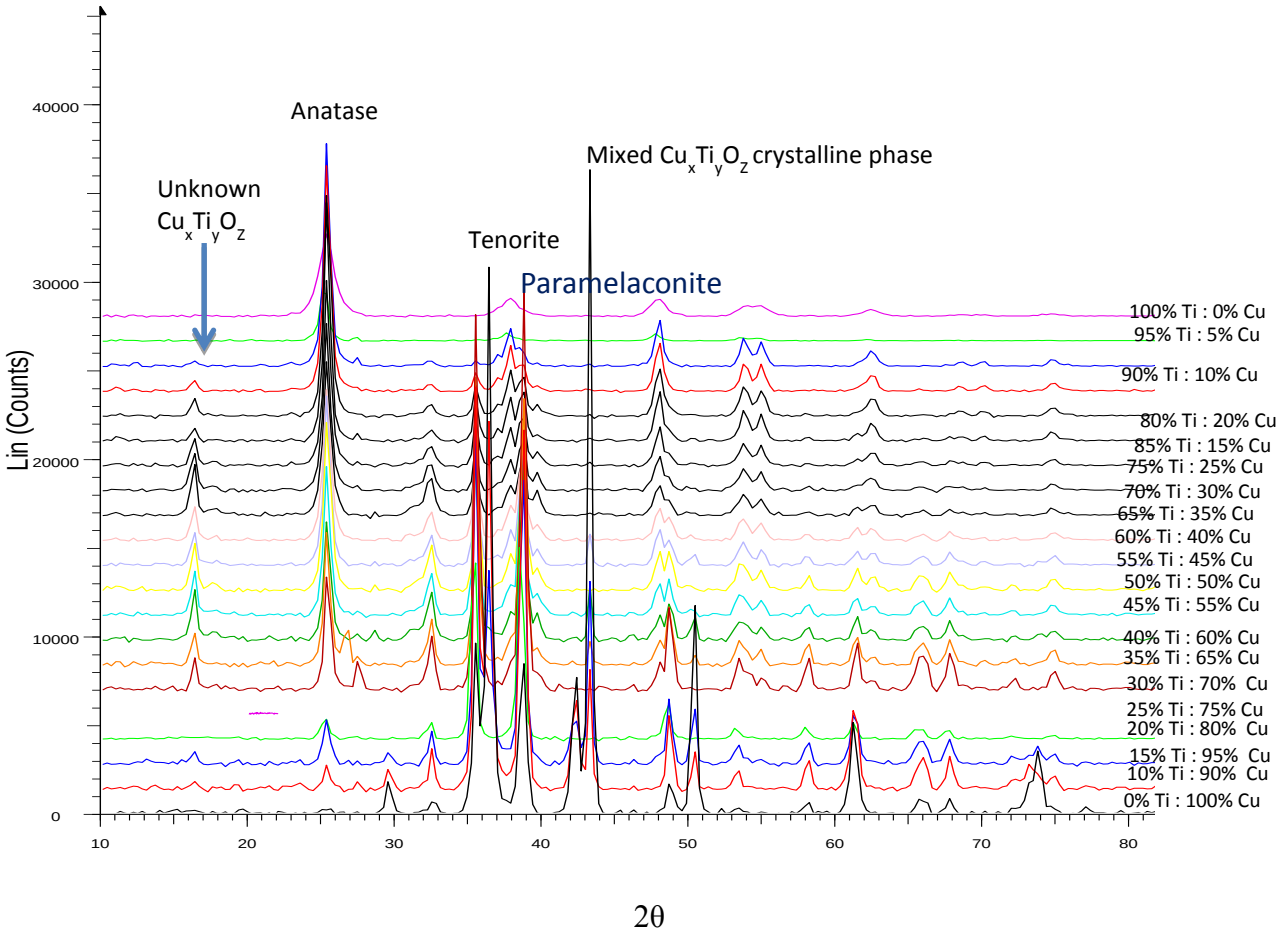

Figure 3.1: PXRD pattern of non-calcined resin-gel precursor powders of mixed Ti and Cu oxides

As seen in Figure 3.1 above the first peak in the stacked PXRD patterns of the 300°C calcined series occurs at 2θ 16.5°. It is noticeable that the phase occurring at 2θ 16.5° diminished whenever a rutile TiO_2 peak appeared. This can be an indication that the phase is decomposing to give rutile phase TiO_2 and CuO. However, this peak does not exist in patterns at compositions 0% Ti: 100% Cu and 5% Ti: 95% Cu respectively. At 10% Ti: 90% Cu, the peak appeared as a broad peak that is not well developed and had a small peak height. This phenomenon persisted in the series until in sample at 35% Ti: 65% Cu

composition where the peak narrowed in base and increased in peak height. At 45% Ti: 55% Cu the peak height started to decrease gradually until at 90% Ti: 10% Cu composition where the peak completely disappeared.

The peak at 2θ 25.5^{o} is insignificant in the first two samples at compositions 0% Ti: 100% Cu and 5% Ti: 95% Cu respectively. However, at 10% Ti: 90% Cu a small peak that is indistinct appeared and matched an anatase peak. This peak gradually increased in intensity and base narrowing at every 5% increase in Ti composition. A tiny peak also appeared at the foot of the anatase peak and identified with a peak due to rutile phase. This phenomenon persisted until in the sample at 45% Ti: 55% Cu composition and the rutile phase disappeared. The peak intensity of the anatase increased at every 5% increase in Ti, such that at 90% Ti: 10% Cu the anatase peak was highly dominant. At 100% Ti, the peaks in the pattern are all due to a pure phase of anatase polymorphic phase.

In the first sample, the composition is 0% Ti: 100% Cu, the peaks produced are due to copper oxides. The main polymorph in the mixed copper oxides is the tenorite occurring in a multiphased mixture comprising paramelaconite, cuprite and copper titanium oxides. This also occurred in the second sample at 5% Ti: 95% Cu. The multiple phases were identifiable at two conjoined peaks occurring at 2θ 35.5^{o} and 39^{o}. The peaks are of high intensity and peak height. As the percentage of copper composition decreased across the series, the peak intensities of these peaks also decreased. The peak at 2θ 40^{o} identified a multiphased mixture of metal oxides. The peak initially had a high intensity but decreased up the series. The possible mechanisms of formation for some phases of $Cu_xTi_yO_z$ are described by the following equations:

$$8CuO + 4TiO_2 \rightarrow 2Cu_4Ti + 2TiO + 7O_2 \quad (1)$$

$$3Cu_4Ti + 2TiO \rightarrow Cu_3Ti_3O + Ti_2O + 9Cu \quad (2)^{26}$$

TiO could form from the reduction of paramelaconite by Ti as in Eq. (1), Cu_4Ti could form by the reaction of Ti, and Cu during bonding process as illustrated in Eq. 2. It is possible that Cu_4Ti reacted with TiO to form Cu_3Ti_3O and Ti_2O phase during cooling according to Eq. (3). However, in my research and Suenaga et

al.[25] the Ti_2O phase did not matched any of the PXRD patterns obtained and presented in Figures 3.1 to 3.7. This also confirms that the phase is highly unstable with respect to its rutile and anatase polymorphs.[26]

At 50:50 percentage compositions, the anatase and tenorite peaks are almost of the same intensity as presented in Figure 3.1. At this composition, there is a breaking point whereby the anatase peak surpasses that of tenorite peaks. This occurs as the Ti percentage continues increasing while that of Cu decreases. From the sample at 55% Ti: 45% Cu, the tenorite peaks decreased in height with every 5% decrease in Cu composition. At 90% Ti: 10% Cu, the tenorite peaks merged to form a single broad peak that was not identifiable with any of the copper oxide polymorphs. At 95% Ti: 5% Cu and 100% Ti: 0% Cu, all the peaks were due to pure phase of the anatase polymorph. There is a small peak found at 2θ 33^o in the stacked PXRD patterns in Figure 3.2 below. The peak is initially identifiable with the tenorite phase. However, further detailed phase matching determined another phase occurring at the same peak. The phase is a titanium complex that has a similar diffraction pattern to the pseudobrookite phase of iron titanium oxide. This peak persisted throughout the series until at composition 95% Ti: 5% Cu.

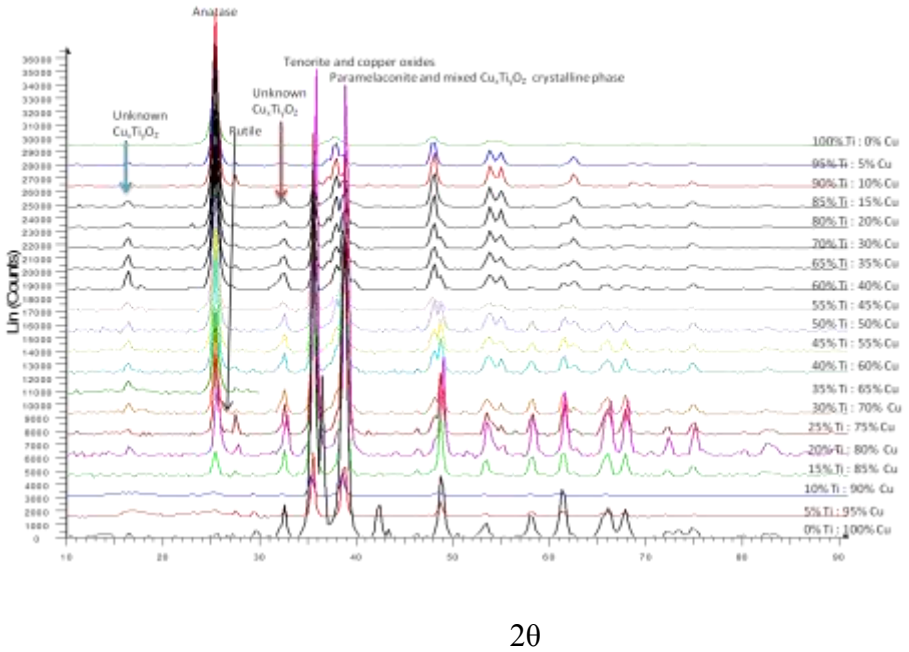

Figure 3.2: PXRD patterns of resin-gel precursor powders of mixed Ti and Cu oxides calcined at 300°C.

The first sample in the series at 500°C shows peak patterns of a pure phase of tenorite as presented in Figure 3.3 on 2θ 35.5^{o} and 39^{o}. The peaks are of very high intensity and have a broad base as presented in Figure 3.3 below. In the second sample, 5% Ti was introduced and a small peak appeared at 2θ 25.5^{o} and was identified as due to anatase phase of the titanium oxide polymorph. The peaks at 2θ 35.5^{o} and 39^{o} in this sample decreased in peak broadness but remained at high intensity. There are additional copper-based phases identifiable at these peaks. In addition to tenorite, there are paramelaconite and copper titanium oxide polymorphs.

As the percentage of Ti composition increased and Cu decreased, the peaks at 2θ 35.5^{o} and 39^{o} gradually decreased across the series while that of anatase increased as presented in Figure 3.3 below. The anatase peak continued to increase in intensity so that at 95% Ti: 5% Cu composition, the peaks in the PXRD pattern were of a pure phase of anatase with a small peak of rutile occurring at the foot of the major anatase peak. Figure 3.3 below indicates that at 100% Ti, a pure phase of anatase with a very high intensity and broad based peak occurred. As the peak intensity decreased at 2θ 35.5^{o} and 39^{o}, the peak bases progressively broadened so that at 90% Ti: 10% Cu, the paramelaconite and the $Cu_xTi_yO_z$ phases were nonexistent in the sample and only tenorite occurred and had a small peak which was indistinct as presented in Figure3.3 below.

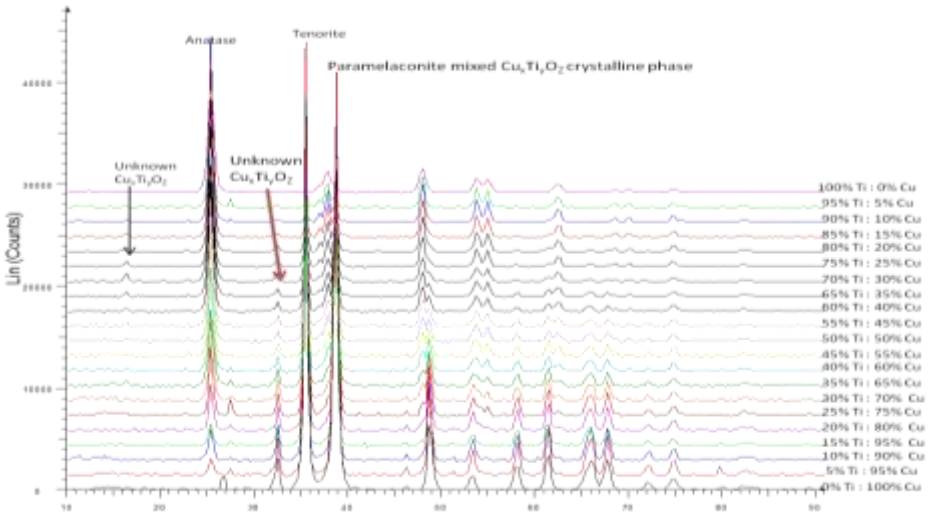

Figure 3. 3: PXRD patterns of resin-gel precursor powders of mixed Ti and Cu oxides calcined at 500°C

At 95% and 100% Ti compositions, pure phases of anatase occurred with no tenorite or other copper-based phases occurring. It is noticeable that a peak identified at 2θ 33^{o} described in the 300°C series is not portraying the same phenomenon represented previously. This is because in this series, it is not changing significantly in the peak properties and characteristics to show multiphase matching at this peak.

The peak at 2θ 16.5^{o} of the unknown $Cu_xTi_yO_z$ observed in Figures 3.1 to 3.3 is completely absent in the stacked patterns of samples calcined at 700°C in Figure 3.4. This implies that the phase is highly unstable at high temperatures above 700°C. However, just like in the previous calcination temperature, Figure 3.4 presents the first sample has a PXRD pattern identifying a pure phase of tenorite. The major peak is found at 2θ 35.5^{o} and 39^{o}. The peaks are of high intensity and broad base. This sample is composed of 100% copper only. The second sample is composed of 5% Ti: 95% Cu. This composition introduces Ti that gives rise to a peak at 2θ 26^{o} identifiable with anatase and a small peak at 28^{o}, which is due to rutile phase of the titanium dioxide polymorphs as presented in Figure 3.4. The anatase peak increased in intensity at every 5% increase in Ti percentage composition. At 60% Ti: 40% Cu, the anatase peak increased in height to have a peak with the greatest peak intensity as presented in Figure 3.4. It continued to increase in intensity with the increase in Ti percentage composition so that at 100% Ti, intense peaks identifying a pure phase of the anatase occurred. The peaks occurring at 2θ values 35.5^{o} and 39^{o} in Figure 3.4 identified multiphased polymorphs of tenorite, paramelaconite and copper titanium oxides. As the percentage of Cu continued decreasing, the peak intensities also decreased with every 5% Cu decrease. At 85% Ti: 15% Cu, the peaks identified only tenorite and paramelaconite. At 95% Ti: 5% Cu, the peaks merged and were very small, indistinct, and identified only tenorite and none in the 100% Ti: 0% Cu. The small rutile peak at 2θ value 28^{o} at the base foot of the anatase peak persisted throughout the series. However, the peak remained a small peak with low intensity. At 60% Ti: 40% Cu, the rutile peak completely disappeared and never appeared again in the rest of the series of the samples.

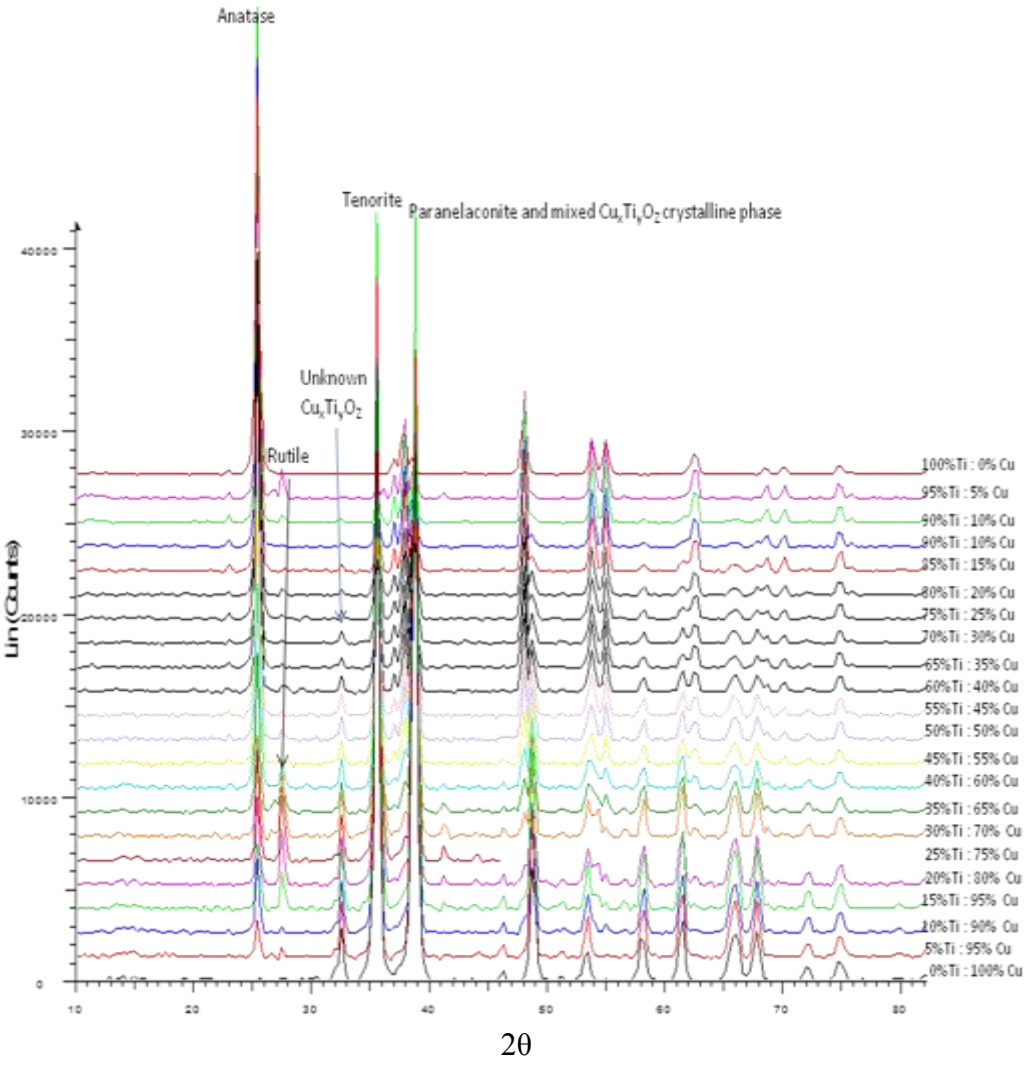

Figure 3. 4: PXRD patterns of resin-gel precursor powders of mixed Ti and Cu oxides calcined at 700°C.

The first sample in the patterns represented in Figure 3.5 produced a peak pattern of the pure phase of tenorite with major peaks occurring at 2θ 35.5^o and 39^o. It is noticeable that unlike in previous calcination temperature series, the peak pattern has only one phase of the CuO polymorphs. This is because of the high temperatures that result in all other phases, transforming to a more stable phase of the tenorite. In the second sample, a small peak occurred at 2θ 28^o. This peak is due to the introduction of 5% Ti giving rise to a pure phase of rutile of the titanium dioxide polymorph. This peak increased in intensity with every 5% increase in Ti percentage composition across the series as presented in Figure 3.5. At 50:50 percentage compositions, the rutile phase's peak reached almost equilibrium in intensity with the tenorite peak. It then surpassed the tenorite peak

and continued to increase in intensity so that at 100% Ti, a highly intense peak of the rutile polymorph presented a pure phase of rutile TiO_2. The PXRD suggest that annealing or calcining improves the crystallinity of $Cu_xTi_yO_z$ materials.[16] As observed in Figure 3.5, $Cu_xTi_yO_z$ nanoparticles calcined at 700 °C and above exhibit distinct metal oxide peaks as compared to those calcined at 500 °C. Figure 3.5 below presents the X-ray pattern of $Cu_xTi_yO_z$ oxides powders after the third treatment at 900◦C. It illustrates that a single phase of $Cu_xTi_yO_z$ is formed whose diffraction peaks are quite sharp indicating that the samples are well crystallized.[17] The tenorite CuO peaks gradually decreased in intensity with every 5% decrease in Cu composition as presented in Figure 3.5. This phenomenon persisted across the series such that at 50:50 percentage compositions, there was a shift in peak dominance so that the rutile TiO_2 peak became more intense than the tenorite CuO peak. The tenorite CuO peak continued decreasing in intensity so that at 95% Ti: 5% Cu, it diminished to insignificant levels and at 100% Ti, only pure phases of anatase and rutile TiO_2 occurred.

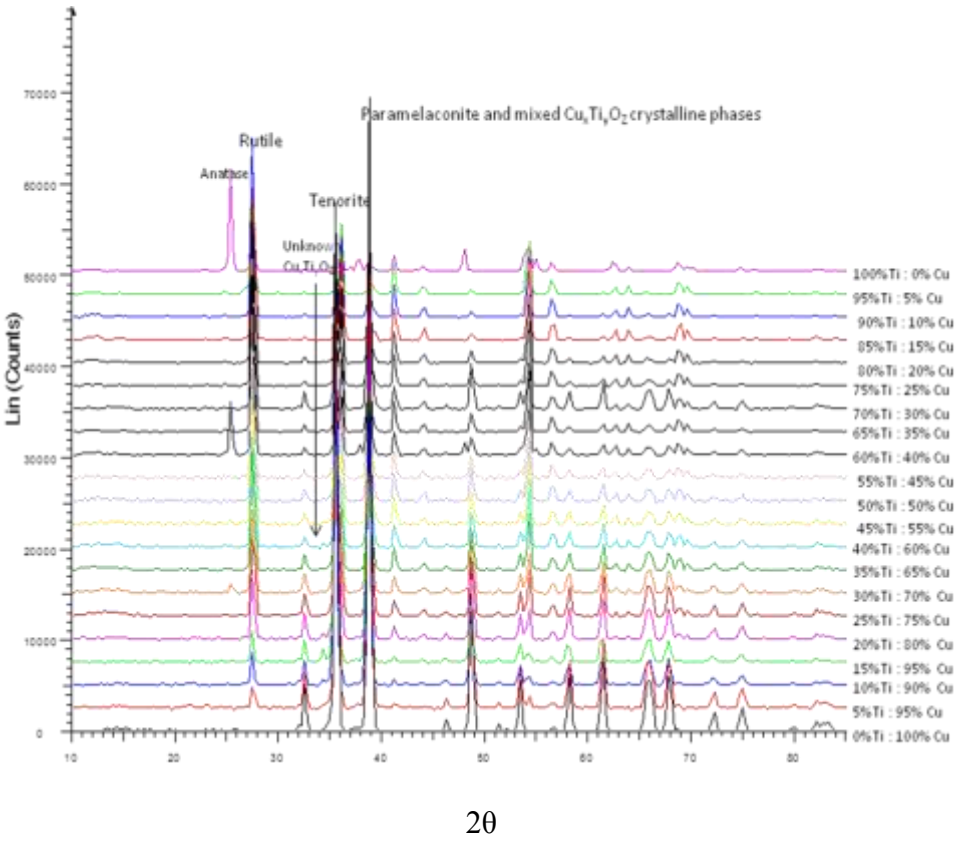

Figure 3. 5: PXRD patterns of resin-gel precursor powders of mixed Ti and Cu oxides calcined at 900°C.

It is noticeable that the tenorite CuO peaks in Figure 3.5 identified multiple phases of paramelaconite Cu_4O_3 and other copper titanium oxides on the same peaks. The peaks are narrow at their base and separated unlike in previous series. As the peaks decrease in intensity, the peaks never merged to form one broad peak as in previous series.

3.1.2 Effect of percentage composition on peak patterns

As the percentage of Ti composition increased, two peaks appeared below 2θ 30^o, an indication that another phase of TiO_2 formed. This peak is very small but distinct. As the percentage of Ti continued to increase with the decrease of copper at 5 % intervals, the peak due to titanium dioxide also increased while the intensity of the peaks due to copper oxides decreased progressively. Between the 35% Ti and the 50% Ti patterns, the peaks of titanium oxide and copper oxides changed in their intensities so that the Ti peaks became more intense while those of copper oxides became less intense. This trend in peak intensity fluctuation continued until the peaks due to copper oxides vanished leaving a major peak pattern representing a pure phase of titanium oxides, a trend presented in Appendix A.

The nature of the peak patterns obtained in this analysis corresponds to the percentage composition of the mixed oxides. At every change in percentage composition of the mixed metal oxides, a new peak appears in either the pattern or the intensities of the existing peaks, and increases or decreases with respect to the composition of the first pattern. For the patterns in Figures 3.6 and 3.7, a peak, occurring at 16.5^o on the 2θ scale, appeared and did not identify with any other peaks due to titanium or copper oxides. It is noticeable that this peak appeared for the first time when the percentage of Ti was increased from 20^o to 25 %. At this composition, this peak is quite small and its intensity continued to increase until at titanium composition of 70 %. This peak started to decrease in intensity until it vanished at a composition of 0 % copper. This shows that the peak is due to a phase of Cu_xTi_y.

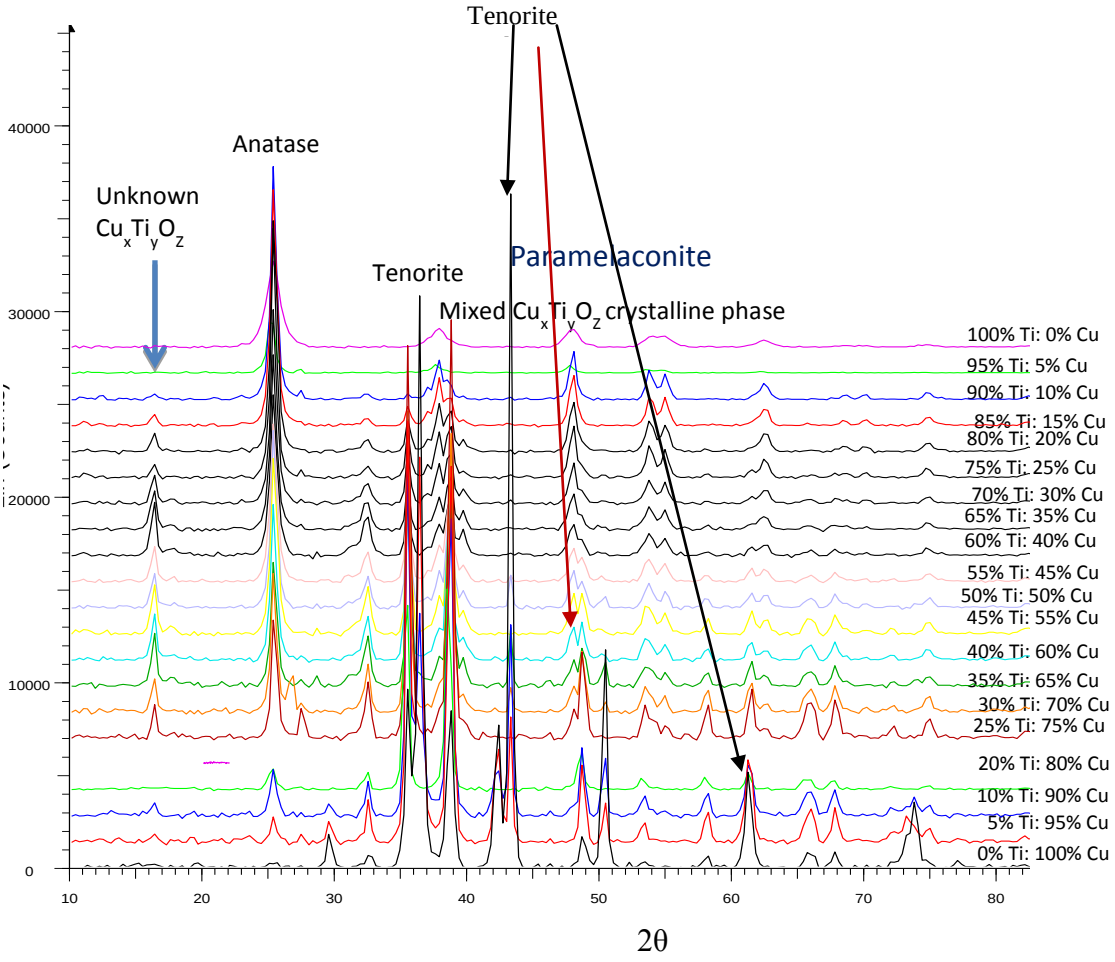

Figure 3. 6: PXRD patterns of non-calcined resin-gel precursor powders of mixed Ti and Cu oxides.

3.1.3 Effect of Temperature variation on Peak Patterns

Polymorphism arises when a given material adopts a different crystal form under different conditions of pressure and temperature.[14, 16] This section gives a detailed account of this phenomenon.[10] Precursor powders of specific percentage compositions were treated at increasing calcination temperatures and the polymorphic transformations where scrutinised from PXRD patterns of their nanopowders. Transition metal oxides show several solid-solid phase transitions as they are heated and the atoms adopt a new packing arrangement.[19, 22, 36] The samples with different metal percentage compositions were all treated at 300°C, 500°C, 700°C and 900°C calcination temperatures. The most closely packed phases are thermodynamically favoured at low temperatures and the less closely packed structures are favoured at high temperatures.[2, 10] Thus, polymorphism is a common consequence of the low directionality of metallic bonding and gives rise to crystalline form changes and Ostwald ripening.[9, 10, 12]

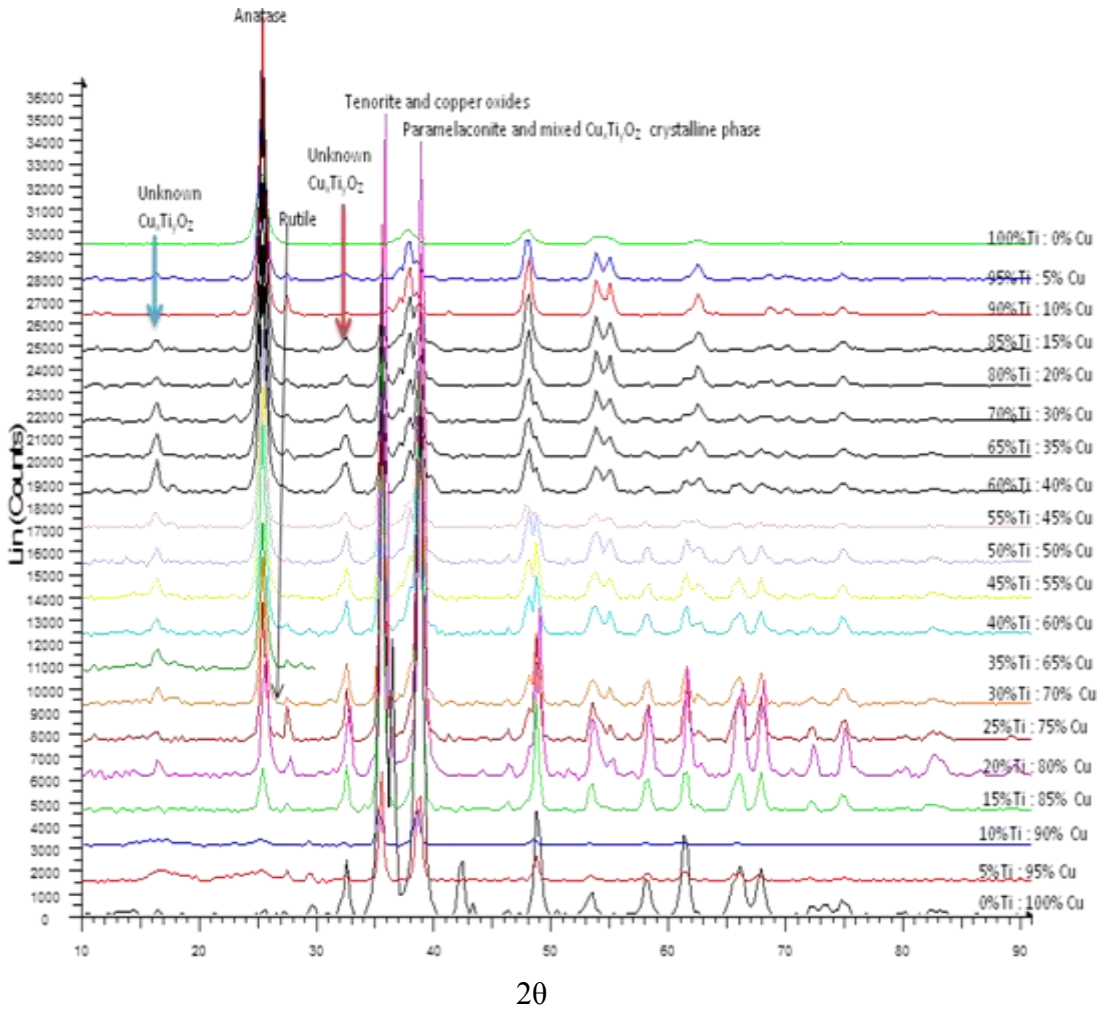

Figure 3. 7: PXRD patterns of resin-gel precursor powders of mixed Ti and Cu oxides calcined at 300°C.

The samples treatment at 500°C, have the contents of samples still as CuO, rutile-TiO_2, CaO, Cu_4Ti_3 and $Cu_xTi_yO_z$, respectively. But the relative amount of $Cu_xTi_yO_z$ increases, which can be confirmed by the increased relative intensity of X-ray peaks of $Cu_xTi_yO_z$ in Figure 3.3. After the second calcination at 500°C, the main phase was TiO_2 or CuO phase in the oxide powders.[17] Only a slight amount of other phases such as Cu_2Ti_3, Cu_4O_3 and rutile $Cu_xTi_yO_z$ can be observed, as presented in Figure 3.3 above. X-ray peak intensities revealed that the relative amount sum of these phases is minimal.[14, 16, 17] For obtaining single phase, above powders were calcined at 700 °C and 900 °C. PXRD patterns illustrates that a single phase of CuO and TiO_2 is formed whose diffraction peaks are quite sharp indicating that the samples are well crystallized.[17]

Oxides of Ti transformed from amorphous TiO_2 to anatase at temperatures below 700°C. Further heating transformed the TiO_2 to predominantly the rutile phase at temperatures above 700°C. Oxides of Cu produced two forms of polymorphs. Firstly, there are the copper *(II)* oxide phases of tenorite and amorphous CuO. Secondly, there are copper *(I)* oxide phases of paramelaconite (Cu_4O_3) and other related copper oxides. Mixed metal-metal oxide phases of copper titanium oxides (Cu_xTi_yO) also formed. The analyses below describe and explain trends in the PXRD patterns of samples of the same composition but different calcination temperatures. The precursor powders were prepared in duplicate under same the conditions. Analysis of duplicate samples in the same analyses produced same graphs represented in this section for the respective samples.

i) Trends in the 0% Ti: 100% Cu

The non-calcined precursor powders produced PXRD peak patterns that identified a mixture of unreacted copper, tenorite, cuprite and paramelaconite. Figure 3.1.1 is a PXRD pattern of replicates of non-calcined samples. The peak patterns in these figures are due to the above mentioned copper oxide polymorphs. The cuprite (Cu_2O), copper oxide (CuO) and paramelaconite (Cu_4O_3) were identifiable on the same peaks at 2θ 35.5° and 39°. It is this overlapping of the peaks of the metal oxides that decrease the accuracy in identification of the respective phases.[7] However, the two major peaks are broad based throughout the calcination

temperatures but had peak intensities lower than expected of a pure phase due to peaks overlapping. This phenomenon persisted as shown in Appendices B to F.

As calcination temperature increased, there was narrowing of peak broadness with increase in temperature so that the peaks became very narrow and distinct at 500°C, 700°C and 900°C respectively. The XRD results indeed proved that calcining improves the crystallinity of metal oxides. As observed in Figure. 3.1.1 Cu_xTi_yO calcined at 700 °C and above exhibit distinct metal oxide peaks as compared to those annealed at 500 °C.[16] Detailed phase matching determined that the major peaks are identifying the tenorite phase of the copper oxide polymorphs. The amorphous copper oxide, paramelaconite and cuprite occurred on the same peaks as the tenorite peaks in the non-calcined sample of the multiphased multicomponent mixture of the mixed metal oxides.

ii) Trends in the 5% Ti: 95% Cu

In this composition, there is the introduction of Ti in the sample. A small peak was observed occurring at 2θ 25.5° as presented in Figure 3.1.2. Detailed analysis determined the peak to be due to titanium dioxide from PXRD analysis.[10, 44] This peak was absent in the PXRD pattern of the first sample because there was 0% titanium. The non-calcined powders and the powders calcined at 300°C, 500°C and 700°C, show that the polymorphic phase of the TiO_2 is anatase. This trend is presented in Appendices B to F.

Another small peak occurred at 27.5° as presented in Figure 3.1.2. The peak was identified as due to the rutile phase of the titanium dioxide. This peak occurred initially at 700°C. At 900 °C the peak due to rutile phase is the only TiO_2 peak occurring while the anatase peak disappeared. This implies that the anatase phase changed to rutile phase at temperatures above 700 °C. The peaks with the highest intensities occurred at 2θ 35.5° and 39° and were identified with multi-phases of copper derivatives in the mixture of metal oxides.

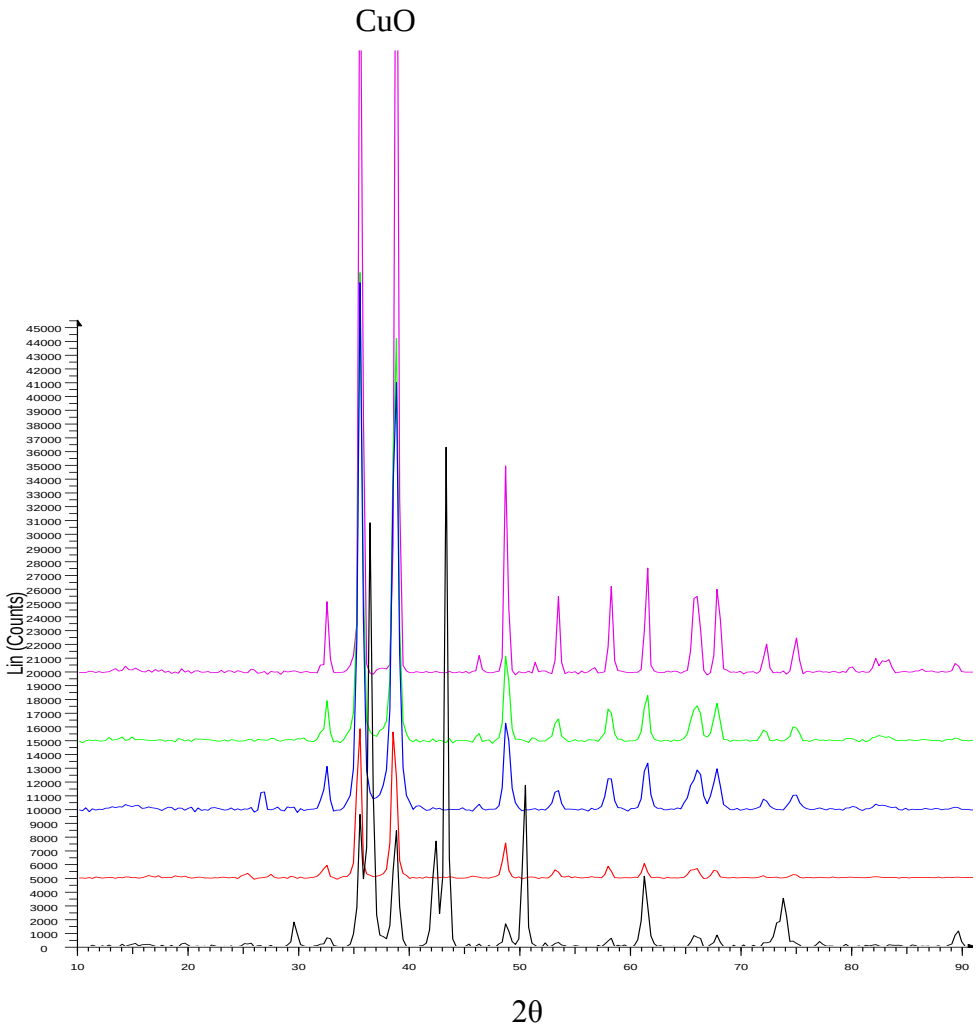

Figure 3.1. 1: X-ray diffraction patterns of the precursor powders of percentage composition 0% Ti and 100% Cu.

The oxides, tenorite, paramelaconite, cuprite and copper titanium oxides were all matched on the same peaks. This implies that these oxides contributed in the broad peak ranging from 2θ 41° to 44° on the 2θ scale as presented in Figure 3.1.2 below. The peak base is wide in the non-calcined peak pattern. The peak is notably conjoined and of great peak height. This phenomenon also occurred in the sample calcined at 300°C. The peaks also identified a pure phase of Ti_3Cu_3O. However from 500°C to 900°C calcined samples, the peak disappears as shown in Figure 3.1.2. This implies that the phase is unstable at higher temperatures and was transformed into more stable polymorphic forms of copper titanium oxides.

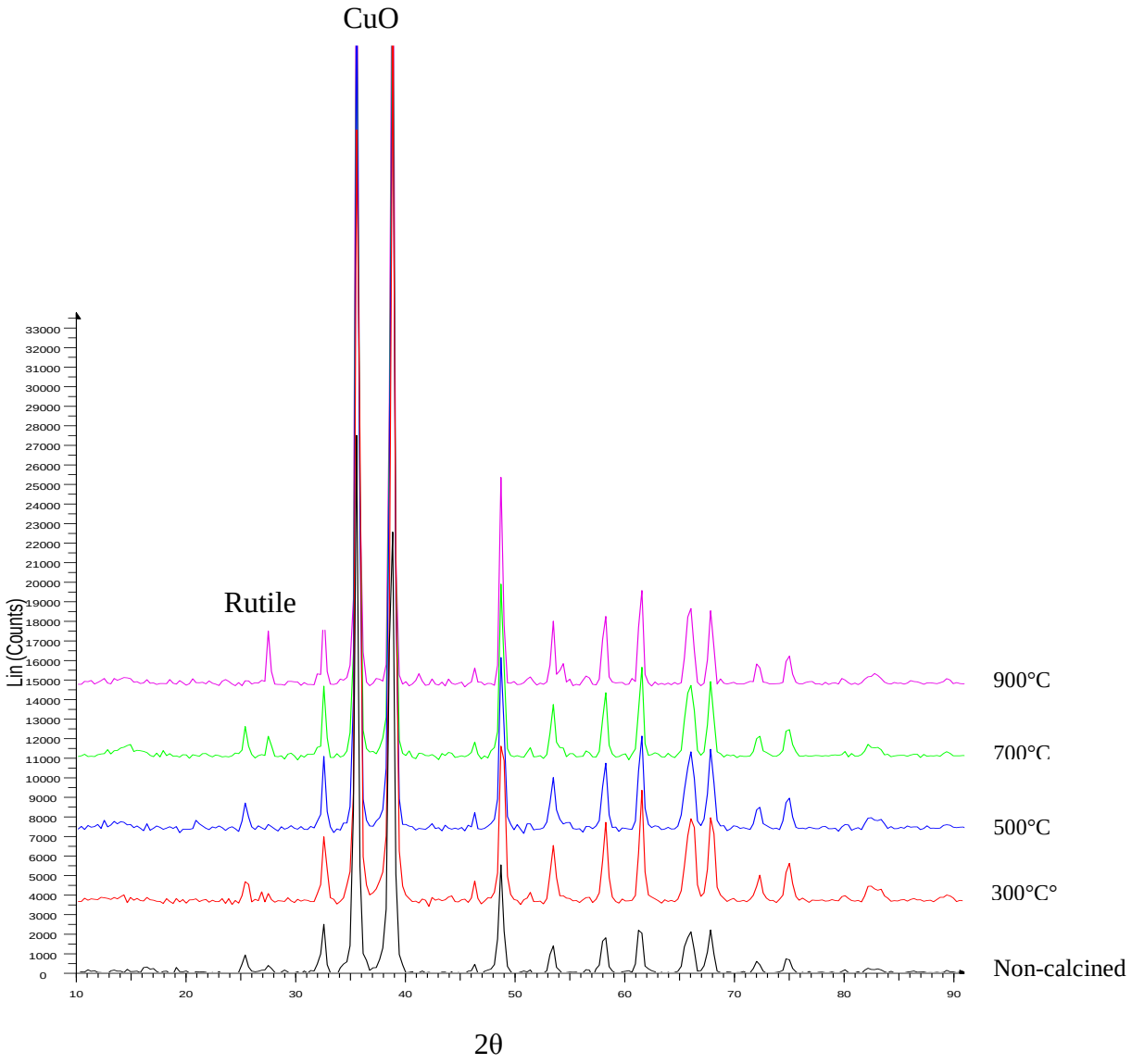

Figure 3.1. 2: X-ray diffraction patterns of the precursor powders of percentage composition 5% Ti and 95% Cu.

iii) Trends in the 10% Ti: 90% Cu

The non-calcined sample has a peak pattern with a small peak occurring at 2θ 15.5°. The peak broadened in base and increased in peak height as the sample was calcined at 300°C. At higher calcination temperatures, this peak vanished completely, as presented in Figure 3.1.3.

The peaks with the greatest peak intensity and height occurred at 2θ 35.5° and 39°, as presented in Figure 3.1. The peaks were determined to be due to the multiphased of copper oxides tenorite, paramelaconite, cuprite and copper titanium oxides. The peaks are broad and conjoined at the base as shown in the

figures below in the non-calcined sample peak patterns. As the calcination temperatures increased, the tenorite peak broadness reduced, so that at 900°C the peaks have a great intensity and narrower base as presented in Figure 3.1.3. At 900°C these peaks identified a pure phase of tenorite.

The peak identified at 25.5° on the 2θ scale in the non-calcined sample is due to a titanium dioxide phase of anatase. This phase persisted through higher calcination temperatures up to 700°C. At 900°C, this phase completely transformed to rutile and gave rise to a peak at 28° on the 2θ scale as presented in Figure 3.1.3.

Figure 3.1.3 shows a peak with a broad base ranging from 41° to 44° on the 2θ scale occurring in the non-calcined sample with two peaks, one due to titanium copper oxide (Ti_3Cu_3O) and the unreacted copper. On calcination, this peak completely disappeared, meaning that the phases identified on these peaks were transformed to other more stable forms of the copper oxide polymorphs.

iv) Trends in the 15% Ti: 85% Cu

The non-calcined sample in this composition showed a peak at 2θ 25° as presented in Figure 3.1.4 below. The peak was identified as due to the anatase phase of the TiO_2 polymorph. This peak is of low intensity due to low Ti composition in the reaction mixture. The peak persisted at higher calcination temperatures up to 700°C. At 900°C, this peak disappeared completely. However, a small peak occurred at the foot of the anatase peak at 28 on 2θ scale. For the non-calcined sample, the peak is just a tiny finger that persisted even at higher temperatures. At 700°C, the peak became of significant intensity that it was identified as due to another phase of TiO_2 polymorph called rutile as explained further in section 3.2. At 900°C, this peak intensified and was due to a pure phase of the rutile polymorph. This implies that the anatase phase was transformed to rutile at temperatures above 700°C. The peak at 2θ 33° in Figure 3.1.4 below is due to the copper oxide polymorphic phase tenorite that has intense peaks at 35.5° and 39° on the 2θ scale. At these peaks, multiphase

matching occurred with the identification of phases, copper titanium oxides and paramelaconite.

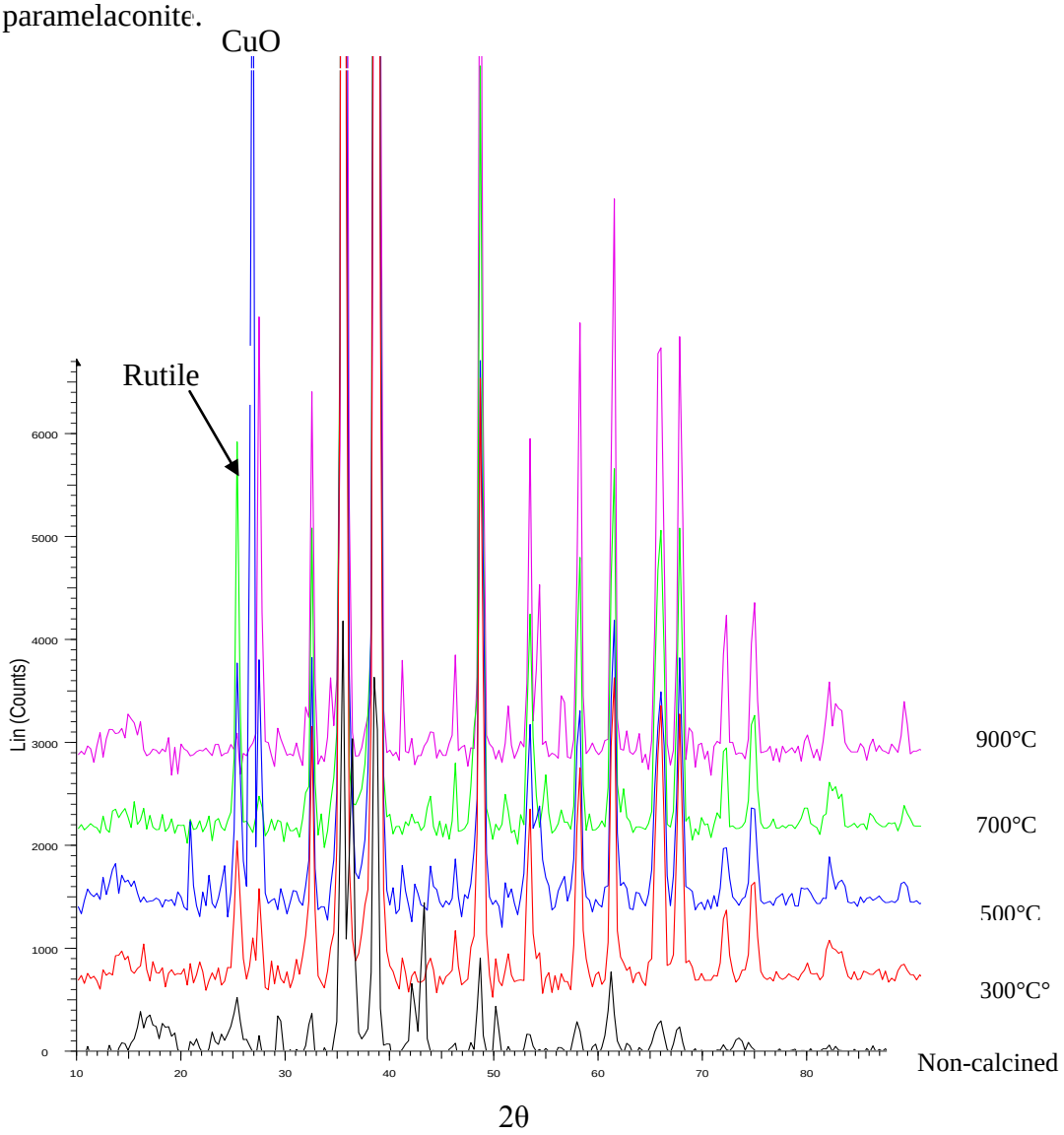

Figure 3.1. 3: X-ray diffraction patterns of the precursor powders of percentage composition 10% Ti and 90% Cu.

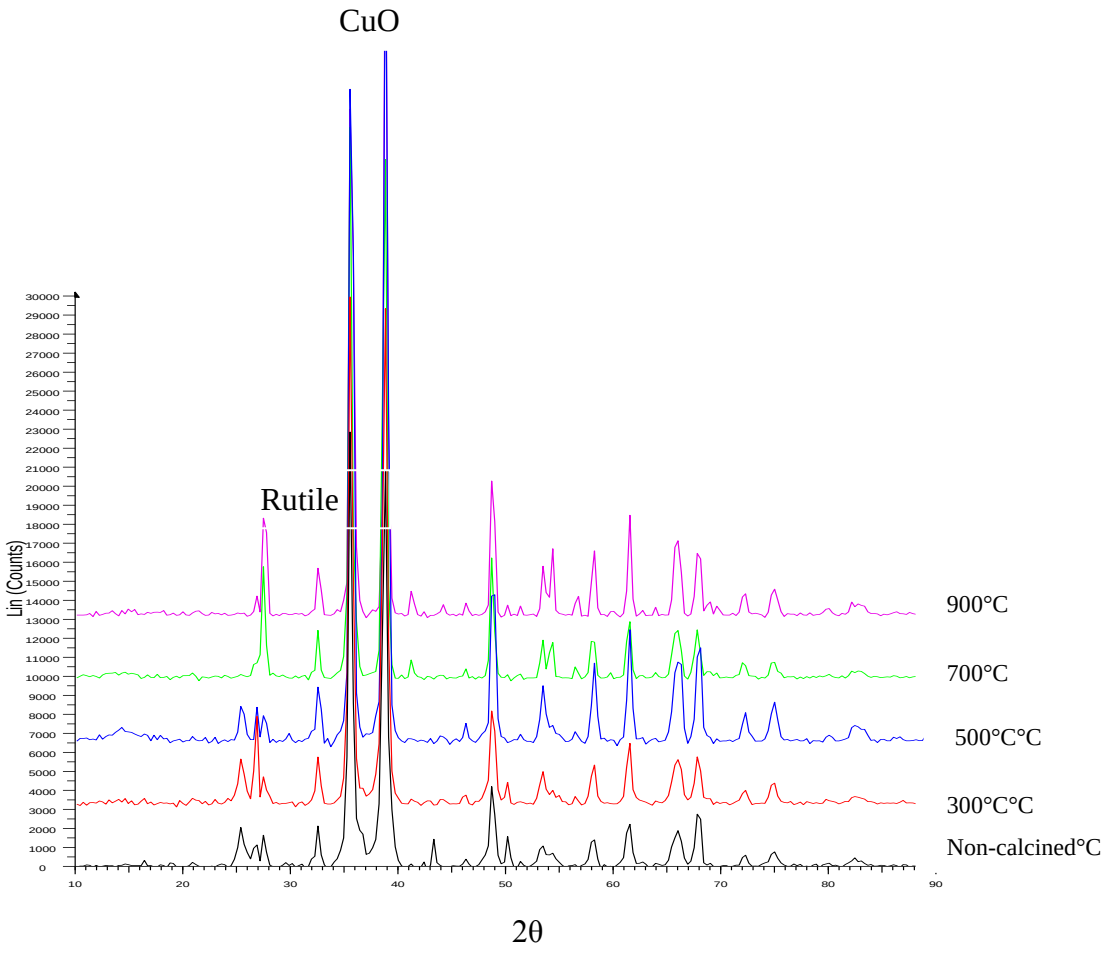

Figure 3.1. 4: X-ray diffraction patterns of the precursor powders of percentage composition 15% Ti and 85% Cu.

v) Trends in the 20% Ti: 80% Cu

Figure 3.1.5 below presents the first peak in the PXRD patterns of this composition occurring at 26° on 2θ scale in the non-calcined sample and at temperatures 300°C, 500°C and 700°C. This peak is at very low intensity and matched the titanium dioxide polymorph anatase peak. At 700°C, another peak appeared immediately at the foot of the anatase peak as presented in Figure 3.1.5 below. This peak occurred at 28° on the 2θ scale. It is of less intensity than that of anatase and identified a rutile peak. At 900°C, the anatase peak disappeared and the rutile peak dominated as the only TiO_2 polymorphic phase in the PXRD pattern of this composition. This implies that the rutile phase is more stable than the anatase phase at temperatures above 700°C. The rest of the peaks in the PXRD pattern of this composition presented in Figure 3.1.5 below are due to tenorite with multiphase identification of paramelaconite and

copper titanium oxide polymorphic phases on the major intense peaks occurring at 35.5° and 39° on the 2θ scale.

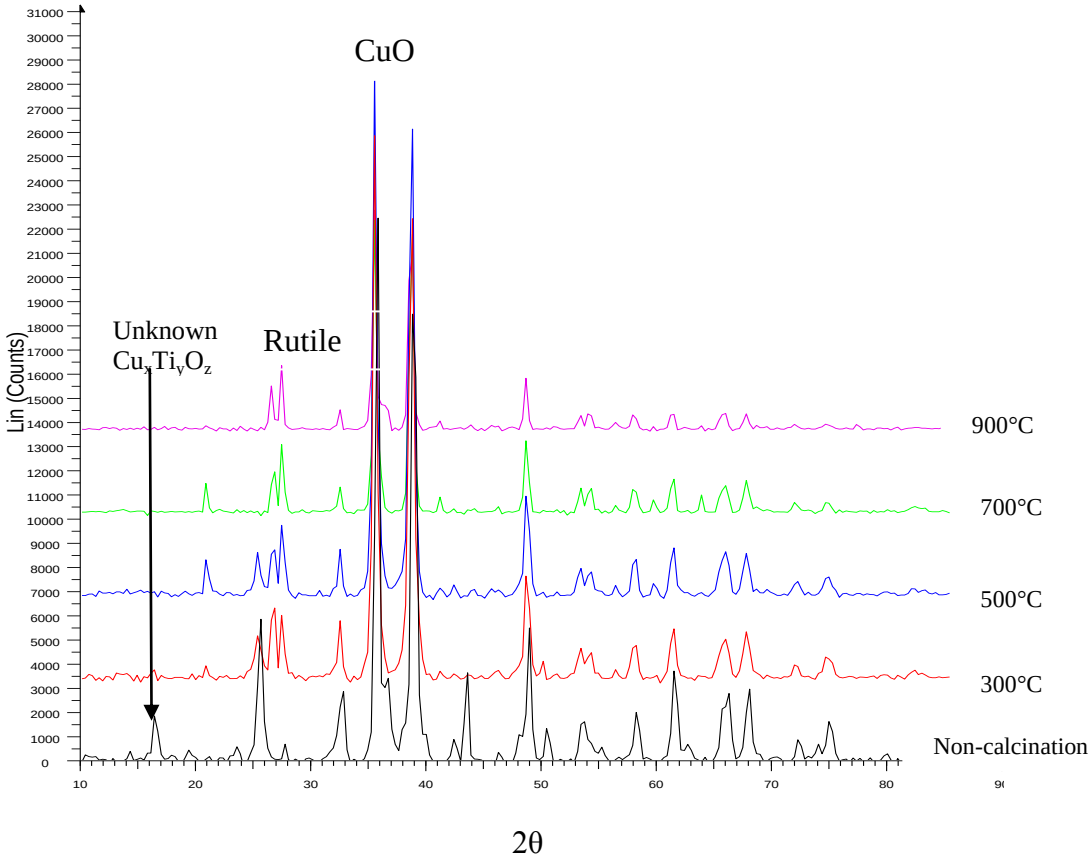

Figure 3.1. 5: X-ray diffraction patterns of the precursor powders of percentage composition 20% Ti and 80% Cu.

vi) Trends in the 25% Ti: 75% Cu

The non-calcined sample peak pattern has a small peak occurring at 16° on the 2θ scale of the PXRD pattern of this composition presented in Figure 3.1.6 below. The peak is of low intensity and did not identify with any polymorphic phases in the mixed metal oxide nanopowders in this sample mixture. However, this small peak immediately disappeared on calcination at 300°C.

The pattern of the non-calcined sample also indicates peaks of both anatase and rutile phases at 2θ 26° and 28° respectively. The anatase peak is more intense than the rutile peak as presented in Figure 3.1.6 below. The anatase peak became

progressively less intense while that of rutile intensified from the non-calcined sample up to the sample calcined at 700°C. At 900°C, the anatase peak disappeared and the rutile peak stood out as a pure phase of the TiO_2 polymorph.

The multiphase peaks at 2θ 36° and 39° in Figure 3.1.6 below identified the tenorite phase and the copper *(I)* oxide paramelaconite polymorph and the polymorphs of copper titanium oxides. The broadness of these peaks reduced with increase in calcination temperatures. At 900°C, pure phases of tenorite and rutile were identified from their peaks that distinctly stood out in the peak pattern at this temperature.

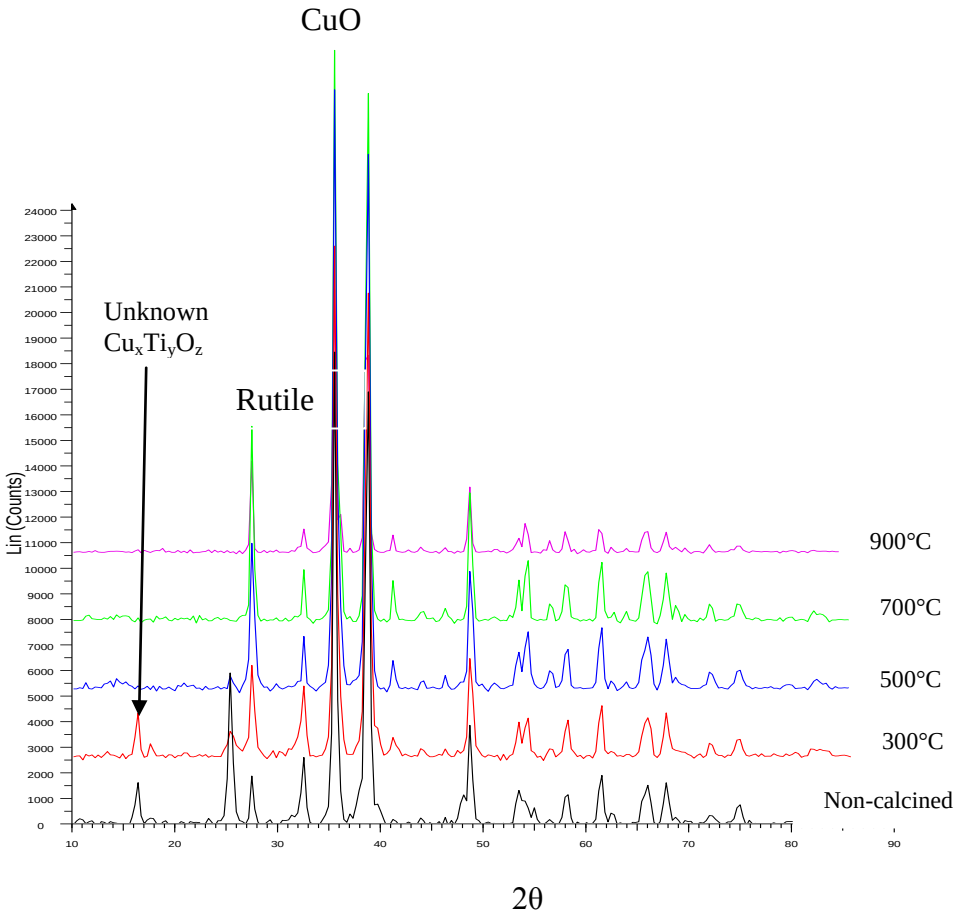

Figure 3.1. 6: X-ray diffraction patterns of the precursor powders of percentage composition 25% Ti and 75% Cu.

vii) Trends in the 30% Ti: 70% Cu

The phenomenon depicted and elucidated in the previous section at composition 25% Ti: 75% Cu continued in this sample composition. However, at 900°C calcination temperature, a small peak occurred at 2θ 26° and identified as an anatase peak. The peak is at very low intensity but represented a pure phase of this polymorph as presented in Figure 3.1.7 below.

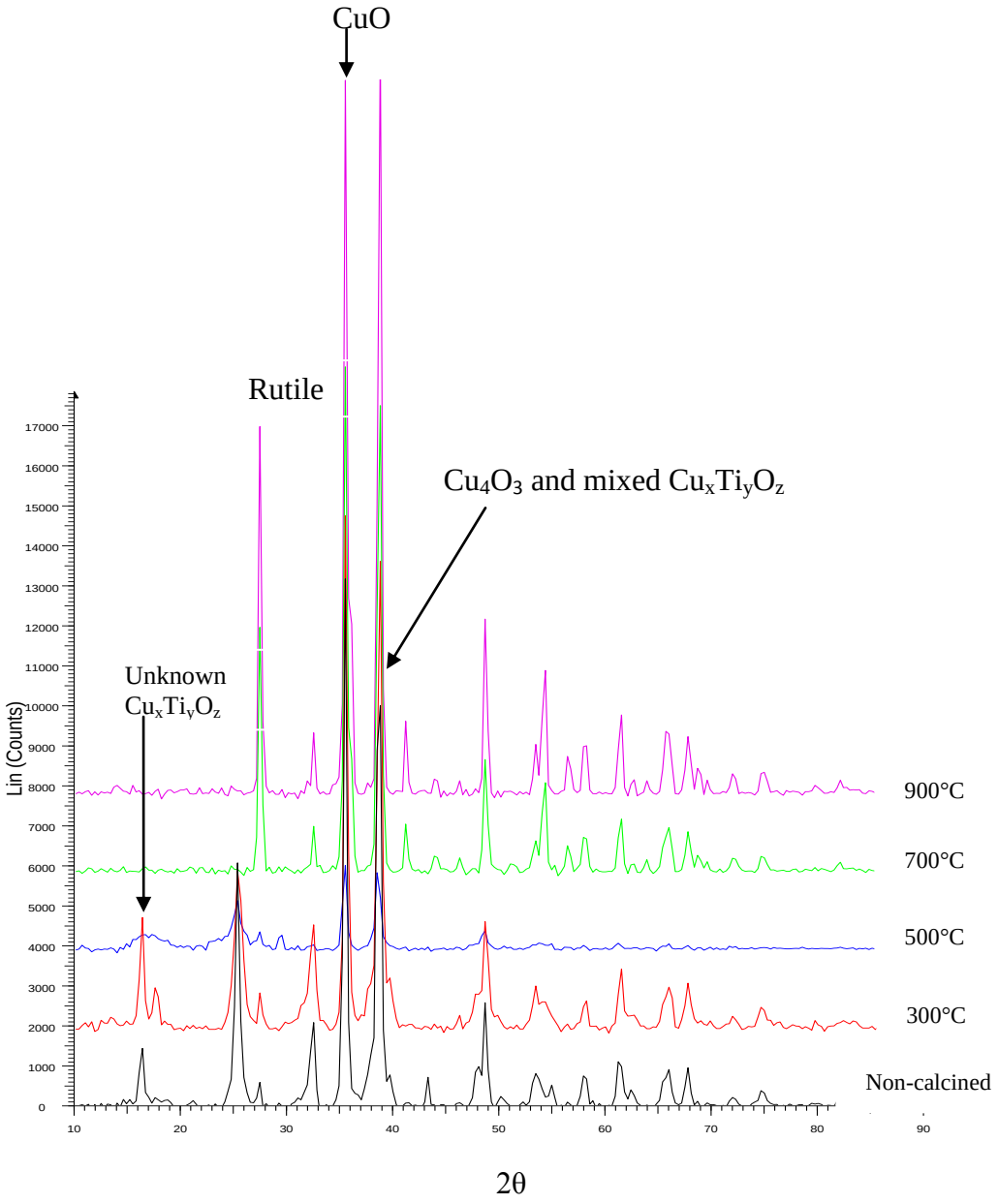

Figure 3.1. 7: X-ray diffraction patterns of the precursor powders of percentage composition 30% Ti and 70% Cu.

viii) Trends in the 35% Ti: 65% Cu

For the non-calcined sample, the small peak identified in the 25% Ti: 75% Cu and 30% Ti: 70% Cu compositions occurring at 16° on the 2θ scale was also observed in this sample as shown in Figure 3.1.8 below. At 300°C, this peak was very small and of insignificant intensity. At 500°C, its intensity further reduced to a very small peak and subsequently became indistinguishable at 700°C and 900°C.

From the non-calcined sample up to the sample calcined at 700°C, an intense peak occurred at 2θ 26° due to anatase phase as shown in Figure 3.1.8 below. A small peak occurred at 2θ value 28 and was of very low intensity in the non-calcined sample. It increased a little more in peak height through increased calcination temperatures up to 700°C. At 900°C, the anatase peak disappeared and the peak at 2θ 28° intensified and identified a rutile peak.

The peaks occurring at 36° and 39° on the 2θ scale in Figure 3.1.8 below are due to multiphase of tenorite, paramelaconite and polymorphs of copper titanium oxides. These peaks are broad and conjoined in the non-calcined peak pattern. The broadness reduced with an increase in calcination temperature. The peaks narrowed and separated at 900°C. At this temperature, all the copper titanium oxide polymorphs disappeared and the peak is attributable to pure phases of tenorite and paramelaconite.

Observations of a peak of considerable intensity identified at 2θ 44° matched an unreacted copper in this composition. This peak disappeared at 300°C and never appeared again at higher temperatures, implying that this unreacted copper turned to copper oxide on calcination of the sample.

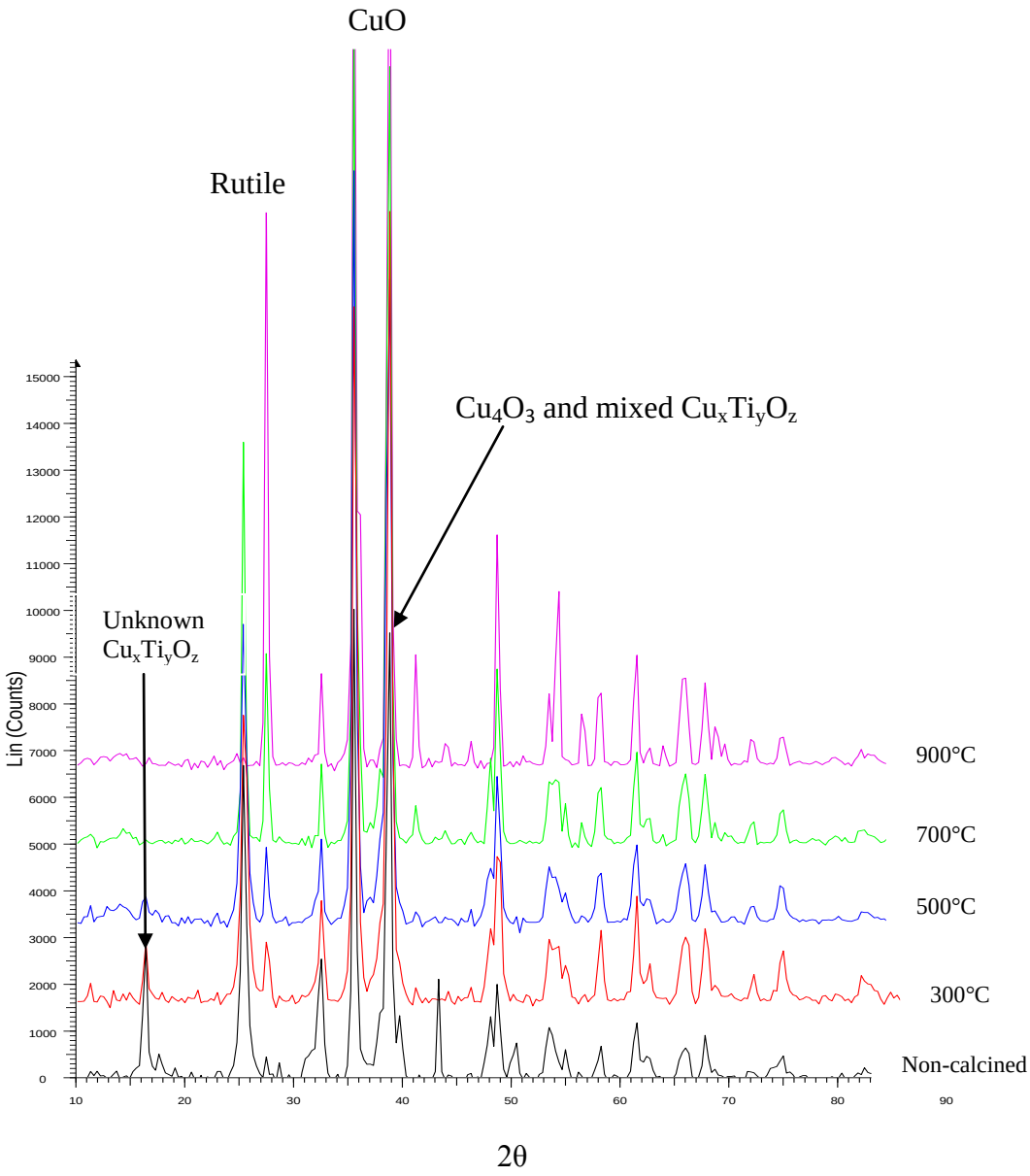

Figure 3.1. 8: X-ray diffraction patterns of the precursor powders of percentage composition 35% Ti and 65% Cu.

ix) Trends in the 40% Ti: 60% Cu

Figure 3.1.9 below shows a peak occurring at 2θ 17° in the PXRD patterns of the non-calcined sample. The peak is quite distinct and of substantial intensity. However, the peak completely disappeared at all calcination temperatures. The anatase peak intensified significantly with respect to the tenorite peak. This peak continued to increase in intensity with temperature so that at 700°C, it was the most intense peak in the peak pattern of the sample at this composition. At 900°C the anatase peak disappeared completely, implying the instability of this phase at higher calcination temperatures as shown in Figure 3.1.9 below. The rutile peak dominated as the only TiO_2 polymorphic phase below 30° on the 2θ scale. The

tenorite, paramelaconite and copper titanium oxide multiphased peak is a broad based low intensity peak. This peak narrowed at every increase in calcination temperature and further intensified so that it attained a great peak height at 900°C as shown in Figure 3.1.9 below.

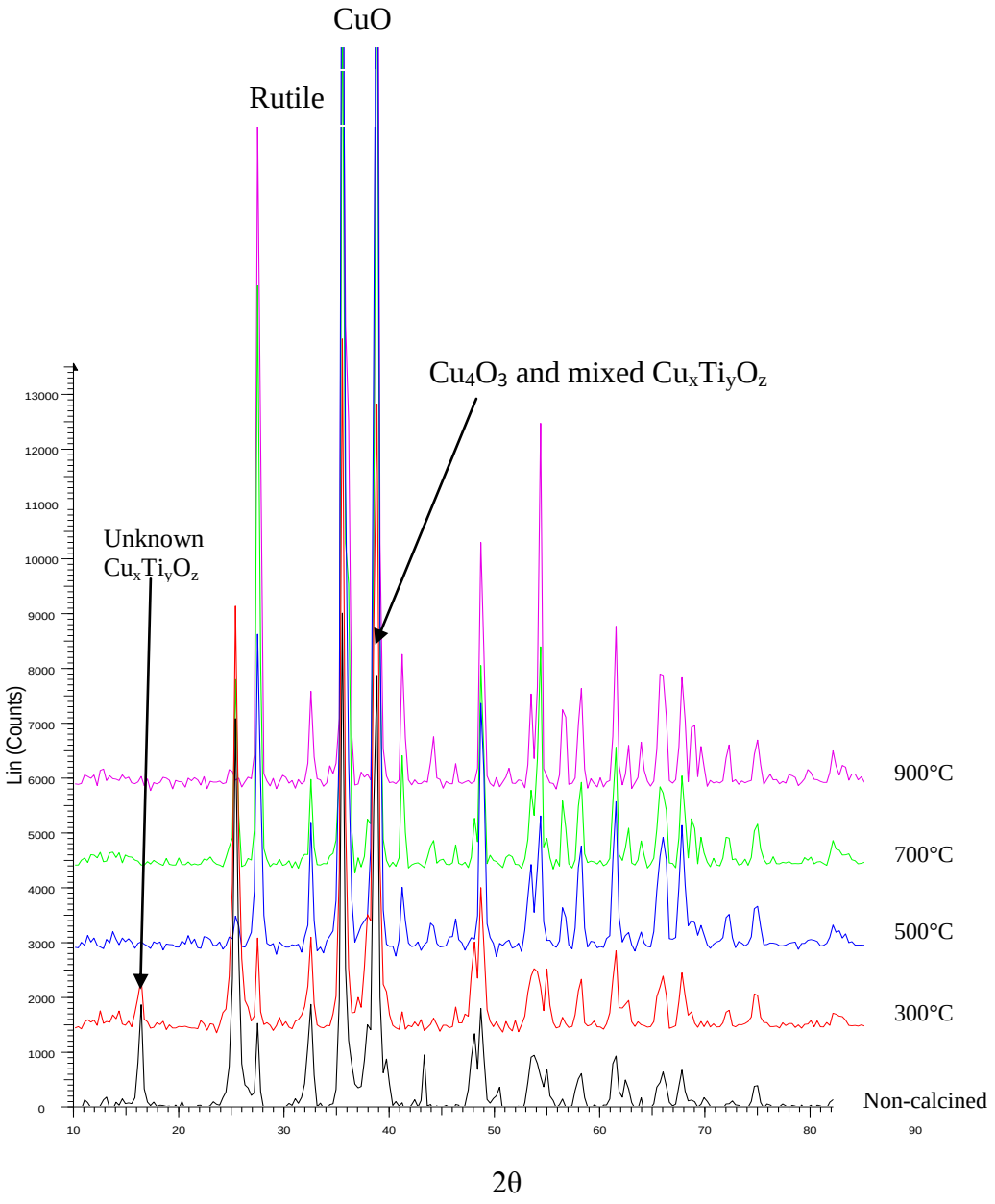

Figure 3.1. 9: x-ray diffraction patterns of the precursor powders of percentage composition 40% Ti and 60% Cu.

x) Trends in the 45% Ti: 55% Cu

The peak at 17° on the 2θ scale occurs distinctively at substantial intensity on the non-calcined sample peak pattern as shown in Figure 3.1.10 below. At 300°C calcination temperature, it diminished to a very small peak. Just like in the previous sample, the phase totally disappeared on calcining at higher temperatures

The anatase peak occurring at 26° on the 2θ scale started as a broad peak of almost the same intensity as that of the tenorite peaks in the non-calcined sample as shown in Figure 3.1.10 below. At 300°C, a small peak occurred right at the foot of the anatase peak and it was determined to be due to rutile phase. The peak persisted as a minute peak through higher calcination temperatures 500°C and 700°C. At 900°C, this peak intensified and attained great peak height with a distinct narrow base. Figure 3.1.10 below shows that the peak stood independently at 28° on the 2θ scale. The anatase peak disappeared completely at 900°C, implying that the anatase phase completely transformed to rutile phase at calcination temperatures above 700°C.

Figure 3.1.10 below shows the multiphased peaks occurring at 36° and 39° on the 2θ scale, which are less intense than in the previous sample compositions. This is attributed to the increase in Ti percentage ratio in the reaction mixture. The peaks are conjoined and have broad bases in the non-calcined sample. As calcination increased, the peak bases narrowed so that at 900°C, the peaks disjoined and identified a pure phase of tenorite. The phases of paramelaconite and copper titanium oxide polymorphs disappeared at this temperature.

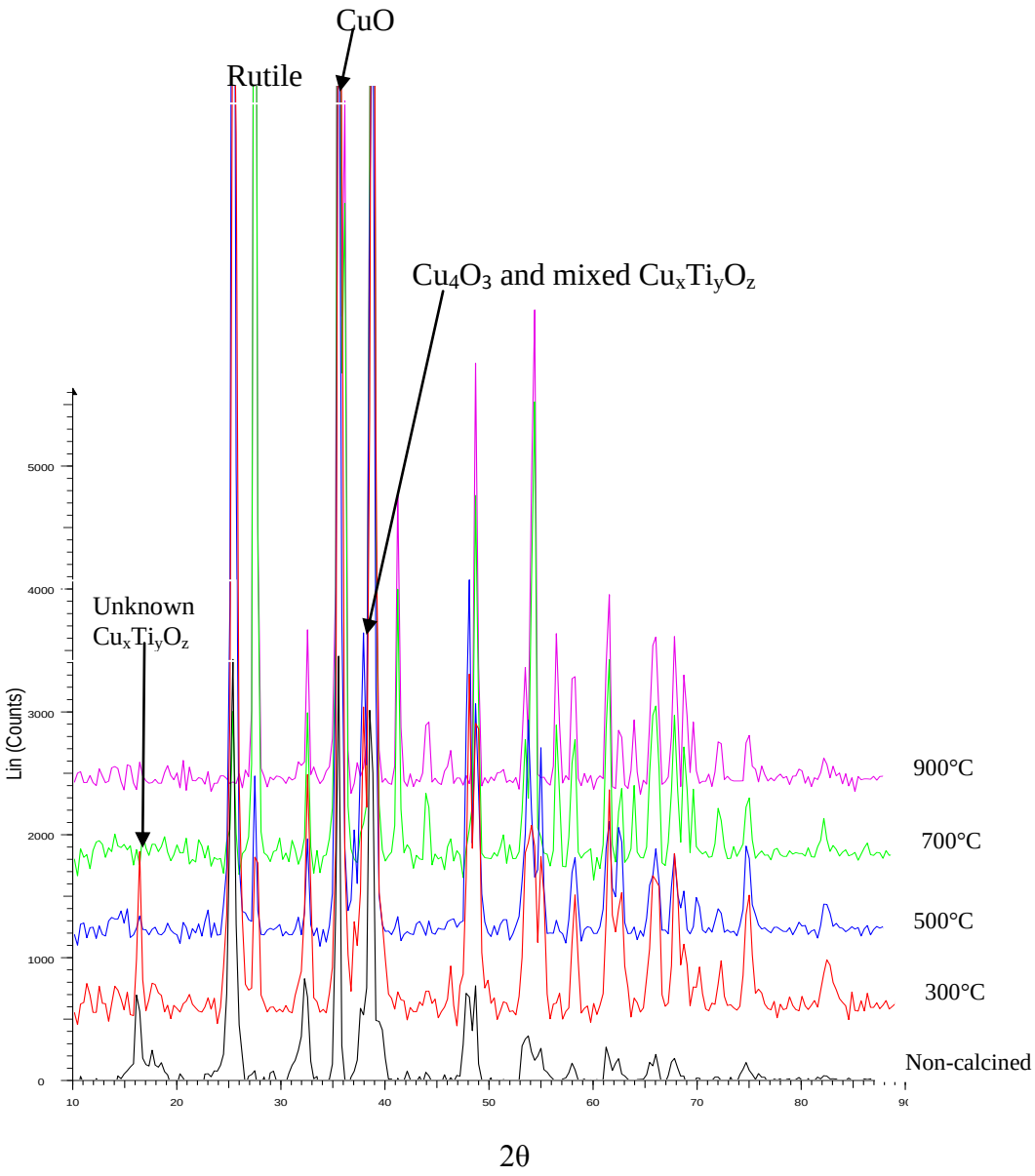

Figure 3.1. 10: x-ray diffraction patterns of the precursor powders of percentage composition 45% Ti and 55% Cu.

xi) Trends in the 50% Ti: 50% Cu

The peak at 17° on the 2θ scale has more intensity with a broad base in the non-calcined sample as shown in Figure 3.1.11 below. At 300°C, the peak significantly lowered in peak height and intensity. In subsequent samples at higher calcination temperatures, the peak became insignificantly small until it completely disappeared. The peak occurring at 26° on the 2θ scale has a broad base and is of higher intensity than any other peaks in the pattern of the non-calcined sample. This peak is due to the anatase phase and it persisted in samples

at calcination temperatures 300°C, 500°C and 700°C. Figure 3.1.11 shows that as the calcination temperature increased, there is a reduction in peak height to almost the same height as that of the tenorite multiphased peaks. A peak occurring at 33° on the 2θ scale initially exhibited contemporary peaks due to tenorite. However, at this composition, the phase matching showed that the increased peak height is due to the occurrence of another phase more intense than the tenorite diffraction at this 2θ value. The peak identified an unknown phase of titanium oxide complex which diffracts x-rays much the same way as iron titanium oxide. The multiphased peaks occurring at 36° and 39° on the 2θ scale maintained the same levels of intensity as the non-calcined sample through higher calcination temperatures as shown in Figure 3.1.11 below. It is noticeable that these peaks showed significant changes in peak broadness from the non-calcined sample in which the peaks were quite broad and conjoined. This decreased as calcination temperature increased so that at 900°C, the peaks had narrow bases and separated.

xii) Trends in the 55% Ti: 45% Cu

The peak at 2θ 17° persisted at this composition except that it has a diminished intensity as shown in Figure 3.1.12 below. In the non-calcined sample, the peak is distinct and broad based. It further diminished at every increase in calcination temperature so that at 700°C, the peak diminished to insignificant levels. The peak at 2θ 26° is the anatase peak that has a broad base and is more intense than any other peak in the PXRD pattern of this sample as shown in Figure 3.1.12 below. At this composition, Ti is 10% more than Cu in percentage ratio, thus the peak due to TiO_2 polymorphic phase is more intense than the CuO polymorphs. The peak at 26° on the 2θ scale progressively increased in intensity throughout the calcination range of this analysis.

At 700°C, a small peak due to rutile occurred at 2θ 28°. Figure 3.1.12 below show that the peak is very small and indistinct. However, at 900°C the anatase peak completely disappeared while the rutile peak shot up to a very high intensity with a narrow peak and high peak height. The peak at 2θ 33° occurred in the

non-calcined sample and is due to the unknown phase of titanium oxide complex but at higher calcination temperatures, the peak diminished in intensity so that the persistence of the peak was due to the multiphased peak of tenorite phase as shown in Figure 3.1.12 below. The peaks at 36° and 39° on the 2θ scale in this composition are due to tenorite and the copper titanium oxide phases. As calcination temperatures increased, the peaks narrowed in base as shown in Figure 3.1.12 below such that at 900°C the peaks disjoined to free standing peaks of the multiphased oxides.

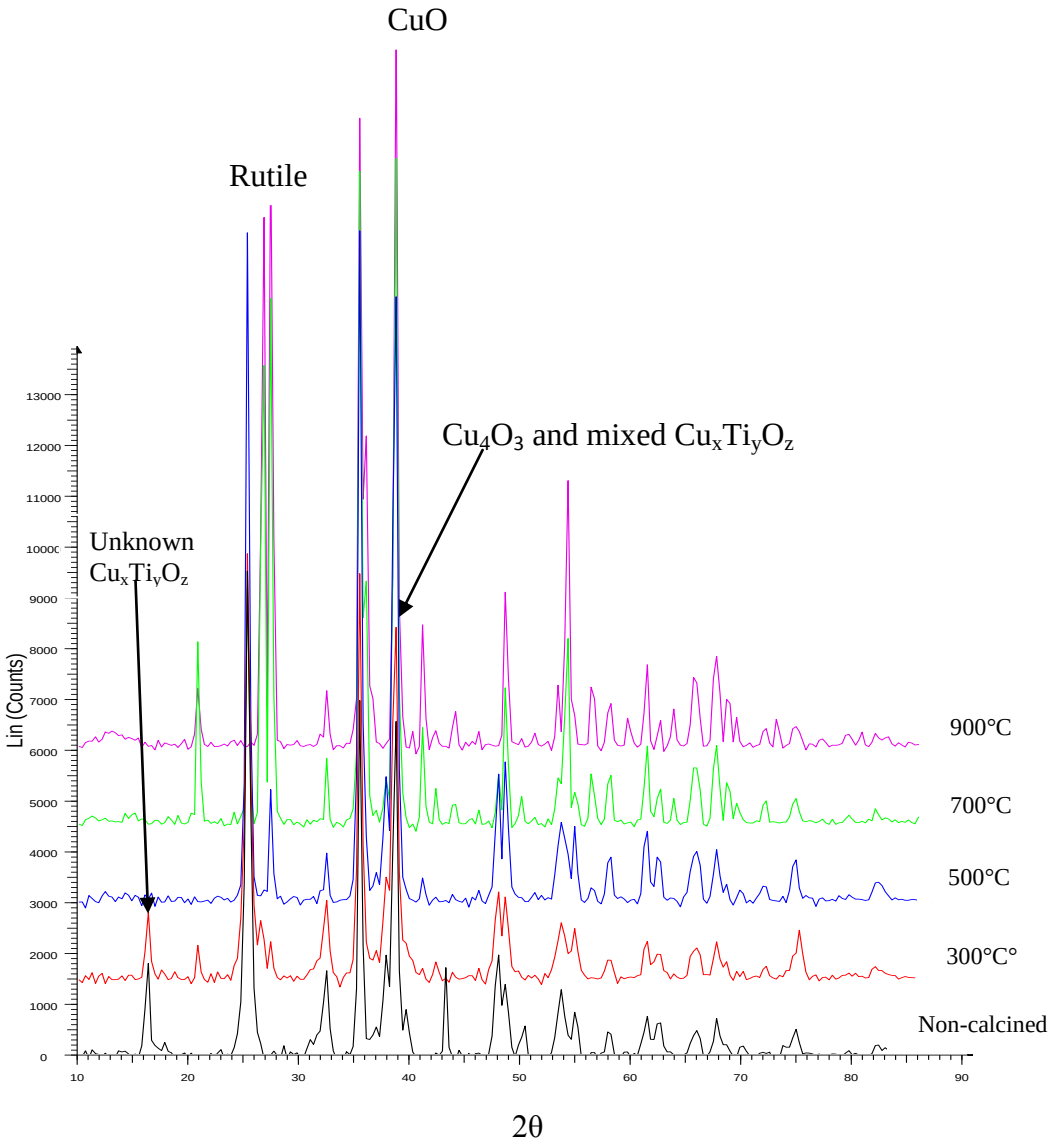

Figure 3.1. 11: X-ray diffraction patterns of the precursor powders of percentage composition 50% Ti and 50% Cu.

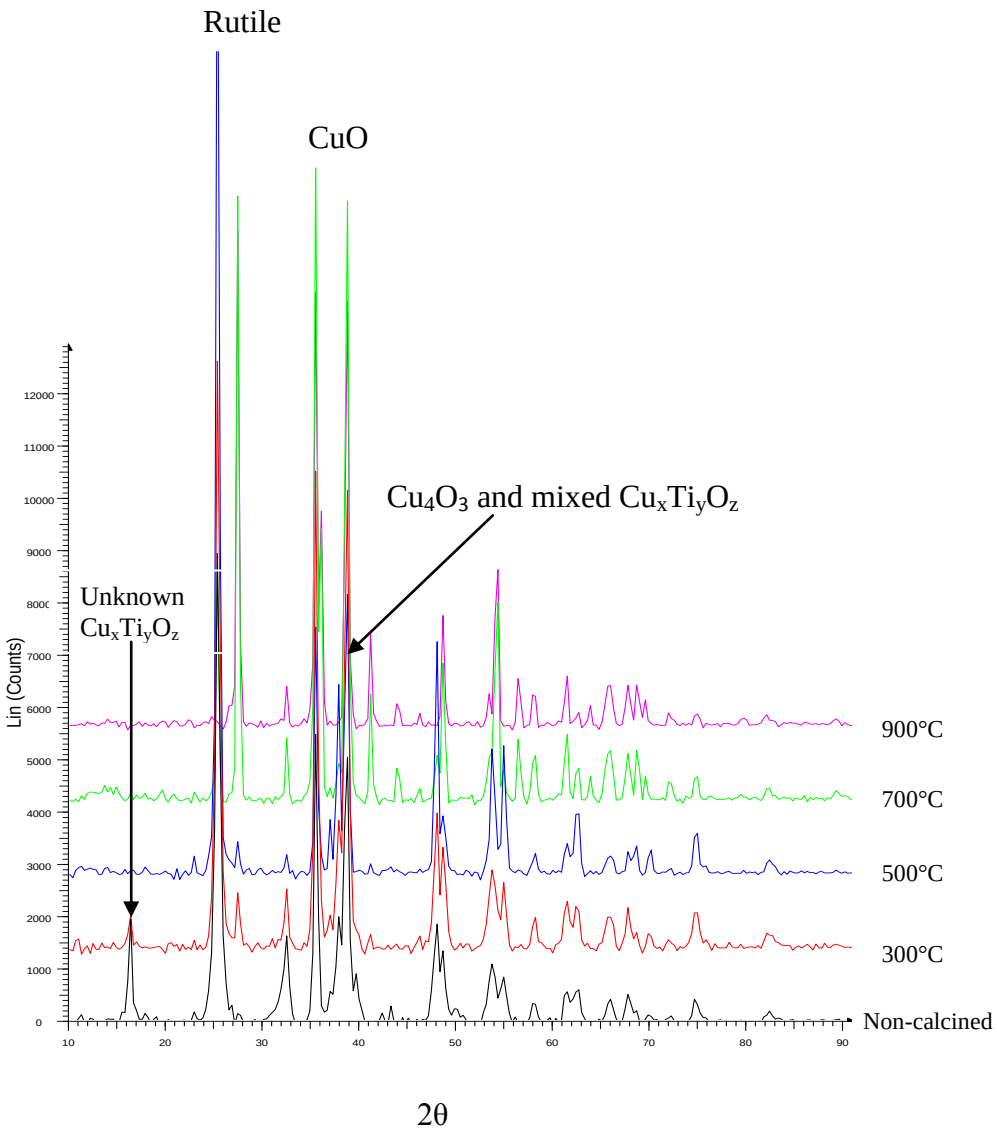

Figure 3.1. 12: X-ray diffraction patterns of the precursor powders of percentage composition 55% Ti and 45% Cu.

xiii) Trends in the 60% Ti: 40% Cu

At this composition, the peak at 2θ 17° is at high intensity compared to previous compositions as shown in Figure 3.1.13 below. It had a broad base and distinctively identified the unknown copper complex. This peak decreased significantly in peak intensity in the 300°C calcined sample. At 500°C, the peak further diminished to insignificant intensity levels. Further calcination at temperatures above 500°C resulted in the peak completely disappearing. The peak at 2θ 26° is a broad based anatase peak as shown in Figure 3.1.13 below. It is at higher intensity than any other peak in the PXRD pattern of the non-calcined sample and had a broad base that narrowed with the increase in calcination temperature. It maintained the high intensity levels at higher calcination

temperatures until 700°C, before it decreased to a very low intensity at 900°C. This is because most of the anatase phase transformed to rutile phase that gave rise to a very intense peak at 28° on the 2θ scale. The peak at 33° on the 2θ scale of the unknown phase of titanium oxide complex had a broad base and was of substantial intensity in the peak pattern of the non-calcined sample. It persisted in the sample calcined at 300°C but this phase disappeared at higher calcination temperatures as shown in Figure 3.1.13 below. The peaks at 36° and 39° on the 2θ scale due to tenorite and copper titanium oxide were broad based with short peak heights in the non-calcined sample. As calcination temperatures increased, the peaks narrowed and increased in peak heights as shown in Figure 3.1.13 below. This phenomenon can be explained in terms of Ostwald ripening as calcination temperatures increased.

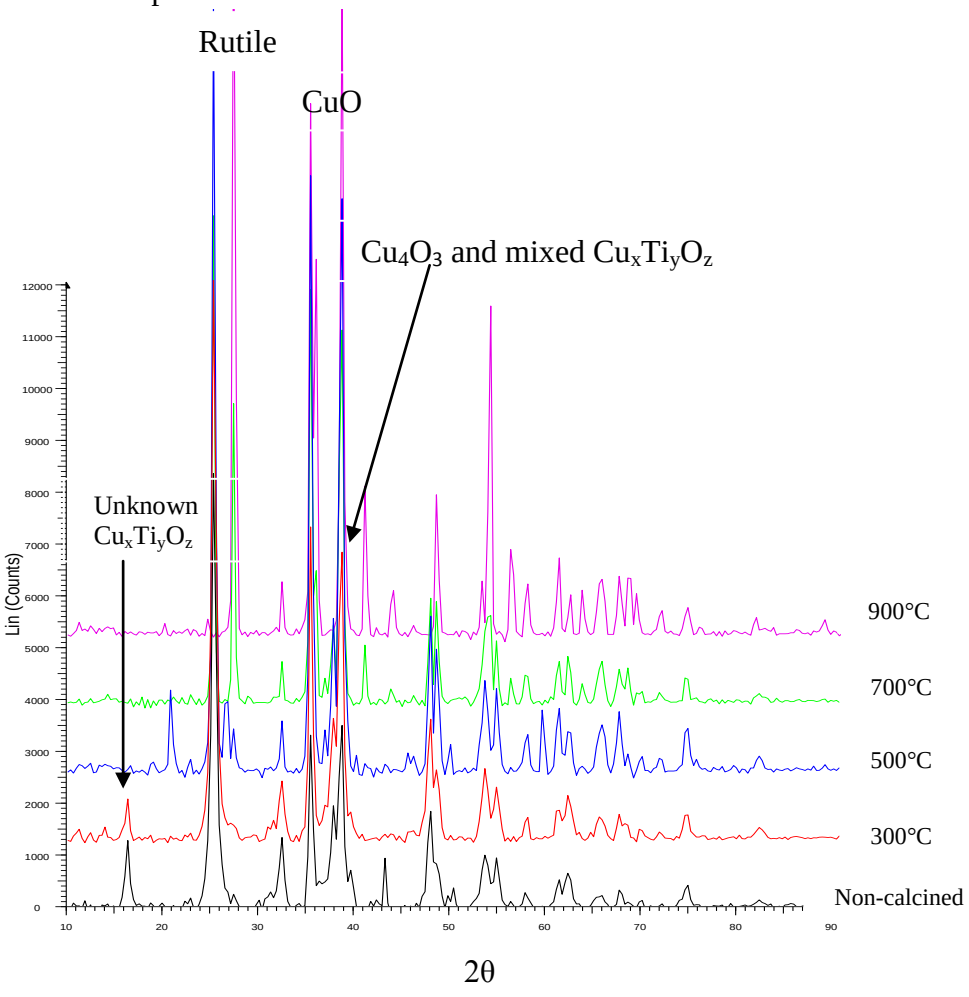

Figure 3.1. 13: X-ray diffraction patterns of the precursor powders of percentage composition 60% Ti and 40% Cu.

xiv) Trends in the 65% Ti: 35% Cu

Figure 3.1.14 below shows that the peaks at 17°, 26°, 33°, 36° and 39° on the 2θ scale were due to the same phases as explained in the trend of the previous sample composition. The peaks are due to unknown copper oxide complexes, anatase phase, unknown titanium oxide complex, tenorite phase and copper titanium oxide polymorphic phases respectively. This phenomenon occurred from the non-calcined sample to the sample calcined at 700°C in this sample composition. However, at 900°C, a unique peak occurred at 2θ 42° as shown in Figure 3.1.14 below. The peak identified with a multiphased peak of rutile and titanium copper oxide polymorphic phases. This peak is quite distinct and of substantial intensity. It is of interest that this peak never appeared at lower calcination temperatures even as a small pattern in their respective peak patterns.

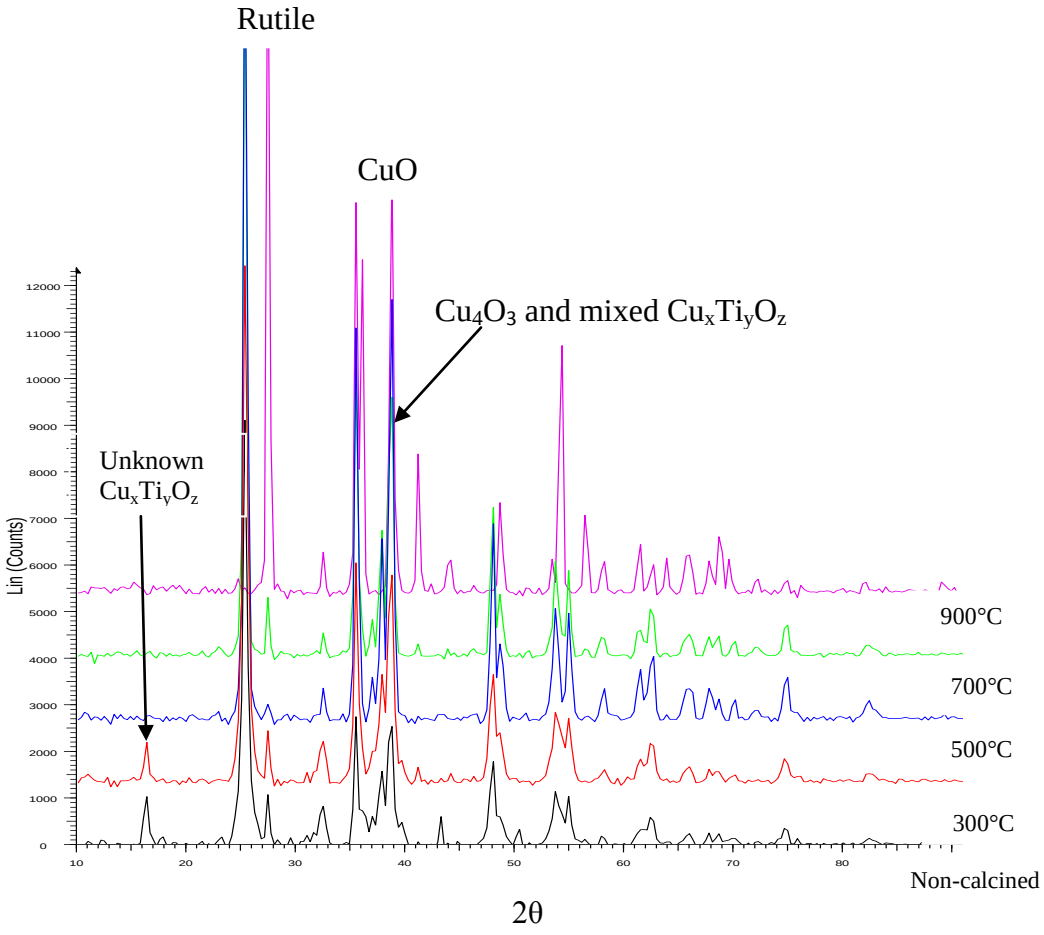

Figure 3.1. 14: X-ray diffraction patterns of the precursor powders of percentage composition 65% Ti and 35% Cu.

xv) Trends in the 70% Ti: 30% Cu

At this composition, the peak at 17° on the 2θ scale has a lower intensity than in the previous sample composition. However, it is still distinct as a peak identifiable with the unknown copper complex. Figure 3.1.15 below shows that the peak diminished in intensity with the increase in calcination temperature of the sample. At 700°C, the peak completely disappeared. The anatase peak at 26° on the 2θ scale has a broad base and is of high intensity as shown in Figure 3.1.15 below. This high intensity in the non-calcined sample persisted through higher calcination temperatures 300°C and 500°C. At 700°C, the anatase peak further intensified while its base narrowed. At 900°C, the anatase peak disappeared completely and an intense narrow peak of rutile phase occurred at 28° on the 2θ scale.

The peak at 33° on the 2θ scale of the unknown phase of titanium oxide complex occurred in the non-calcined and 300°C calcined sample. The peak then disappeared at higher calcination temperatures. This implies that the phase is unstable at higher temperatures so that it decomposed with the titanium forming anatase or rutile oxide. The peaks at 36° and 39° on the 2θ scale, due to tenorite and copper titanium oxide polymorphs are much smaller in peak height compared to their peaks in first sample compositions. The peaks now have even broader bases in the non-calcined sample. The peak bases narrowed as calcination temperatures increased but maintained a low intensity as shown in Figure 3.1.15 below. At 900°C, the intensity of these peaks increased to higher levels but identified only tenorite and one copper titanium oxide polymorph.

xvi) Trends in the 75% Ti: 25% Cu

The peak at 17° on the 2θ scale is smaller than in the previous peak patterns in the non-calcined sample as shown in Figure 3.1.16 below. This peak persisted at 300°C and 500°C before it completely disappeared at 700°C and 900°C. At 26° on the 2θ scale, a very intense peak and broad based anatase peak occurred. It persisted from the non-calcined sample through to the 700°C calcined sample.

This anatase peak disappeared at 900°C as it transformed to rutile phase that gave a very intense peak with a narrow base at 28° on the 2θ scale.

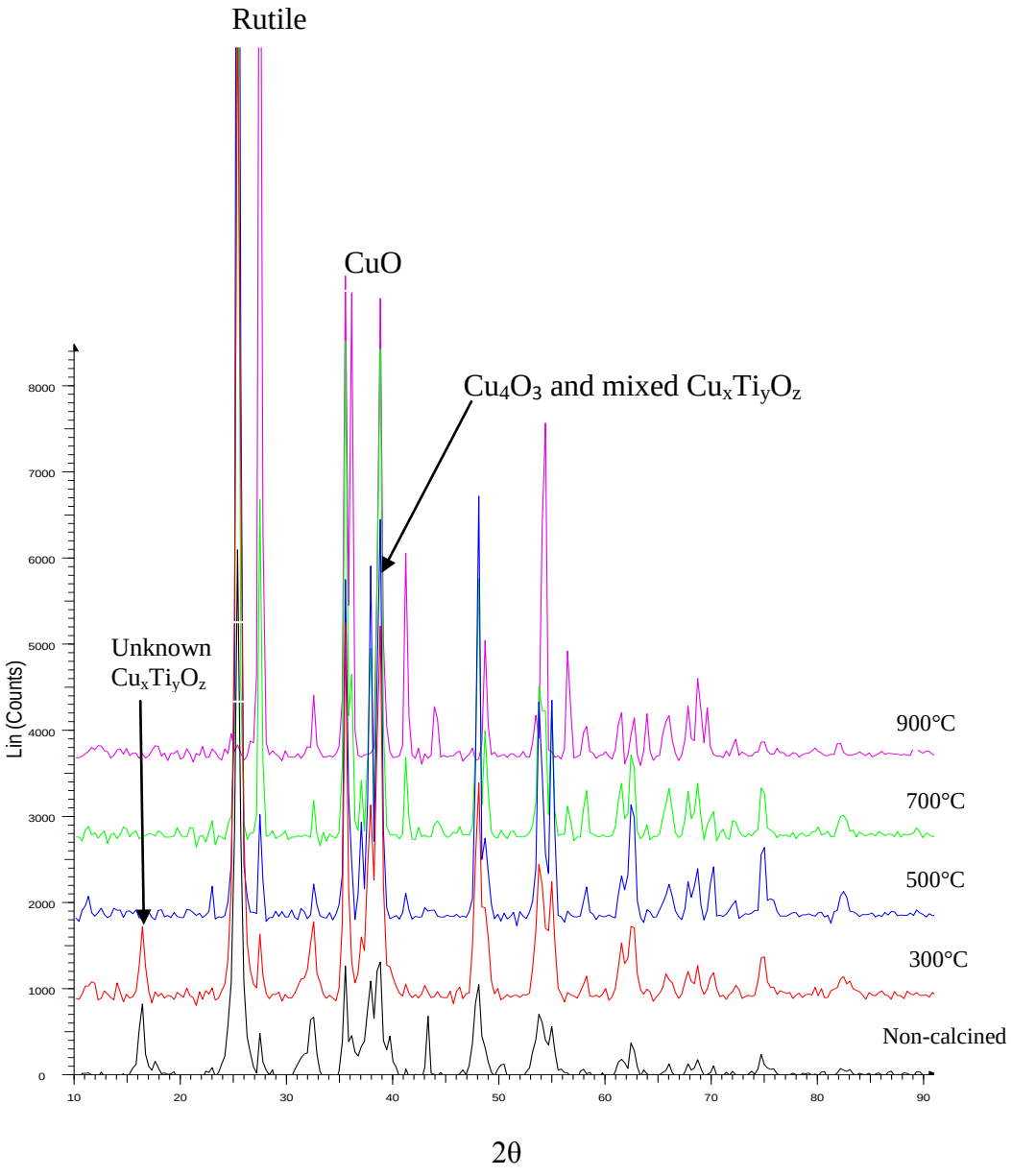

Figure 3.1. 15: X-ray diffraction patterns of the precursor powders of percentage composition 70% Ti and 30% Cu.

The peaks on 2θ 36° and 39° have bases that are broad and conjoined. The peaks are at very low intensity from the non-calcined sample through to the 700°C calcined sample as shown in Figure 3.1.17 below. The peaks identified tenorite, paramelaconite and copper titanium oxide polymorphs. At 900°C, the peaks intensified moderately and the peak bases narrowed and disjoined to give freestanding peaks that are distinct.

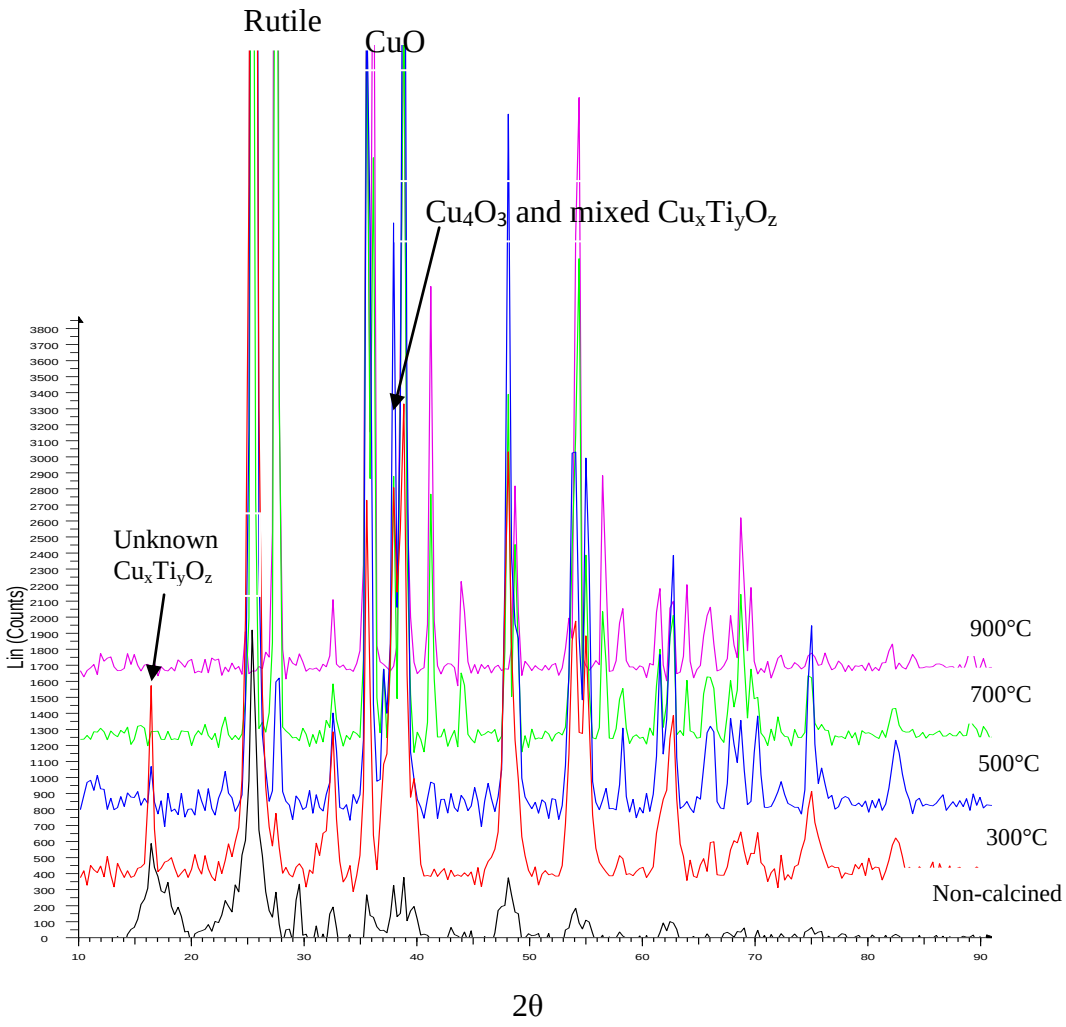

Figure 3.1. 16: X-ray diffraction patterns of the precursor powders of percentage composition 75% Ti and 25% Cu

xvii) Trends in the 80% Ti: 20% Cu

The peak at 17° on the 2θ scale is still persistent at this composition. It is at low intensity and has a narrow base as shown in Figure 3.1.17 below. As calcination temperatures increased, it further decreased in both peak intensity and peak broadness until it completely disappeared at 700°C. The anatase peak occurred at 2θ 26°. It had a broad base in the PXRD pattern of the non-calcined sample. Figure 3.1.17 below shows that the broad base narrowed as calcination temperature increased and had a high intensity until at 700°C where on further calcination, it completely turned to rutile phase giving rise to yet another narrow and intense peak at 28° on the 2θ scale. The peaks at 36° and 39° on the 2θ scale are broad and conjoined at their bases in the non-calcined sample as shown in

Figure 3.1.17 below. The broad peak bases narrowed with an increase in temperature so that at 900°C, the peaks disjoined to give freestanding peaks. The peaks were due to tenorite and copper titanium oxide phase. It is of interest that at this temperature, the paramelaconite phase no longer existed in the mixture of the metal oxides at this composition.

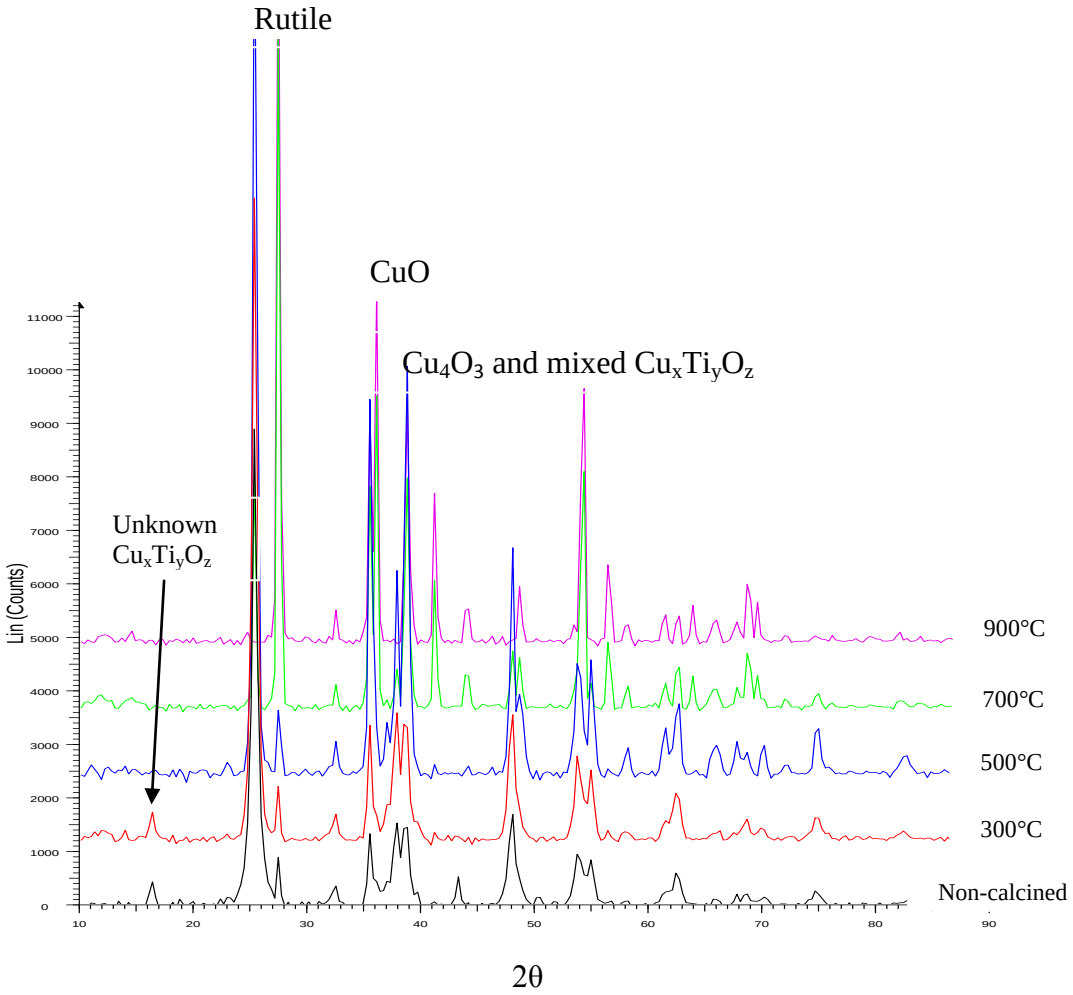

Figure 3.1. 17: X-ray diffraction patterns of the precursor powders of percentage composition 80% Ti and 20% Cu.

xviii) Trends in the 85% Ti: 15% Cu

At this composition, the peak at 17° on the 2θ scale persisted in the non-calcined sample up to the 500°C calcined sample as shown in Figure 3.1.18 below. The peak is at low intensity and further decreased in intensity to insignificant levels with an increase in calcination temperature. The anatase peak at 2θ 26° has a broad based peak at very high intensity in the non-calcined sample as shown in Figure 3.1.18 below. As calcination temperature increased, the base of this peak

narrowed as intensity remained high through the calcination temperatures up to 700°C. The peak shifted to 2θ 28° at 900°C as the anatase phase transformed to rutile phase that was equally intense as the anatase peak except that it had a narrower base. The peaks at 2θ 36° and 39° show that they are progressively decreasing in intensity with increase in the Ti percentage composition in the reaction mixture. The low intensity peaks in the non-calcined sample have broad bases and are at low intensity as shown in Figure 3.1.18 below. They persisted at higher calcination temperatures matching the existence of the phases, tenorite, paramelaconite and copper titanium oxide polymorphs.

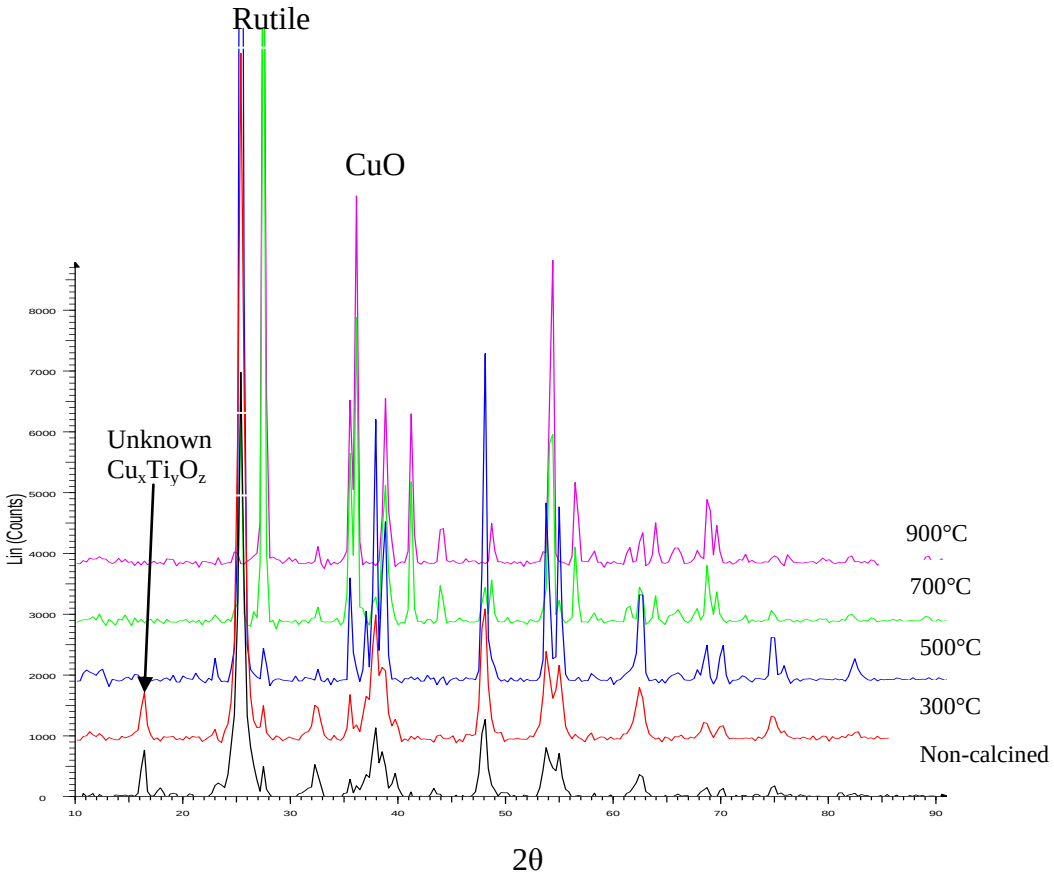

Figure 3.1. 18: X-ray diffraction patterns of the precursor powders of percentage composition 85% Ti and 15% Cu.

xix) Trends in the 90% Ti: 10% Cu

The peak at 2θ 17° at this composition is extremely small and indistinguishable from the non-calcined sample through to samples at higher calcination temperatures where it completely disappeared above 500°C as shown in Figure 3.1.19 below. They also show that the anatase peak at 2θ 26° is very intense,

reaching very high peak heights with a broad base in the non-calcined sample. At 300°C, a small peak due to rutile phase appeared right at the foot of the broad based intense anatase peak as a small finger at 2θ 28°. It persisted through higher calcination temperatures. Figure 3.1.19 below show that the peak shot up to high intensity at 900°C that saw the disappearance of the anatase peak as the anatase phase was all transformed to rutile phase. In the non-calcined sample, the tenorite peaks are appearing as a single broad peak spanning from 2θ 36° to 40°.

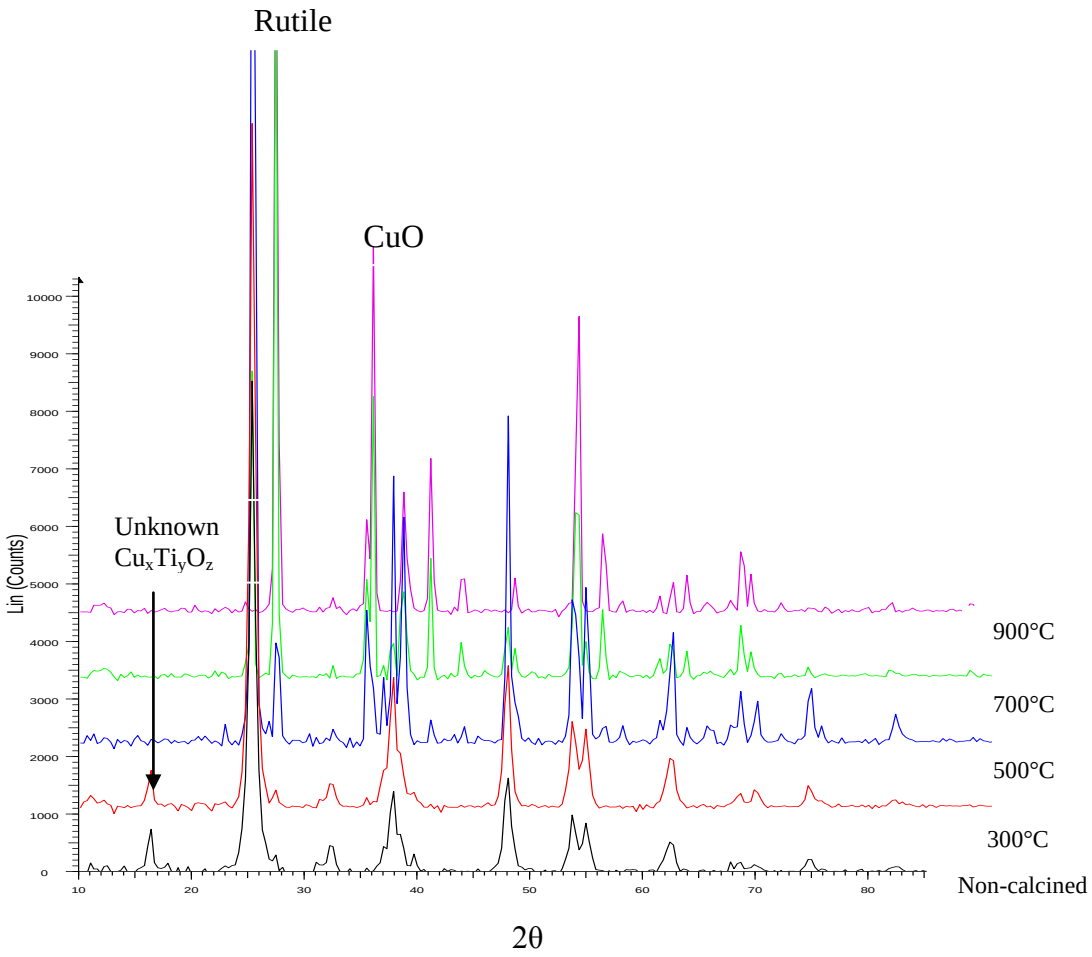

Figure 3.1. 19: X-ray diffraction patterns of the precursor powders of percentage composition 90% Ti and 10% Cu.

PXRD pattern peak matching identified a pure phase of tenorite only occurring from the non-calcined sample through to the sample calcined at 500°C. At 700°C, the peaks showed significant base narrowing and disjoining to three distinct peaks phase matched to tenorite and two phases of copper titanium oxide as shown in Figure 3.1.19.

xx) Trends in the 95% Ti: 5% Cu

The peak patterns in this composition portrayed much the same trends as in the previous sample composition as shown in Figure 3.1.20 below. However, the non-calcined sample had a small peak identified as due to rutile phase at the foot of the anatase peak at 2θ 28°. This peak persisted through higher calcination temperatures and it shot up to high intensity at 900°C when the anatase peak at 2θ 26° shifted to 28° on the 2θ scale with the transformation of anatase phase to rutile phase. The multiphased peak of tenorite and copper titanium oxide appeared as a single broad based peak that narrowed with increase in calcination temperature. At 900°C, the peak split into distinct separate peaks phase matched to tenorite, paramelaconite and copper titanium oxide as shown in Figure 3.1.20 below. The PXRD patterns of the samples at this composition show that residual peaks are very few along the 2θ scale as shown in Figure 3.1.20 below. The few residual minor peaks occurring in these patterns are at very low intensities compared to the minor peaks in previous compositions. At 900°C, these peaks narrowed at their bases while their intensities substantially increased. Figure 3.1.20 below show that this included the multiphased broad base peak of tenorite that separated to give three distinct peaks. The peaks identified polymorphic phases of tenorite, copper titanium oxide and paramelaconite.

xxi) Trends in the 100% Ti: 0% Cu

Figure 3.1.21 below shows that in this composition, the peak at 17° is non-existent in the samples at all the calcination temperature range. The peak pattern in the non-calcined sample shows a pure phase of the anatase phase with a major peak occurring at 2θ 26°. The peak is very broad at the base including its residual minor peaks. As calcination temperatures increased, all the peaks in the PXRD pattern narrowed in base and increased in intensity. At 700°C, the anatase peak is at its narrowest in peak base and shows that the phase is in its purest form. At 900°C, there is appearance of both the anatase and rutile phase peaks at 2θ 26° and 28° respectively. The peaks are distinct, intense and show the pure phases of these two polymorphic phases as shown in Figure 3.1.21

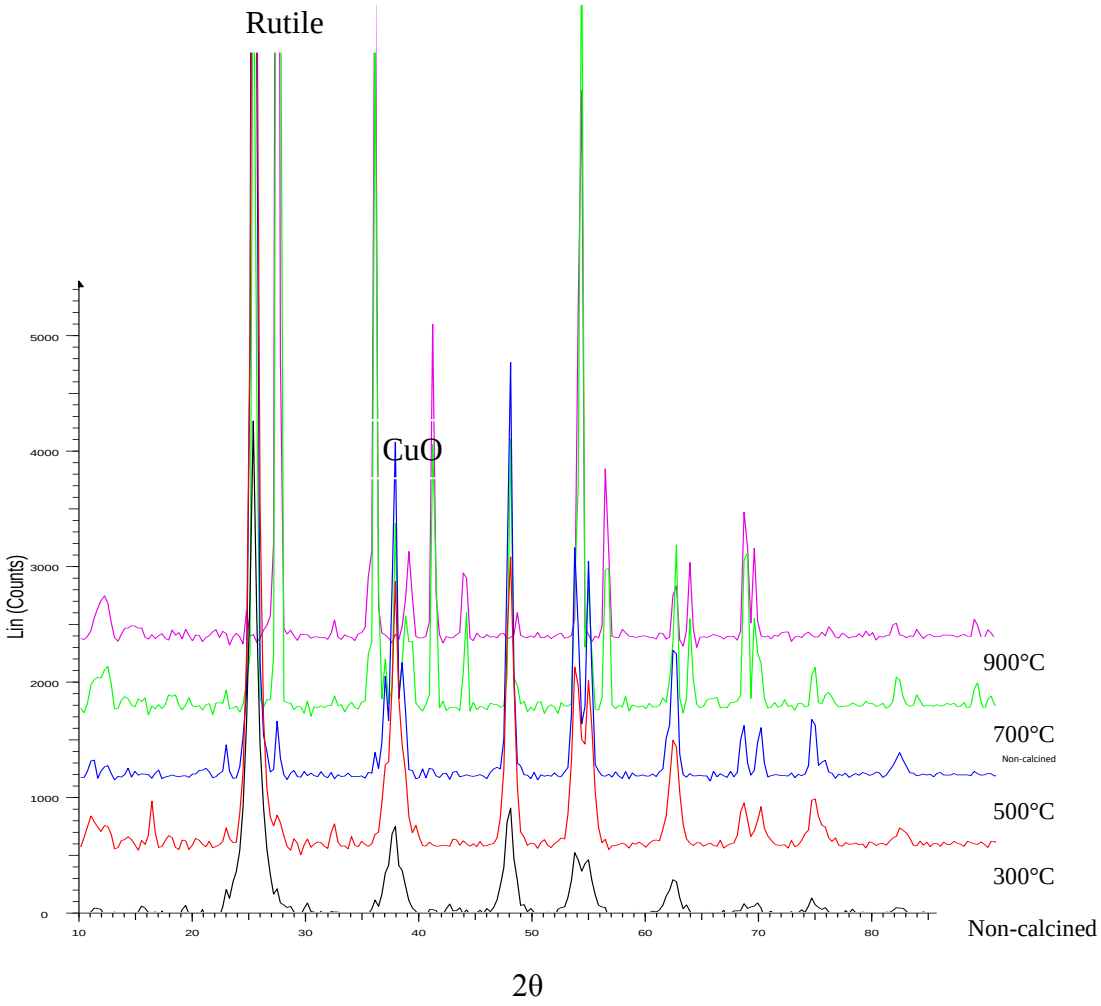

Figure 3.1. 20: X-ray diffraction patterns of the precursor powders of percentage composition 95% Ti and 5% Cu.

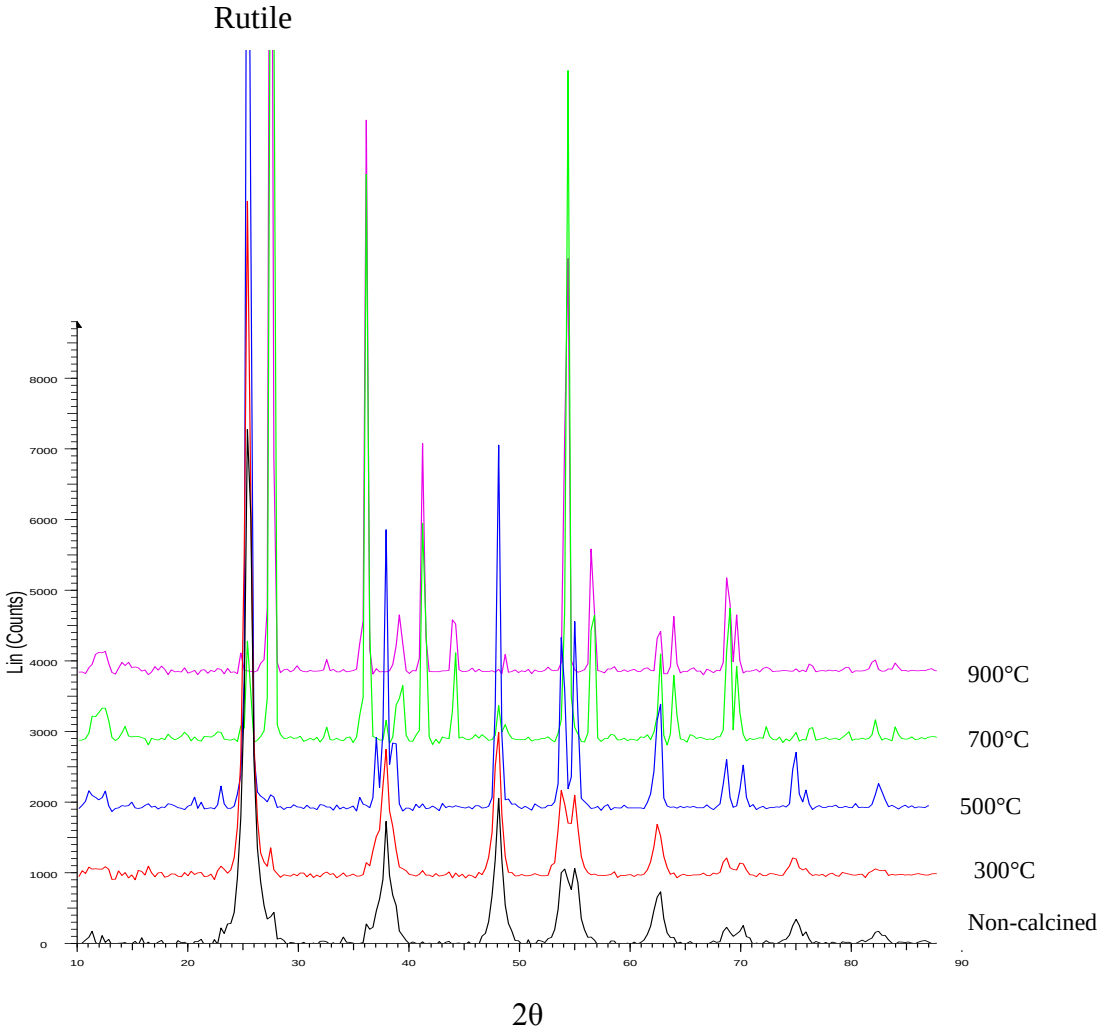

Figure 3.1. 21: X-ray diffraction patterns of the precursor powders of percentage composition 100% Ti and 0% Cu.

Chapter 4: Results and Discussion

4.1. Particle Size Analysis

Detailed analysis of particle sizes and determination of phase purities of crystallite phases synthesized using the resin-gel method of synthesis employed the PJF-X-ray Analyzer software. This program performs the mathematical calculations of determining particle size of nanoparticles using the Scherer's equation. In this research, the synthesis process produced multiphased or multicomponent mixtures of metal oxides. The X-ray analyzer enabled particle size determination of the respective oxides in the precursor powders from the PXRD peaks that identified with the crystallite phases. Tables 4.1 to 4.21 in Appendix G presents the particle size analysis of the crystalline phases of respective metal oxides occurring in the mixed-metal precursor powders. Tables 4.1 to 4.7 show particle size distribution of the crystalline phases in selected compositions. The first sample comprises of 100 % Copper so that the whole range of copper oxides occurring in the precursor powders appeared. Figure 4.1 shows the particle sizes of the crystal phases at different calcination temperatures at percentage composition 0 % Ti: 100 % Cu.

As temperature increased, the particle size of all crystalline phases generally increased, with a maximum particle size of 47 nm measured in the non-calcined sample for the cuprite phase as shown in Figure 4.1. The general increase in particle size in all the crystalline phases depicts Ostwald ripening patterns brought about by respective increase in calcination temperatures.[76] Figure 4.2 is showing particle sizes of crystalline phases occurring in samples at percentage composition 5% Ti: 95% Cu. The introduction of Ti generated phases due to TiO_2 and Cu_xTi_yO. The distribution of particle sizes shows the occurrence of these phases at respective calcination temperatures. It is of interest to note that even though the anatase particles had particle sizes as large as 21 nm, on transformation to rutile phase, the particles attained a maximum size of 4 nm at

this composition. However, all the crystalline phases exhibited a common trend in which particle sizes increased with an increase in calcination temperature.

Figure 4.4 shows particle sizes of both the unknown titanium and copper oxide complexes and Cu_xTi_yO phases at composition 15 % Ti: 85% Cu. These phases are occurring at different calcination temperatures. The unknown titanium oxide phase persisted from 15 % Ti: 85% Cu composition until in composition 75% Ti: 25% Cu where it last occurred. It occurred in both the non-calcined sample and the 300°C calcined sample. The unknown copper oxide complex phase persisted in this composition up to a sample with composition 85% Ti: 15% Cu in table 4.18 in appendix G where it also occurred in both the non-calcined sample and the sample calcined at 300°C. The particle sizes of these two phases ranged from 4 nm to 17 nm and the tables below show that the phases never occurred beyond 300°C calcination temperature.

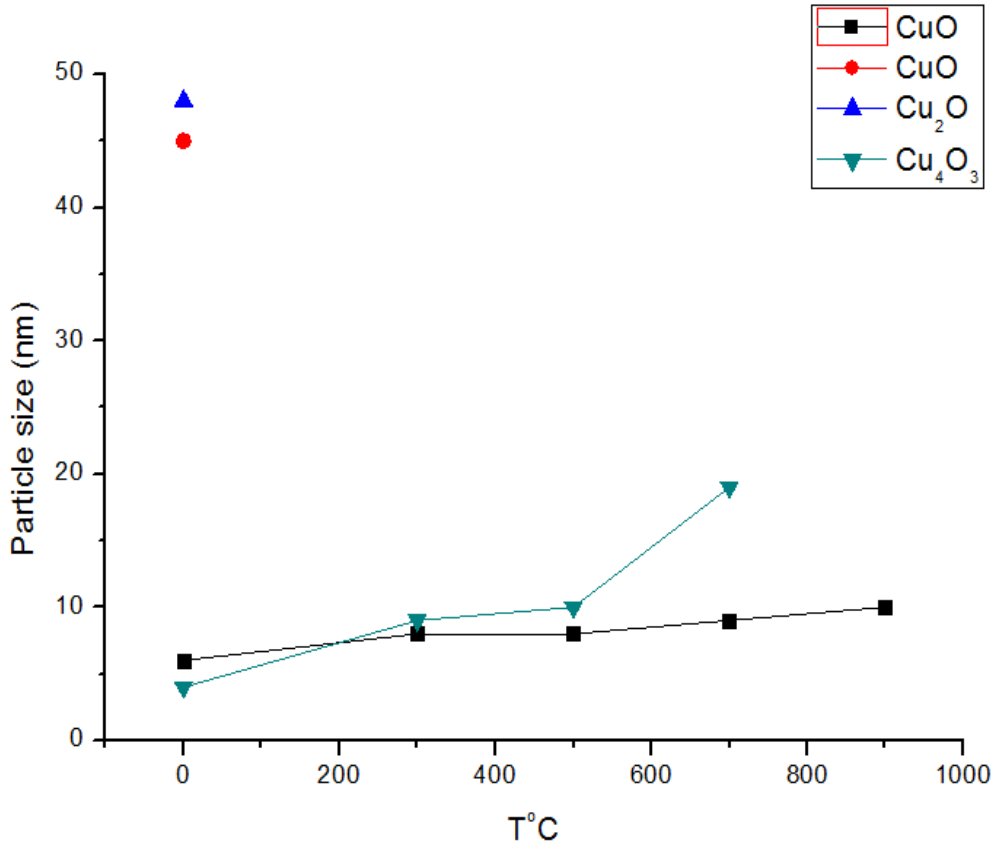

Figure 4.1: Particle size analysis for crystallographic phases in the precursor powde sample of composition 0 % Ti: 100 % Cu .

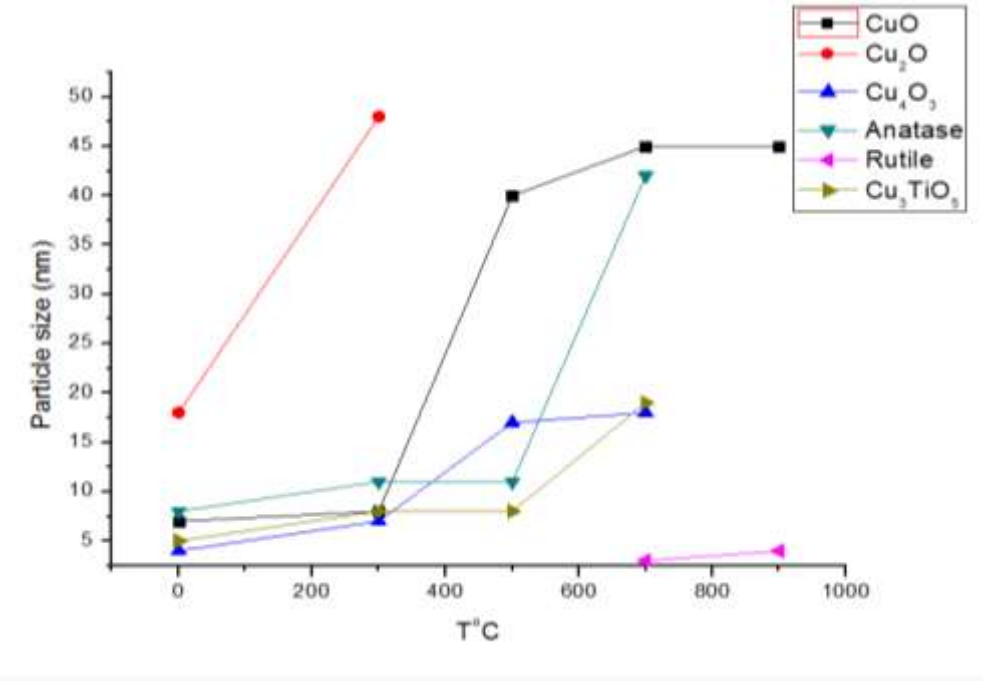

Figure 4.2: Particle size analysis for crystallographic phases in the precursor powder sample of composition 5 % Ti: 95 % Cu.

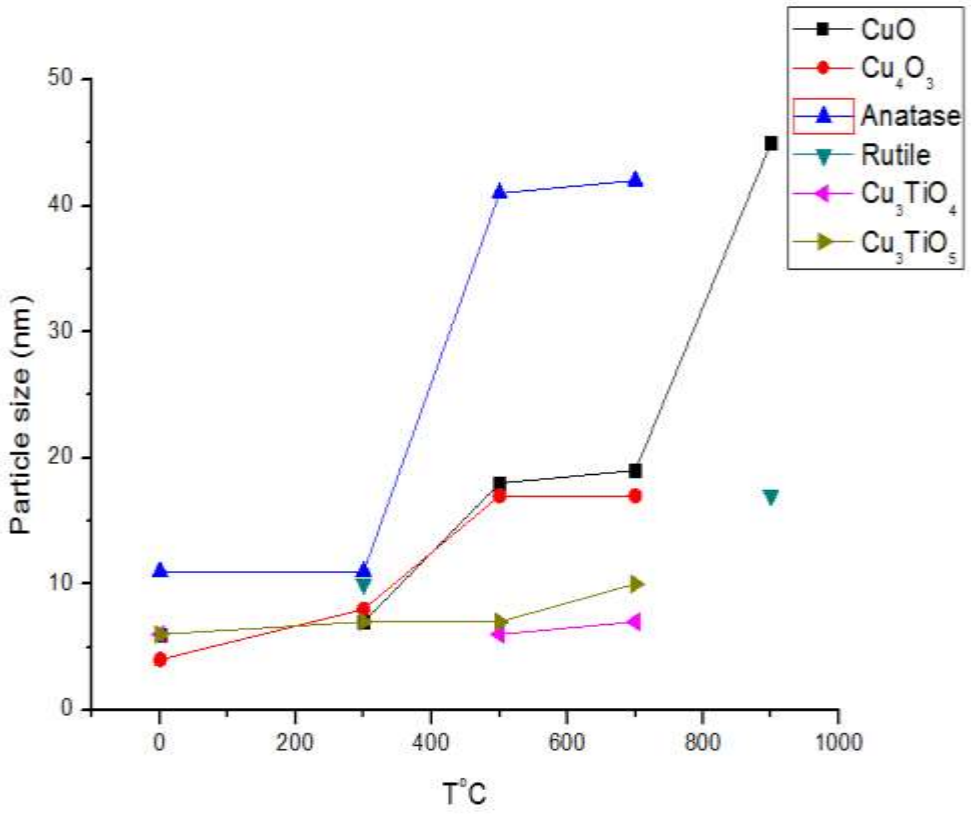

Figure 4.3: Particle size analysis for crystallographic phases in the precursor powder sample of composition 10 % Ti: 90 % Cu.

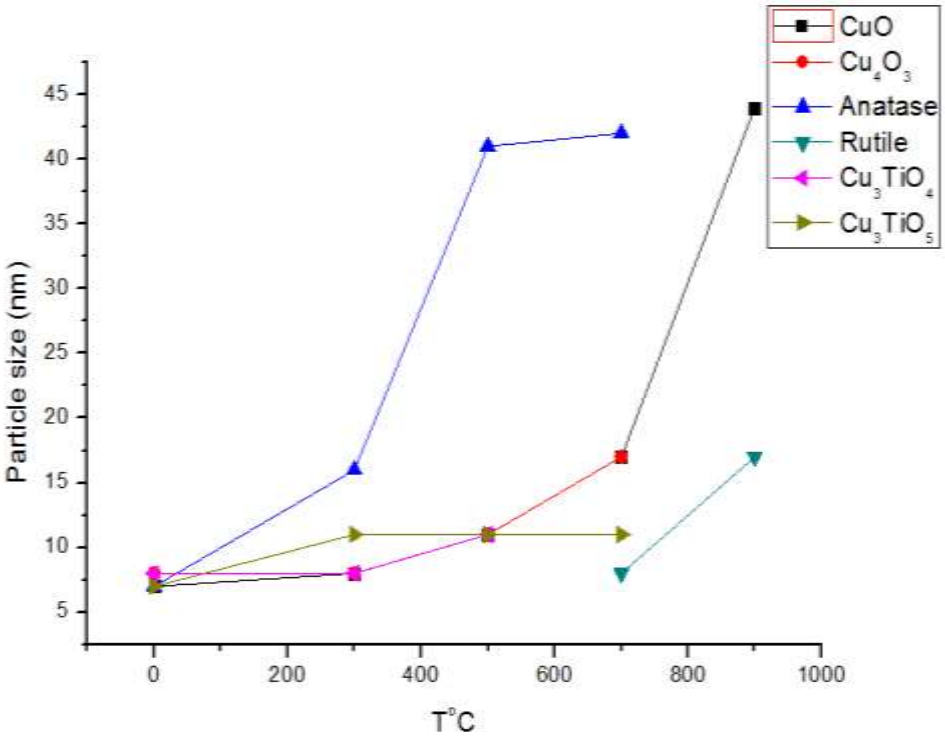

Figure 4.4: Particle size analysis for crystallographic phases in the precursor powder sample of composition 15 % Ti: 85 % Cu.

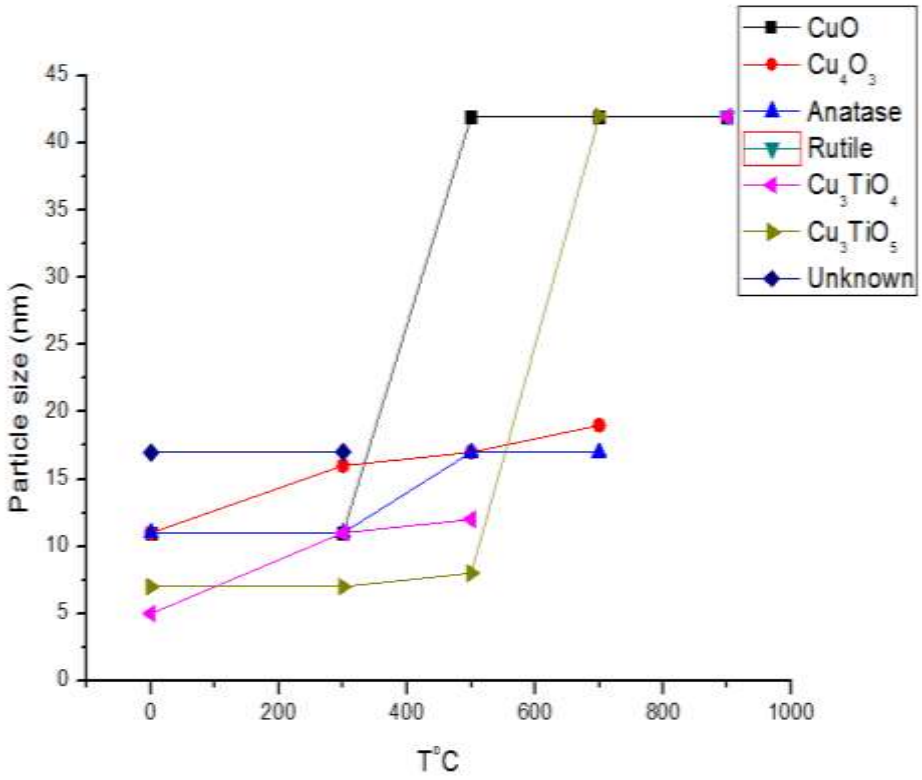

Figure 4.55: Particle size analysis data for crystallographic phases in the precursor powder sample of composition 50 % Ti: 50 % Cu.

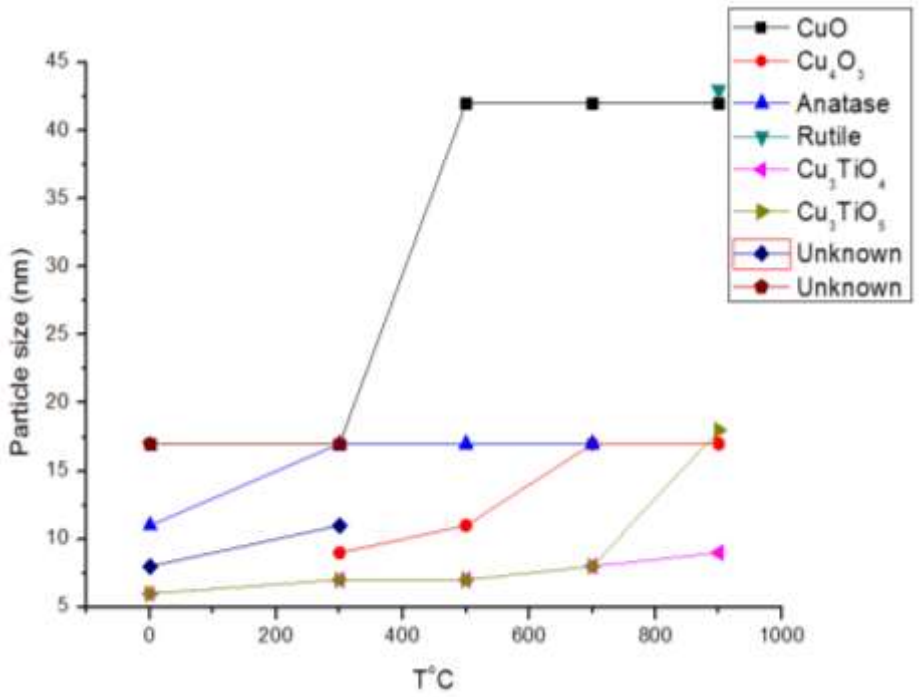

Figure 4.6: Particle size analysis for crystallographic phases in the precursor powder sample of composition 75 % Ti: 25 % Cu.

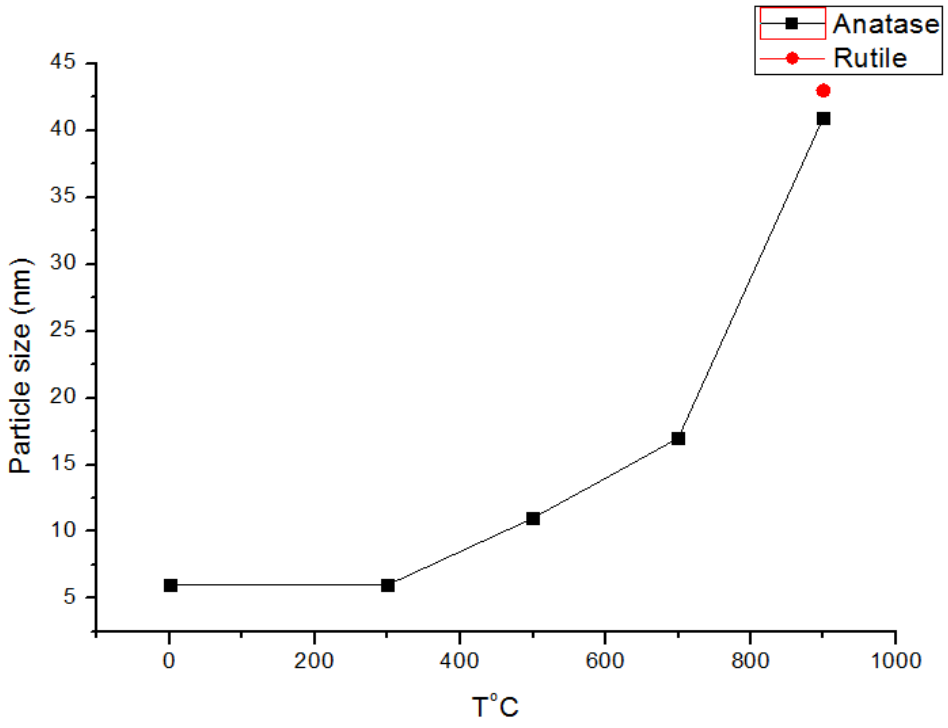

Figure 4.7: Particle size analysis for crystallographic phases in the precursor powder sample of composition 100 % Ti: 0 % Cu.

Phase matching of the PXRD peak patterns identified another unique phase of the copper (*I*) oxide polymorph called Paramelaconite (Cu_4O_3). This crystalline phase persisted in all calcination temperatures diminishing with a decrease in Cu percentage composition. However, paramelaconite (Cu_4O_3) exhibited a unique characteristic in which the particle sizes ranged from 10 to 19 nm throughout the whole calcination temperature range. Figure 4.2 above and tables 4.2 to 4.19 in appendix G shows the distribution of the paramelaconite (Cu_4O_3) phase across the calcination temperature range in respective sample compositions. It is apparent that the particle size of this phase also increased with an increase in calcination temperature. As the percentage of Cu composition decreased, the phase tends to occur at higher calcination temperature as shown in Figures 4.1 to 4.4 above and tables 4.16 to 4.19 in appendix G. Its particle sizes continued to take higher values at higher calcination temperature.

With the introduction of Ti, TiO_2 phases formed and showed some trends due to both temperature and compositional variations.[77] Figures 4.5 and 4.6 above and table 4.6 in appendix G shows that the anatase phase occurred from the non-calcined series to the 700°C-calcined series. Tables 4.2 to 4.21 in appendix G shows particle size of TiO_2 anatase phase increasing with an increase in temperature as shown in Figure 4.7 above. In the non-calcined series, most particles had particle size around 10 nm increasing through the 16 nm sizes in the 300 and 500°C to a high particle size of around 17 nm in the 700°C series. The table also shows that the particle size of TiO_2 anatase crystalline phases was not subject to percentage composition of Ti in the reaction mixture. However, at 900°C, TiO_2 anatase phase persisted only at 100% Ti while at other compositions the crystalline phase turned into rutile.

The phenomenon described above is completely the opposite of the particle size distribution of rutile crystalline phase of the TiO_2 polymorph as shown in table 4.6 in appendix G. In the non-calcined series, the rutile phase occurred incidentally only at 25 % Ti composition. The particle size of these particles is very small at 4 nm to 42 nm while it does not exist at other Ti percentage compositions at calcination temperatures below 700°C. This phenomenon is

attributable to a decomposition pathway of an unknown Cu_xTi_yO phase. This implies that the TiO_2 rutile phase is thermodynamically stable only at high temperatures.[78] At 300 to 500°C, the rutile TiO_2 crystalline phase is also occurring intermittently at very few instances meaning that these calcination temperatures do not support this crystallographic phase. At 700°C, the rutile phase occurred in the first half of the series with particle sizes ranging from 4 to 42 nm. At higher Ti percentage composition, the phase did not persisted in occurrence because at this temperature, the TiO_2 does not sufficiently transform into rutile phase but remained predominantly in the anatase phase.

At 900°C, the particle size of the TiO_2 rutile phase increased with increase in calcination temperature. The crystallite sizes are generally around 23 nm and occurred at every Ti percentage composition down the series. This phenomenon entails the optimum temperature that allows the transformation of the TiO_2 to the rutile crystallographic phase.[79] The temperature is above 700°C and produced crystals of significantly high particle sizes as shown in table 4.18 above. Tables 4.2 to 4.20 in appendix G show the particle size distribution of the crystallographic phases of Cu_xTi_yO phases Cu_3TiO_4, Ti_3Cu_3O and Cu_3TiO_5 respectively. In tables 4.8 to 4.10, the crystallographic phase Cu_3TiO_4 occurred across the whole calcination temperature range except in the 700°C series. The particle size of the crystals varied in range at different calcination temperatures.

Tables 4.2 to 4.6 and 4.15 to 4.20 in appendix G show the distribution of the crystallographic phase Ti_3Cu_3O. It is of interest to note that this phase did not occur at all in the 500°C series. In other calcination temperature series, it occurred incidentally with the greatest frequency in the 900°C series at high Ti percentage composition. This crystallographic phase exhibit intermediate particle sizes ranging from 5 to 17.6 nm as shown in tables 4.15 to 4.20 in appendix G. The particle size distribution of the Cu_3TiO_5 crystallographic phase is as shown in tables 4.2 to 4.19 in appendix G. The particle size values show that the polymorphic phase occurred across the whole calcination temperature range with a few obtained in the 900°C series. Particle sizes were intermediate throughout the series with extreme particle sizes observed in the 300°C series at 42 and

43nm at 45-50 % titanium composition respectively. The general particle size distribution dictates that orderly increase in the particle sizes of this phase occurs at both different temperatures and percentage composition. The particle sizes ranged from 5 to 19nm across the table.

The search-match of the PXRD peak patterns also identified unique and unexpected phases due to Ti and Cu that persistently occurred in the precursor powders. Tables 4.4 to 4.18 in appendix G show the particle size distribution of the two crystallographic phases respectively. The tables in appendix G and Figures 4.5 and 4.6 above show the occurrence and the particle sizes of the unknown non-stoichiometric Cu_xTi_yO phase. This phase occurred predominantly in the non-calcined series, a few in the 300°C series and none in the 500-900°C series. The most frequent particle size obtained is around 17 nm with a few having sizes between 6 - 10 nm as shown in the tables in Appendix G. The tables above also present the particle size distribution of the unknown Cu_xTi_yO non-stoichiometric crystallographic phase. It follows that this phase occurred only in the non-calcined and the 300°C series. The particle size ranged from 7 to 17 nm with most particles having a particle size around 16 nm and a few samples with sizes around 10 nm and 7 nm. The non-existence of this phase at higher temperatures dictates that the phase decomposed at temperatures above 300°C.

4.2. Phase Purity

The crystallographic phases identified in the PXRD analysis occurred on distinct peaks that distinguished them from other phases in the mixed metal oxides precursor powders. The PXRD peaks identifying each crystalline phase give details of the purity of that phase. This is because each PXRD peak is a product of the intensity of the diffracted X-rays from crystalline particles. Thus, the Particle size tables above and the PXRD analysis in the appendices show the phase purity of the crystallographic phases of the identified polymorphs. Tables 4.1 to 4.12 in appendix G show the particle sizes and occurrence of the phases of the respective polymorphs. It is noticeable that the PXRD analyses further support this phenomenon by giving the specific 2θ values at which these phases

occur in relation to other phases occurring in the same peak pattern. The anatase phase occurred at a different 2θ value as compared to the rutile phase. Their particle sizes measured at these peak positions were of the pure phases of these polymorphs. The difference in the particle sizes measured shows that one polymorphic phase had no influence on the morphology and crystalline state of another polymorph.

However, other peaks exhibited multi-phase occurrence in which more than one phase occurred at the same peak. This did not affect the measurement of particle size of these phases as the patterns were giving other peaks that were due to those phases at a different 2θ position. The major peak of the phase Cu_4O_3 was found at the same peak with tenorite at 2θ 35.5^o but its particle size was measurable at 2θ 58^o where the peak at that value was due to purely paramelaconite phase. The particle size tables in Appendix G shows the distribution of the crystallographic phases in the mixed metal precursor powders. The relative abundance of the respective phases was subject to the percentage composition of the respective metals in the mixture. However, these compositions did not show much influence on the variation of the particle sizes on the crystallographic phases. However, temperature had a direct effect on the particle size and hence phase purity since the occurrence of the phases was subject to their respective thermodynamic stability. It is this thermodynamic stability of the crystallographic phases that result in an unknown phase of $Cu_xTi_yO_z$ forming as shown in the figures and tables in the appendices.

Temperatures at which precursor powders were calcined determined the distribution of the crystalline phases of the polymorphs. Particle size analysis tables above shows that pure phases of anatase occurred at temperatures below 700°C, while above this temperature, the rutile polymorph forms. Similarly, the crystalline phases of copper oxide, ammonium copper chloride hydrate and iron titanium oxide produced pure phases at temperatures below 300°C. The pure polymorphic phase of copper titanium oxide (Ti_3Cu_3O) is thermodynamically stable at 900°C. Another phase Cu_3TiO_4, is thermodynamically unstable at 700°C while stable at all other calcination temperatures.

The pure phase of copper occurred a few times in the non-calcined series and none existent at higher temperatures because the copper is thermodynamically unstable such that it turns into the polymorphic forms of copper oxide.[79] The high temperatures render the pure copper to be reactive with oxygen forming the mixture of oxides including tenorite, cuprite, copper oxide and paramelaconite. This also continued to happen even in the presence of titanium. Thus, varying temperatures of calcination influenced the purification of phases with respect to their thermodynamic stability.[80]

Chapter 5: Results and Discussion

5.1. Transmission Electron Microscopy (TEM) Analysis

The TEM analysis gives provision for making detailed comparison of the characteristics and physical properties of nanosized crystallographic particles. The TEM images show the shapes of the crystallographic phases with their particle sizes measurable to the scale given.[10] This allows verification of the crystallites particle sizes to those determined from the X-Ray analysis of the XRD data. Figures 5.1 to 5.12 below are TEM images of the crystallographic phases synthesized using the resin-gel method of synthesis. It is noticeable that the shapes of the particles are varying due to composition variation of the precursor powders and the temperatures at which the powders were calcined. Hence, this analysis helps reveal the crystallographic transformation undergone by one crystallographic phase to another.

Observation from the TEM images reveals that all of the samples consist of nanocrystalline particles of Ti and Cu oxides. The size of the nanocrystalline particles increases with increasing calcination temperatures. The 500°C calcined sample contains nanoparticles of 12 +/- 6 nm in size as in images of Figure 5.3 whereas the 700°C calcined sample contains nanoparticles of a narrow anatase and rutile size range of 17 +/- 2 nm as in image Figure 5.7. As expected, the 900°C calcined sample consists of nanoparticles with the largest particle size of 40 +/- 3 nm as in Figure 5.1 image. This is in correspondence with the rutile phase identified in PXRD analysis in Section 3.2. Particle size analysis in Section 4.1 and data tables in Appendix G also confirm the effect of temperature on the particle size ranges observed in this analysis

TEM analyses revealed the formation of uniform particles, with an average size of about 17 nm and an accentuated tendency to form aggregates or agglomerates (Figure 5.6) irrespective of Ti or Cu content. The ceramic sample in Figure 5.9a calcined at 900°C exhibits a well densified, pore-free microstructure, with

bimodal grain distribution, consisting of both polyhedral, faceted, larger grains (of about 42 nm) and smaller grains of about 4 nm. As copper composition increases in relation to percentage Cu ratio, the small grain fraction increases progressively so that the ceramic with the highest ratio seems to be almost homogeneous as in Figure 5.7, a phenomenon attributable to presence of largely CuO and Cu_4O_3 phases.

The TEM image in Figure 5.6 clearly shows agglomerates of the synthesized material. The image of this sample shows localized surface fringes not confined to any particles that the crystallites are grossly of amorphous structure, although crystalline structure extending over nano or sub-nano dimensions existed.[83] However, the TEM image of the sample calcined at 300°C (Figure 5.2a) shows distinct particles of average crystallite size of 9-17 nm. The TEM image of this sample reveals sharp and clear lattice fringes indicating the good crystalline perfection of the calcined samples.

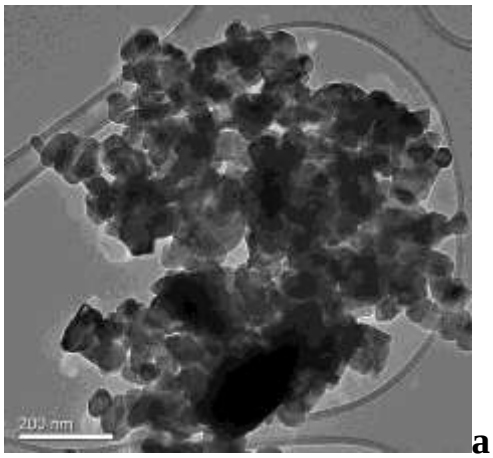

a

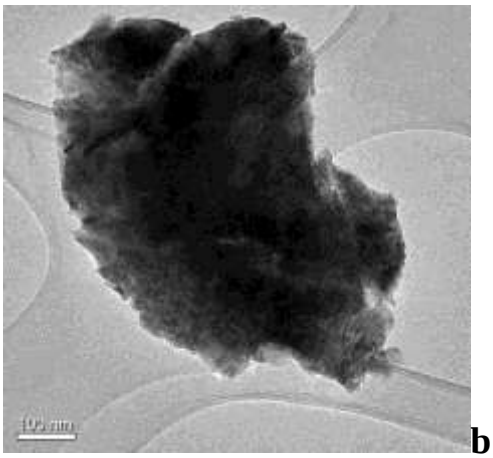

b

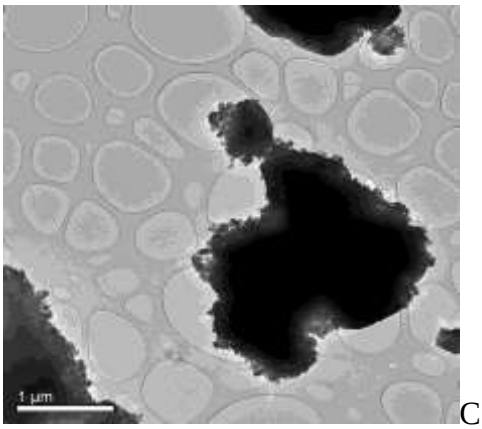

C

Figure 5.1: TEM images showing particles of a non-calcined sample with 0% Ti: 100% Cu composition. (a) high magnification image. (b) large concentration of the crystallites (c) large cluster of the nanoparticles agglomerate of the Tenorite phase (CuO).

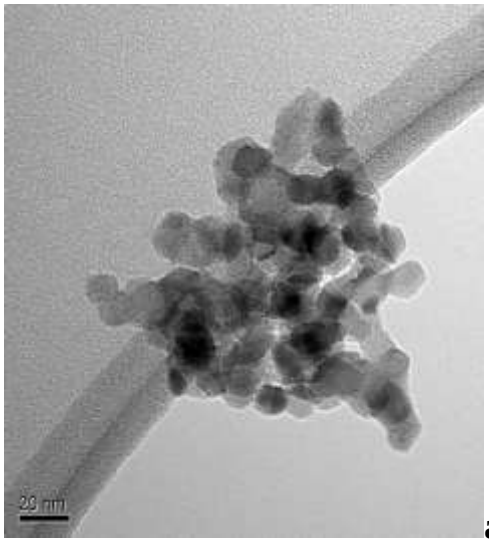

a

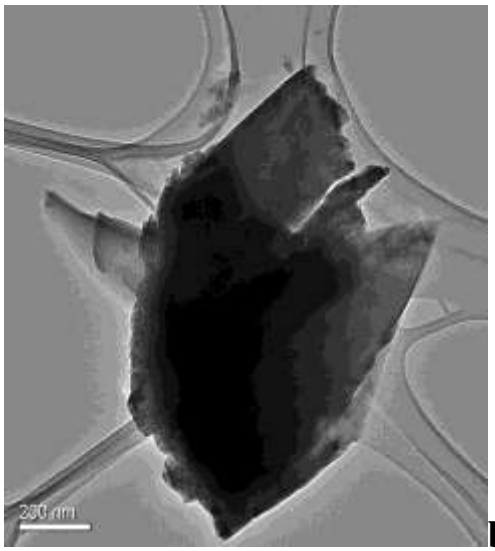

b

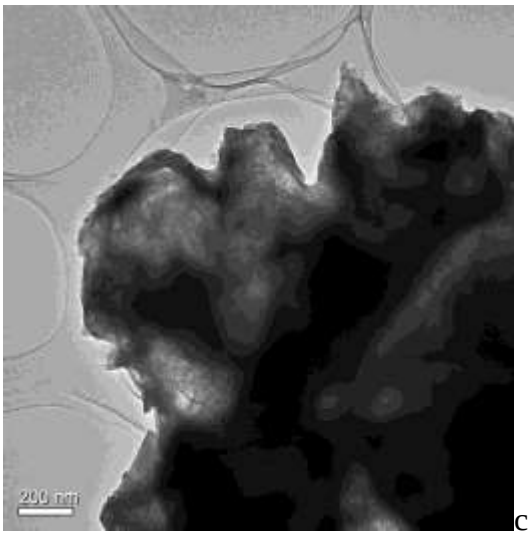

c

Figure 5.2: TEM images showing particles of a mixture of CuO and TiO_2 sample calcined at 300°C with 25% Ti: 75% Cu composition. (a) high magnification. (b) high concentration of the crystallites. (c) duplicate sample.

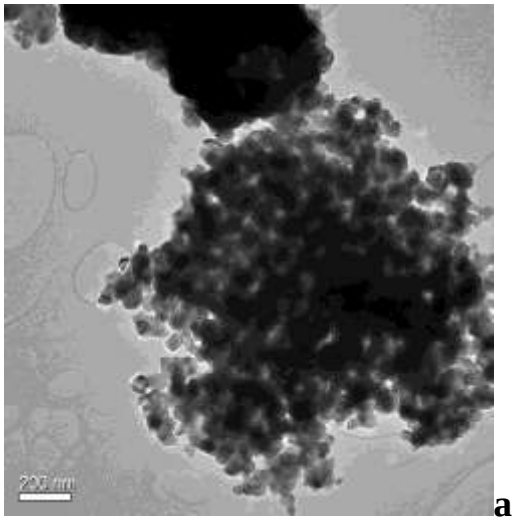

a

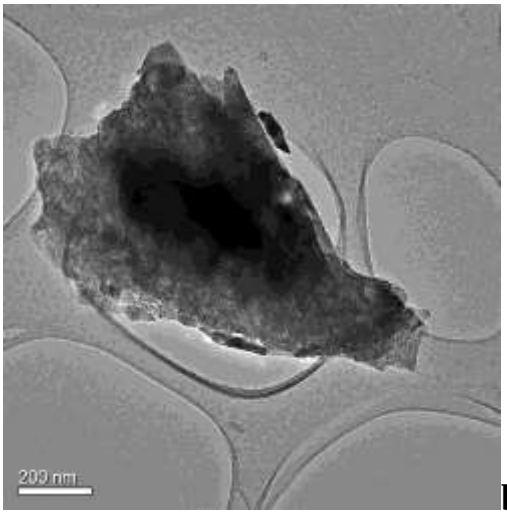

b

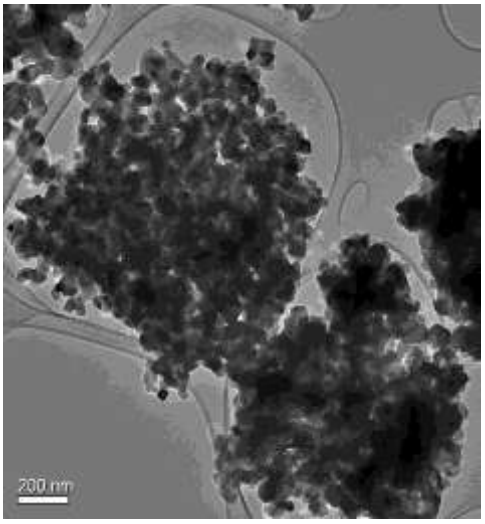

c

Figure 5.3: TEM images showing particles of a 500°C calcined sample of mixed metal oxides with 50% Ti: 50% Cu composition. (a) high magnification. (b) large particle concentration. (c) duplicate of the sample.

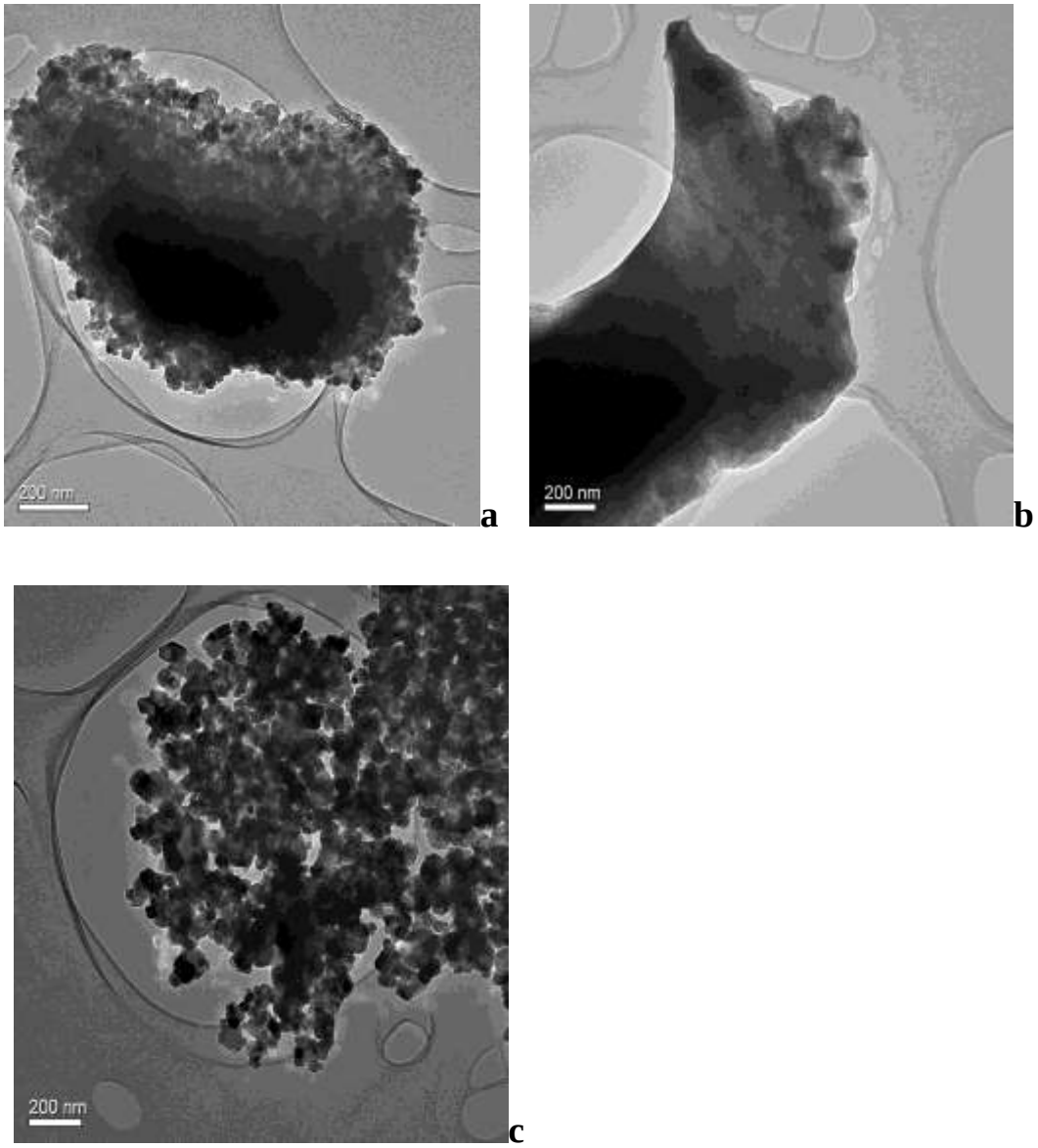

Figure 5.4: TEM images showing particles of a 700°C calcined sample of CuO and TiO_2 with 75% Ti: 25% Cu composition. (a) high magnification. Image (b) highly clustered particles (c) duplicate sample viewed at high magnification.

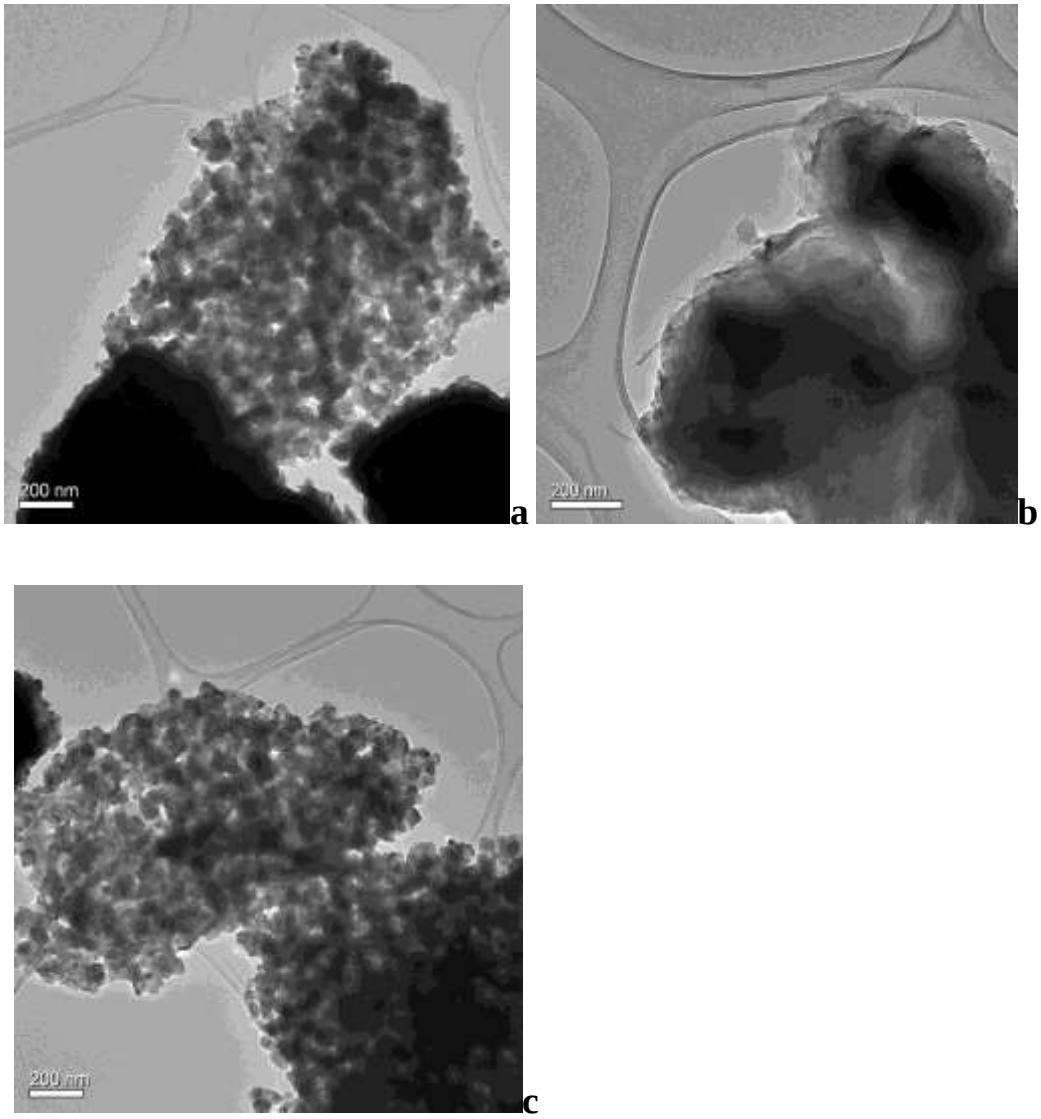

Figure 5.5: TEM images showing Rutile particles of a 900°C calcined sample with 100% Ti: 0% Cu composition. (a) high magnification. (c) replicate sample of the crystalline particles.

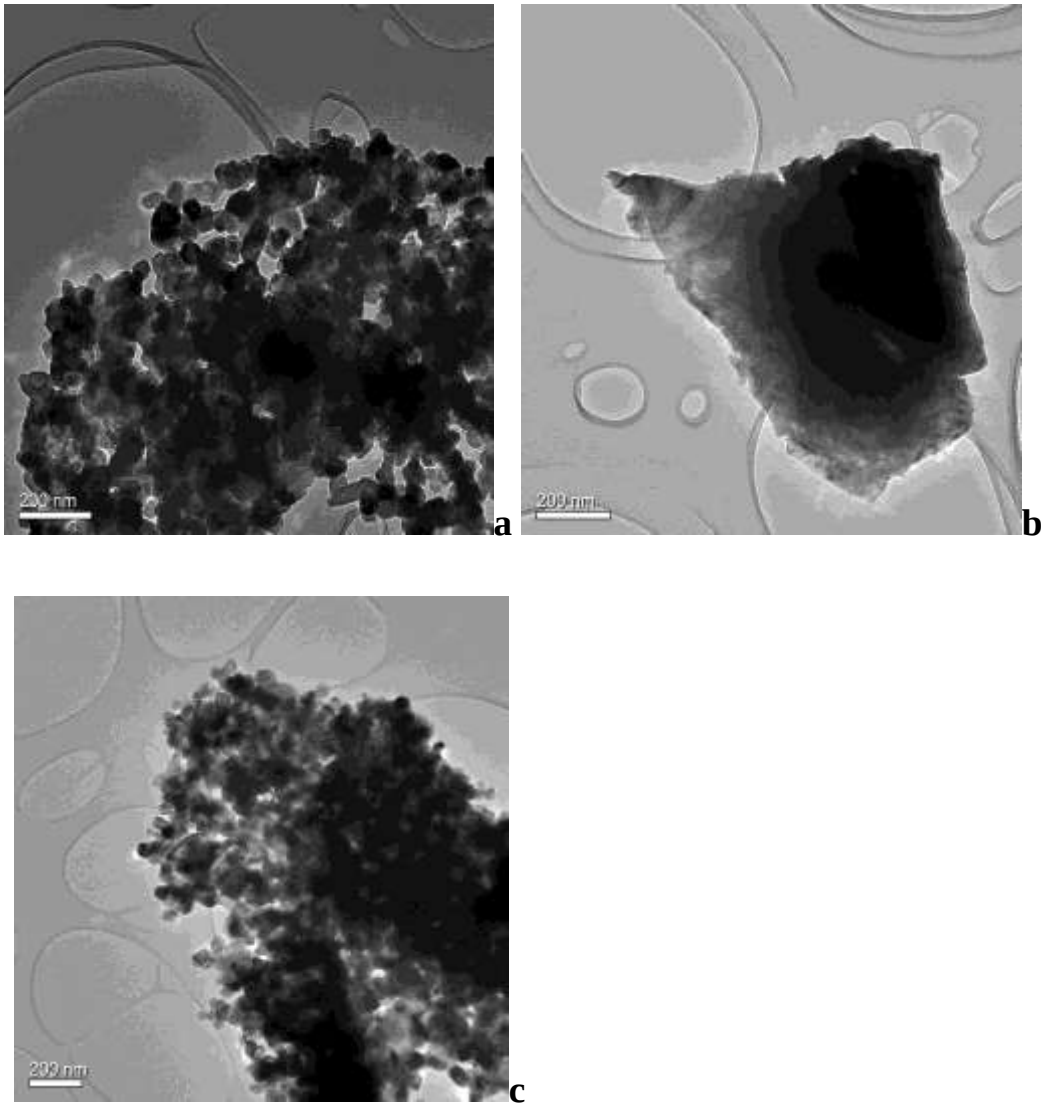

Figure 5.6: TEM images showing Anatase and CuO particles of a non-calcined sample with 45% Ti: 55% Cu composition. (a) crystalline particles at high magnification. (b) high particle concentration. (c) replicate sample.

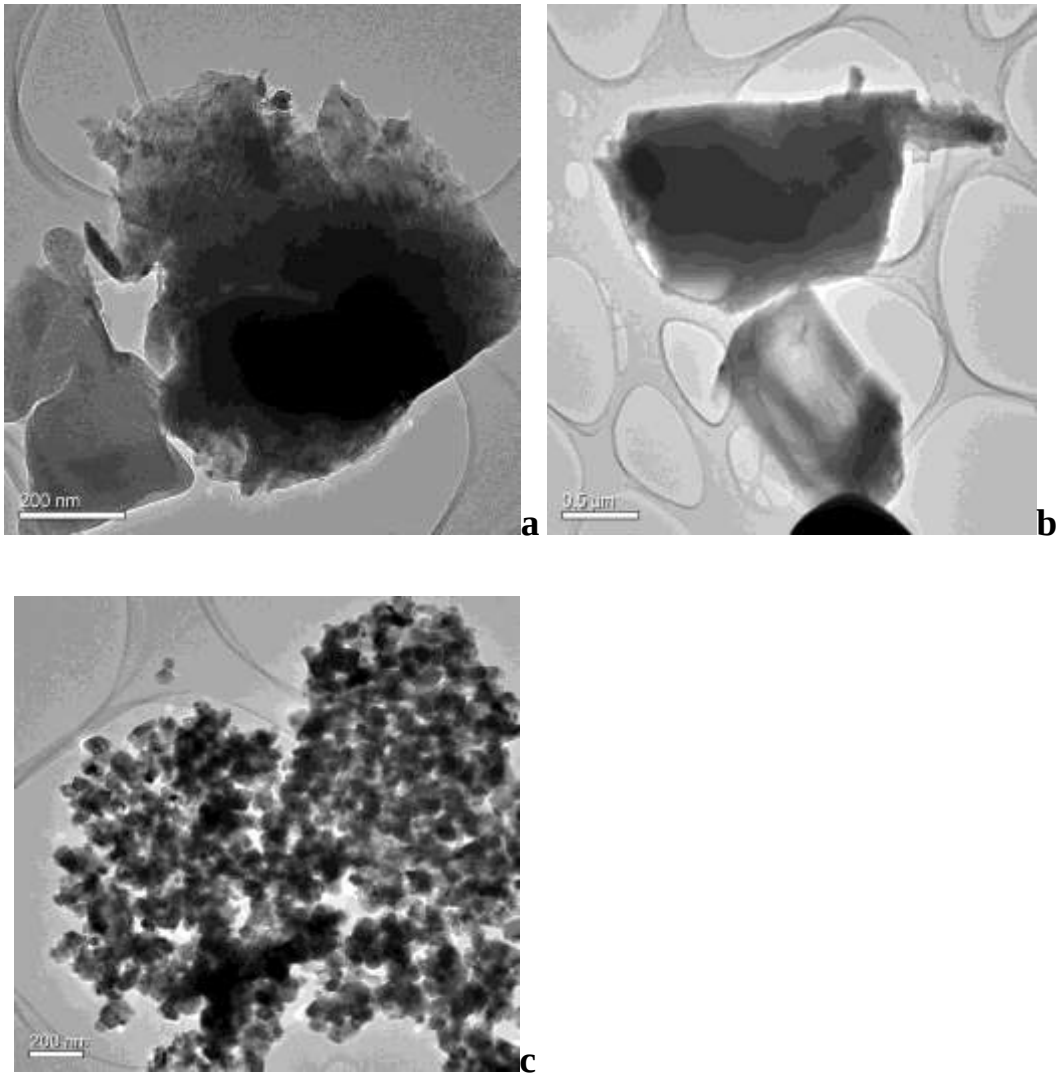

Figure 5.7: TEM images showing Anatase and CuO particles of a 300°C calcined sample with 30% Ti: 70% Cu composition. (a) nanoparticles in a cluster or agglomerate. (b) area of particles concentration. (c) duplicate sample of the precursor powders.

Figure 5.7 TEM images are showing particles of a 300°C calcined sample at 30% Ti: 70% Cu composition. In image 'a', the crystalline nanoparticles are in a cluster or agglomerate. In image 'b', the particles formed a large area of particle concentration. The image exhibit blocks of crystals because of the nature of the dominant crystallographic phase anatase. In image 'c', the replicate sample shows similar particles of the precursor powders. The image shows the nanorods conformation of the rutile-like particles due to the transformational temperatures that result in the extension of the atomic bonds in the rutile lattice.[84] This also correlates with the particle size data in the previous chapter that show the rutile phase occurring predominantly at temperatures above 700°C.

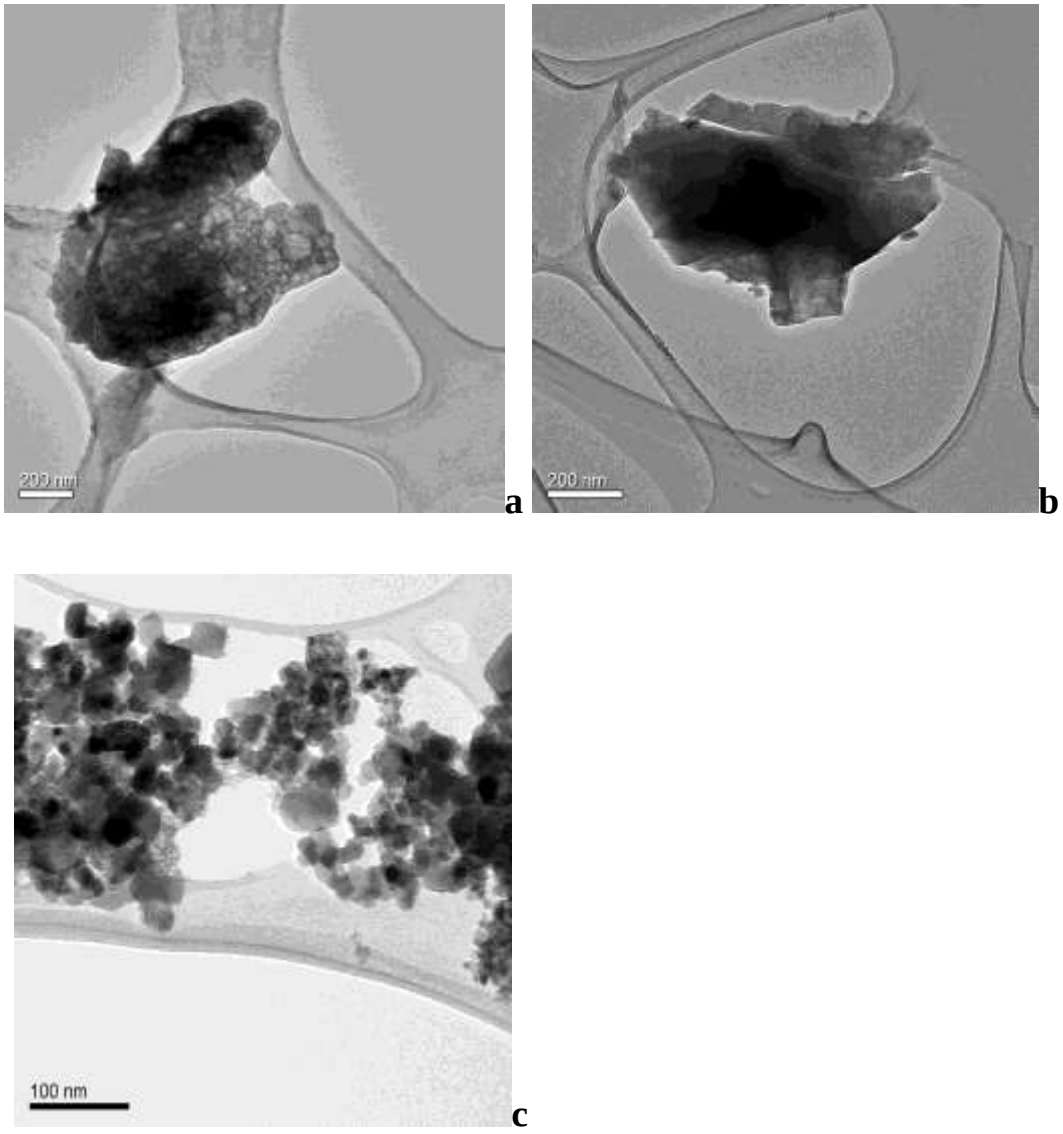

Figure 5.8: TEM images showing Rutile and Copper oxide particles of a 700°C calcined sample with 60% Ti: 40% Cu composition. (a) agglomerate of crystalline particles. (b) area of high concentration (c) duplicate sample.

Figure 5.8 TEM images are showing particles of a 700°C calcined sample at 60% Ti: 40% Cu composition. In image 'a', crystals formed a cluster or agglomerate of crystalline particles. In image 'b', there is another area of high concentration showing sharp edged sides of the crystal. Image 'c', is the replicate sample of the precursor powders. The image is at high magnification and shows the clear and clean crystals of the particles. Figure 5.9 TEM images are showing particles of a 900°C calcined sample at 85% Ti: 15% Cu composition. Image 'a', is the high magnification image of the crystalline polymorphs. The image shows the wide range of particle sizes exhibited by the phases in the particle size analysis table in

the previous chapter. Image ‘b’, is a representation of the high concentration of the particles in the sample. Image ‘c’, is the replicate sample of the precursor powders.

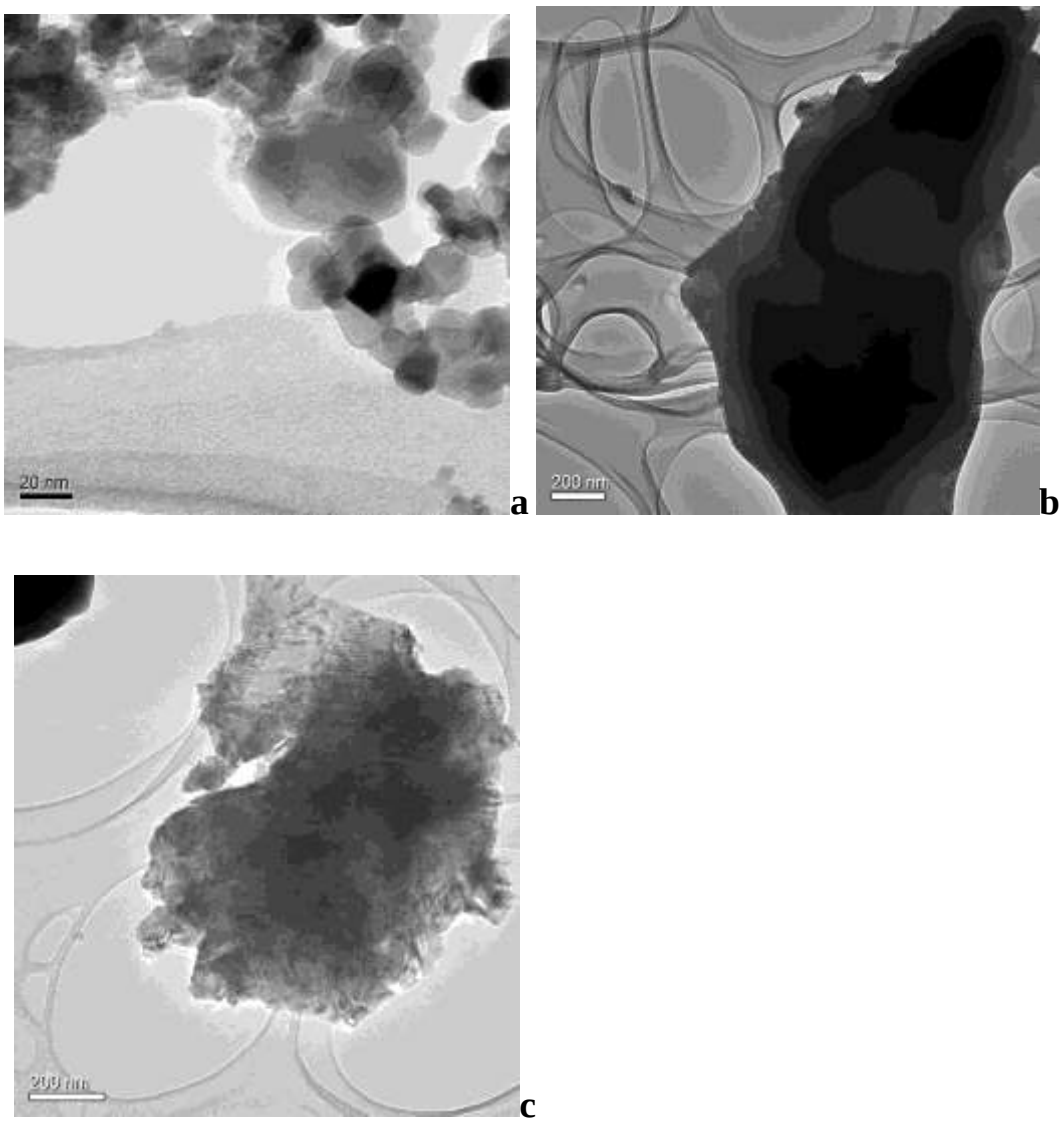

Figure 5.9: TEM images showing Rutile and CuO particles of a 900°C calcined sample with 85% Ti: 15% Cu composition. (a) high magnification image. (b high concentration of the particles (c) duplicate sample.

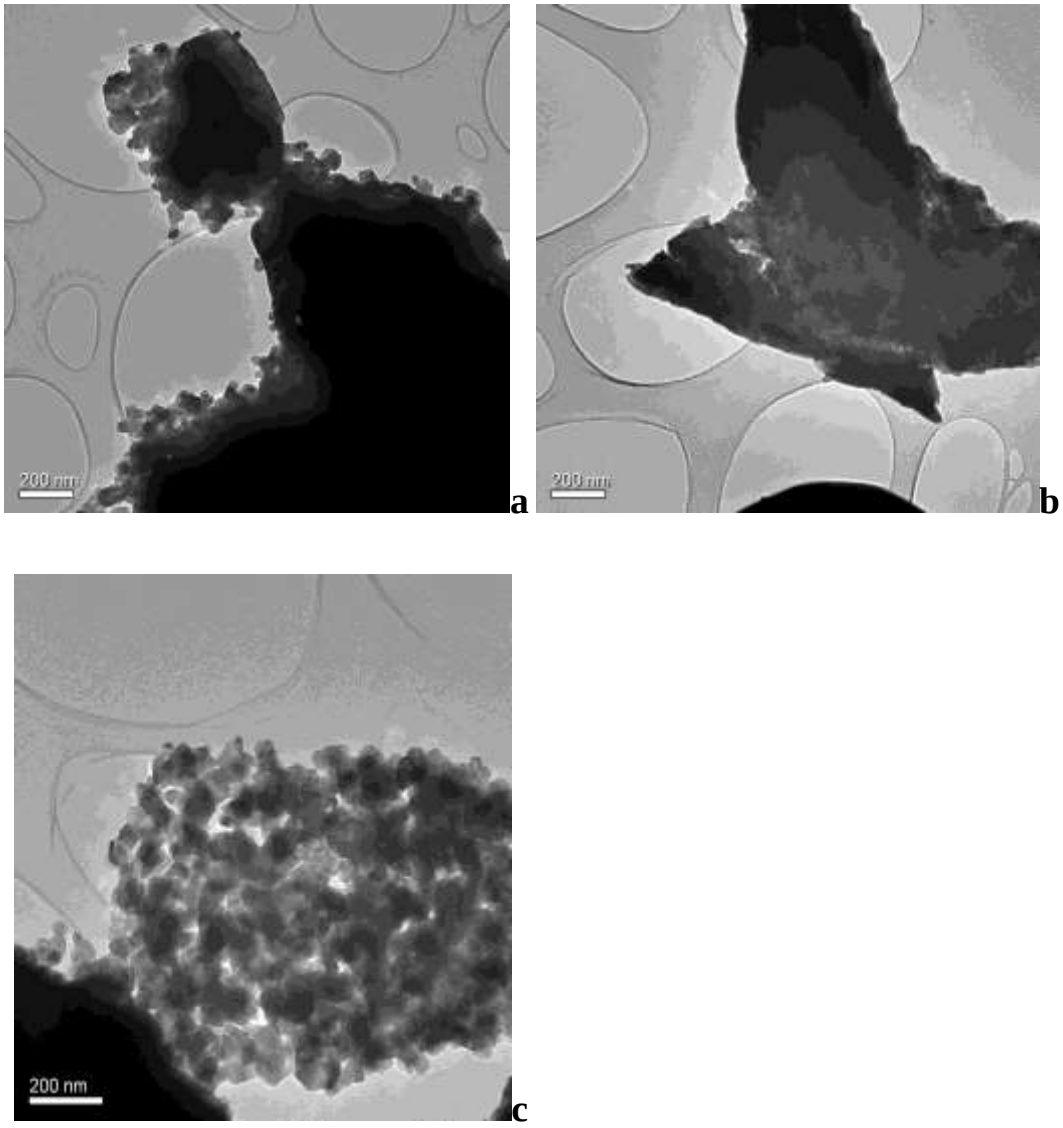

Figure 5.10: TEM images showing Anatase, Rutile and CuO particles of a 500°C calcined sample with 75% Ti: 25% Cu composition. (a) nanoparticle phases in the precursor powder of the sample. (b) high particle concentration of the crystalline phase. (c) duplicate sample of the precursor powders.

Figure 5.10 TEM images are showing particles of a 500°C calcined sample at 75% Ti: 25% Cu composition. Image 'a', is the representation of the nanoparticles in the precursor powder of the sample. The image shows a cluster of particles of relatively small size in confirmation with some of the particle size analysis data in the previous chapter. Image 'b', is an area of high particle concentration of the crystallographic polymorphs. Image 'c', represents the replicate sample of the precursor powders. This image is at high magnification and clearly shows the clean oxide particles.

Figure 5.11 TEM images are showing particles of a non-calcined sample at 90% Ti: 10% Cu composition. Image ‘a’, shows particles at high magnification. The image shows the small particle size of the crystallites. Image ‘b’, is the high concentration area of the crystallographic phases of particles. The image of the replicate sample is represented in image ‘c’. It shows similar structure and shape of the polymorph as in image ‘a’. Figure 5.12 TEM images showing particles of a non-calcined sample at 50% Ti: 50% Cu composition. Image ‘a’, shows the high concentration area of the crystalline particles. Image ‘b’, is a representation of the replicate of the precursor powder sample. The edges of the agglomerate are so Uneven.

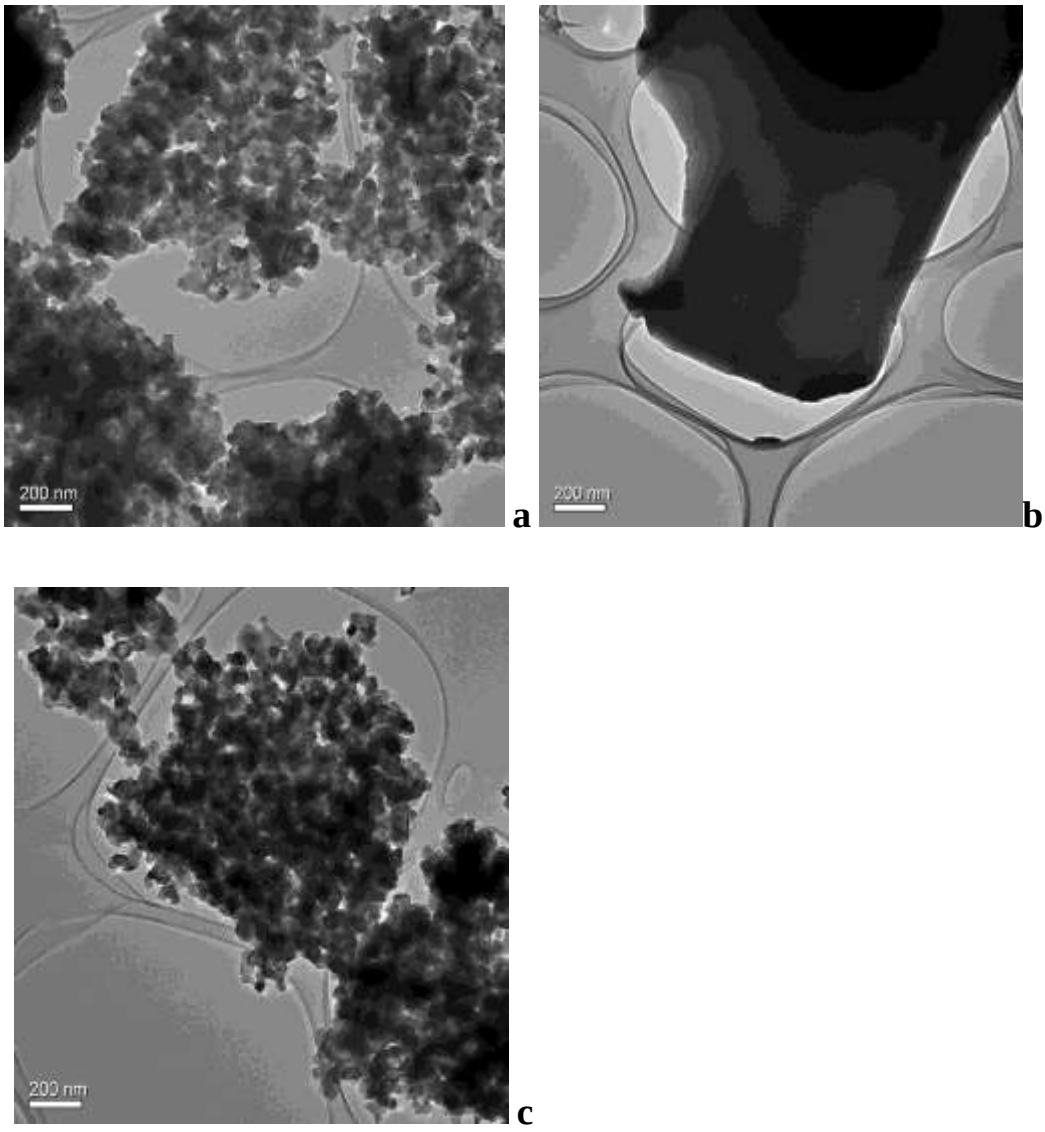

Figure 5.11: TEM images showing Anatase and CuO particles of a non-calcined sample with 90% Ti: 10% Cu composition. Image (a) shows particles at high magnification. (b) concentrated crystalline phases of particles. (c) duplicate sample.

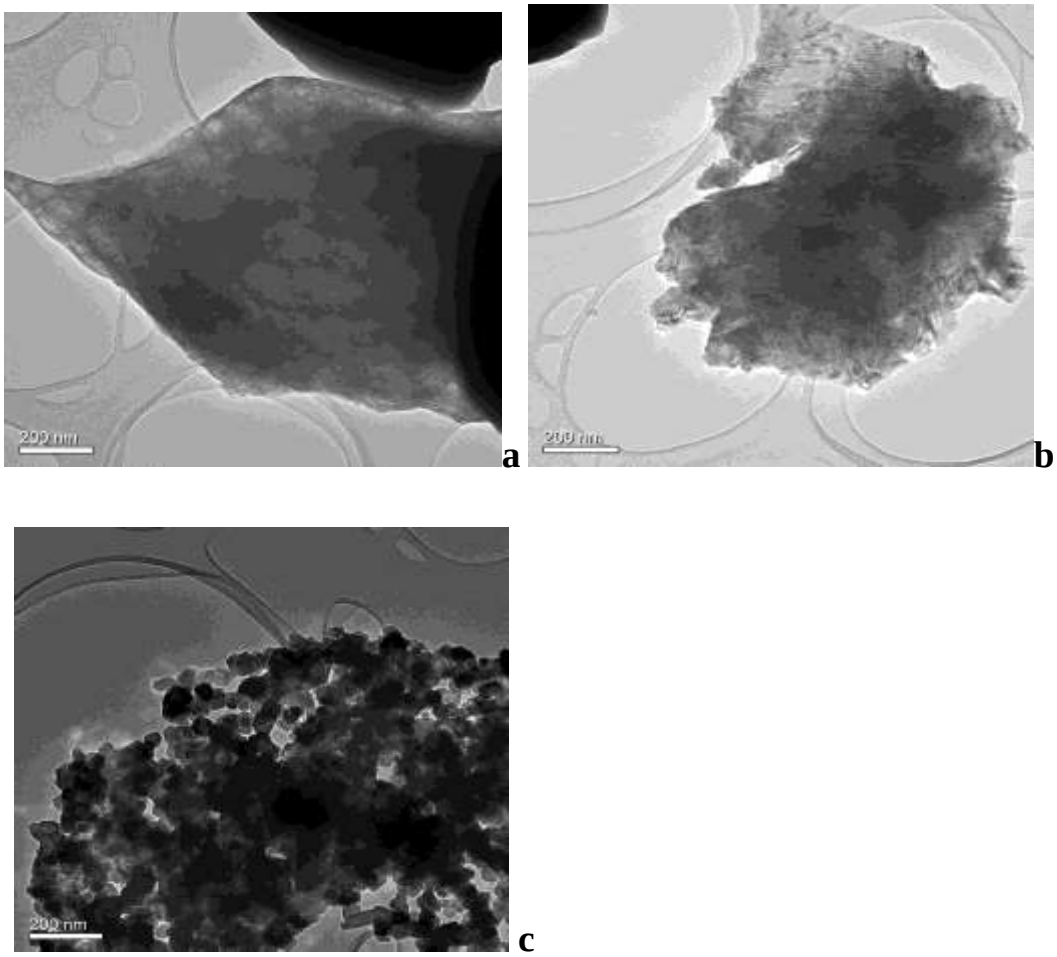

Figure 5.12: TEM images showing Anatase and CuO particles of a non-calcined sample with 50% Ti: 50% Cu composition image (a) high concentration area of the crystalline particles. (b) duplicate of the precursor powder sample. Image (c) is the high magnification image of the crystalline particles.

Image 'c', is the high magnification image of the crystallites of the polymorph. The particles seem to be of uniform size.

Chapter 6: Conclusion

The resin gel method of synthesis successfully produced a wide range of metal oxides by a hypothermal polymerizable complex method. Unfortunately, in the copper titanium oxides synthesized, the method was not good at producing pure phase of $Cu_xTi_yO_z$. The method described herein is based on the formation of a polymeric organic resin gel net intended to hold precursor metals in fixed positions in the gel. This prevents premature reactions and reduces any segregation of cations. Calcination of the precursor resin generated allowed rapid and random interaction of ions to obtain the precursor powders of mixed metal oxides. A dense multi-phase $Cu_xTi_yO_z$ product can be prepared by the hypothermal polymerizable complex method reaction using one pot resin – gel synthesis. Nanopowders obtained by the post-sintering open flame calcination accessed rapid ionic interactions of higher order and non-stoichiometric proportions.

The precursor gives rise to nano-crystalline phase pure $Cu_xTi_yO_z$ (CTO) powders with a crystallite size varying from 5 to 45 nm when heat treated up to 900 ^{0}C. The evolution of CTO phases with increasing temperature of calcining is associated with the changing stereochemistry of Cu (II) ions from distorted octahedral to a supressed tetrahedral and further to perovskite. The significant observation during the present studies is the coexistence of nearly flattened tetrahedral Cu (II) with those of square-planar coordination. Pure phases of metal oxides produced are the copper oxide polymorphs mainly Copper oxide (CuO), Cuprite (Cu_2O), Tenorite (CuO), Paramelaconite (Cu_4O_3) and pure copper (Cu). The titanium dioxide polymorphs produced are the Anatase and Rutile. Metal - metal oxide polymorphs of copper titanium oxide formed and these were of the forms Ti_3Cu_3O, Cu_3TiO_4 and Cu_3TiO_5. A possible formation mechanism of $Cu_xTi_yO_z$ is explained in section 3.1.1. Cu_4Ti possibly reacted with TiO to form Cu_3Ti_3O and Ti_2O reaction intermediate phases.

The mixtures of metal oxides were composed of pure phases of the respective polymorphs and their properties and characteristics were analyzed in details using XRD and TEM methods of analysis. The pure phases were obtained when Ethanol/PEG = 1, with a calcination of the precursor powder in the temperature range 300 to 900°C. Most oxides were obtained at temperatures below 700°C while other methods would require temperatures as high as 1050°C. The calcination time was only 1 hour as compared to 3 hours or longer in other methods of synthesis.

Structures of the nanosized phases were determined using XRD analysis method. The structures ranged from simple tetragonal to orthorhombic structure depending on the morphology and characteristics of the crystallographic polymorph. The crystallites of anatase, rutile, copper titanium oxide (Cu_3TiO_5), ammonium copper chloride hydrate and paramelaconite assumed the tetragonal structure. The copper oxide, titanium copper oxide (Ti_3Cu_3O) and cuprite crystalline phases assumed a cubic structure. The tenorite had a monoclinic structure while the copper titanium oxide (Cu_3TiO_4) had a hexagonal structure and the iron titanium oxide assumed an orthorhombic structure.

The smaller crystallite size obtained in the ethanol and PEG conditions may be due to the hydrophobic nature of the organic solvent as compared to water, which has a higher dielectric constant and hence hinders the growth of crystallites. Therefore, the resin gel method of synthesis can afford manipulation of a reaction mixture such that intended parameters such as desired product, particle size of products, crystallographic phase of crystallites and other morphological aspects can be predetermined and preset while the precursor metals are held in fixed positions in the resin gel. Altering the ratios of the Ethanol/PEG will change the way particles will crystallize and or the phases in which the crystallites will be in and hence provide a wide choice of materials that can be produced using this method. This phenomenon also help reduce temperatures at which materials can be produced at and lessen the calcination periods while getting the target product. This renders the method cheaper and quite effective in preparing ceramic materials such as mixed metal oxides with respect to other methods of synthesis.

Chapter 7: Further Research

Resin gel method proved to be a viable route in the preparation of nanopowders of mixed metal oxides. It has also shown that it can achieve synthesis of pure phases of crystalline particles at very low temperatures. Further research can be done on manipulating the resin-gel mechanism to access non-stoichiometric phases producible by this method and make new crystallographic ceramic materials that can be used in catalysis.

The hard wax left behind after slowly evaporating the solvent help hold the precursor metal ions in fixed positions before spontaneously heating it to combustion. Further research can be done on synthesizing nanoparticles of predetermined properties through altering the resin make-up. The percentage composition of the precursor metals can be altered to suppress the formation of one phase while favoring the formation of the other. The resin-gel itself can be moderated to see the influence of the ratios of the α-hydroxycarboxylic acid and the polyethylene glycol used in the polymerization process. Further detailed research can then be done to determine how the polybasic acid chelates determine the direction of reaction of the precursor metal ions held in the rein-gel.

Further research can also be done on the effect of solvent used in the preparation of the precursor powders. This will determine if solvents can undergo preliminary reactions with metal ions in the reaction mixture before formation of the resin-gel. Detailed analysis will seek to determine how these interactions of metal ions and different solvents influence access to Cu-Ti-O in pure phases.

HRTEM provides for multislice simulation on a sample and thus allows exhaustive description of the sample. The descriptions will be with reference to the atomic type and position of each atom in the structure and hence determining the slices projected potential and the propagation step geometrical parameters, which is a critical issue for large structures and for low-symmetry systems and

zone axes. Further research can be done on resin-gel method and use HRTEM and quantitative EDS to analyze compositions of individual particles. This is because HRTEM has a preliminary step on image simulation usually performed for semi-infinite structures considering the unit cell repetition along the axes that are normal to the zone axis. This approach simplifies the HRTEM multislice simulation input regarding the atoms information and allows the direct verification of thickness and defocus dependence on the contrast.

Further research can also be done on the resin-gel method in which variable temperature X-ray powder diffraction (VTPXRD) can be employed on the crystals. This analysis will be performed to evaluate diffraction pattern changes during crystallization of metal oxides from the amorphous to the stable polymorphic form A modification. VTPXRD closely analyze sample morphological transformations such that it shows the amorphous phase crystallizing via a transient metastable form B state that should show some differences in terms of the diffraction pattern, relative to the patterns obtained for forms A and C.

Lastly, it is apparent that in an attempt to synthesize pure phases of mixed metal oxide, unknown crystalline nanoparticle materials were synthesized. It follows that further research can be done to attempt to index the unknown materials. Success in indexing these unknown materials might help explain the morphological processes the metal ions went in the formation of metal oxides and their subsequent transformations through varied calcination temperatures.

References

1. Christina Bock, Helga Halvorsen and Barry MacDougal, Catal. Synth. Tech NRCC (2009)

2. Mariappan C. R., Galven C., Crosnier-Lopez M. P., Le Berre F., Bohnke O., J. Sol. State Chem, 179 (2006) 450 – 456

3. Aatiq A., Menetrier M., Croguenne L., Suard E., Delmas C., J. Mater. Sci. 12 (2002) 2971

4. Duward F. Shriver, P.W. Atkins and Cooper H. Langford, Oxford, New York 1990, Inorganic Chemistry 4^{th} Edn. 454

5. Haber J., Pure and Applied Chem, Vol. 63 9 (1991) 1227 – 1246

6. Xueyuan C., Wenquin L., Yongsheng L. and Guokui L., J. Rare Earth 25 (2007) p 515

7. Kun – Lin L., Mrityunjay S. and Rajiv A. Mater. Characterization 90 (2014) 40 – 51.

8. Keswani R. K., Harshad Chodke, Sarkar D., Khilar K. C. and Srinivasa R. S., J. Met. Eng and Mater. Sci 400076 (2010)

9. Verma K. C., Kotnala R. K., Mathpal M.C., Thakur N., Gautam P., Negi N. S., Mater. Chem. Phys 114 (2009) 576 – 579

10. Mêndeza M., Carvajala J. J., Cesterosb Y., Aguilôa M., Diaz F.16 (2010) E – 43007

11. Lee WC, Kwon OY, Kang CS. Microstructural characterization of interfacial reaction products between alumina and braze alloy. J Mater Sci 1995;30:1679–88.

12. Hao H, Wang Y, Jin Z, Wang X. Interfacial morphologies between alumina and silver–copper–titanium alloy. J Mater Sci 1997;32:5011–5.

13. Mandal S, Ray AK. Correlation between the mechanical properties and the microstructural behaviour of Al2O3–(Ag–Cu–Ti) brazed joints. Mat Sci Eng A 2004;383:235–44

14. Voytovich R, Ljungberg LY, Eustathopoulos N. The role of adsorption and reaction in wetting in the CuAg–Ti/alumina system. Scr Mater 2004;51:431–5.

15. P. J. Franklyn, D. C, Levendis, N. J. Coville, M. Mza, S. Afr. J. Chem., 60, 71 – 75 (2007)

16. Yu-Shu, Shen Bi-Shiou, and Chiou Chia-Cheng Ho [14] 517 (2008) 1209–1213.

17. L.C. Chang, D.Y. Lee, C.C. Ho, B.S. Chiou, Thin Solid Films 516 (2007) 45

18. Balachandran U. and Eror N. G., J. Sol. State Chem. 42 (1982) 276 – 282

19. Mascat J., Swany V. and Harrison N.M., Phys. Rev. B., 2002, 65, 2241 – 2

20. Fernandez-Garcia M., Martinez-Arials A., Hanson J.C. and Rodriguez J.A., Chem. Rev., 2004, 104, 4063 – 4104

21. Chen X.and Mao S., Chem. Rev., 2007, 107 2891 – 2959

22. Cotton F. A., Wilkinson G., Murrillo C.A. and Bochman M, Advanced Inorganic chemistry, John Wiley and Sons, 1999.

23. Hwu Y., Yao Y.D., Cheng N.F., C.Y. Tung and Lin M.H., Nanostructure. Mater. 1997, 9, 355

24. Zhang H. and Banfndield J.F., J. Mater. Chem. 1998, 8, 2073

25. Loehman RA, Tomsia AP. Joining of ceramics. Am Ceram Soc Bull 1988;67(2):375–80.

26. Suenaga S, Nakahashi M, Maruyama M, Fukasawa T. Interfacial reactions between sapphire and silver–copper–titanium thin film filler metal. J Am Ceram Soc 1997;80(2):439–44

27. Howard M., Rutile Paramorphs after Brookite, and Rutile Twins from Magnetic Core, Akansas, Heldref publications, 1999.

28. Aono H., Sugimoto E., Sadaoka Y., Imanaka N., Adach G., J. Electrochem. Sosci. 140 (1993) 1827 – 1832

29. http:// wikis.libs.nasu. edu/index.php/ bcc_and_hcp 2012-05-20

30. Hull, S. Rep. Prog. Phys, 2004, 67, 1233 - 1314

31. ruby.colorado.edu/~smyth/min/perovskites. Html 2012-05-20

32. Teraoka Y., Kakebayashi H., Morigushi I., Kagawa S., Chem. Lett 88 (1987) 673

33. Dharmaraj N., Park H.C., Kim C. K., Kim H.Y., Lee D. R., Mater. Chem. Phys 87 (2004) p 5

34. Rao, Can. J. Chem., 1961, 39, 498

35. Burger, Smoluchowski (John Wiley), New York and Chapman and Hall, London, 1957) Chap. 6

36. Rao, Turner and Honing, J. Physc. Chem. Solids, 1959, 11, 173

37. Rao and Lewis, Curr. Sci. (India), 1960, 29, 52

38. Barksdale, Titanium: Its°Ccurrence, chemistry and Technology (Ronald Press Co., New York, 1949)

39. Skinner, Johnston and Beckett, Titanium and its compounds (Herrich L. Johnston Enterprises, 1954), pp. 22 – 23

40. Schossberger, Z. Krist, 1942, 104, 358.

41. Gme;in, Handbuch der anorganischen chemie (Gmelin Institute, Verlag Chemie, Weinheim Germany, 1951), 41, pp. 233 – 34.

42. Jeremy K. BURDETT, Timothy Hughbanks, Gordon J. Miller, James W. Richardson Jnr, and Joseph V. Smith. J. Am. Chem. Soc. 1987, 109, 3639 – 3646

43. Encyclopedia.com http//www.encyclopedia.com/doc/1013 – perovskite model. Htlm

44. O'Keeffe, M. Acta Crystallorg, Sect. A. Cryst. Phys., Diffr., Theor, Gen. Crystallogr. 1977, A33, 924.

45. Forsyth J. B., Hull S., J. Phys., The effect of hydrostatic pressure on the anbient temperature structure of CuO., Condens. Matter 3(1991), 5257 – 5261, doi: 10.1088/0953 – 8984/3/28/001

46. Leal S. H. Sczancoski J. C., L. Cavalcante S., J. Sol-Gel Sci. Tech 53 (2010) 21 – 29

47. Escote M. T., J. Matos M. E., Santos M. R. M. C., J. Sol. State Chem. 40 (2009) 813 – 816

48. Teranishi T., M. Hosoe, Tanaka T., Miyake M., J. Phys Chem B 103 (1999) 3818

49. Li Z. F., Ge H. L., Zhong W. L., J. Cryst. Growth 294 (2006) 283 – 287

50. Longoni G., Chini P., Motoo S., J. Am. Chem. Soc 98 (1976) 7225

51. Mao Y., Tran T., Guo X., Huang J. Y., Shih C. K., Wang K. L. and Chang J. P., Adv. Func. Mater. 19 (2009) 745 – 758

52. Lui H., Wang L., Chen S. and Zou B., Lumin J. 126 (2007) p 459

53. Galceran M., Piyol M. C., Aguilo M. and Diaz F., Mater. Sci. Eng. B 146 (2008) P 7

54. Nazarov M., Kang J. H., Jeon D. Y., Bukesov S. and Akmaeva T., Opt. Mater. Chem. 27 (2005) 1576 – 1587

55. Richard I. Walton, Progress in Crystal Growth and Characterization of Materials 57 (2011) 93 – 108

56. Yan – Xiang Wang, Jian Sun, Xue Yun Fan, Xi Yu., Ceramics International 37(2011) 3431 – 3436

57. James R. Connolly, EPS 400 – 002, Introduction to X – Ray Powder Diffraction, Spring 2007

58. Bish, D. L., and Post, J. E., eds., 1989 Modern Powder Diffraction, Min. Soc. America Reviews in Mineralogy Vol. 20, 369p.

59. Buhrke, Victor E., Jenkins, Ron, and Smith, Dean K., eds, A Practical Guide for the preparation of Specimens for X – Ray Fluorescence and X – Ray Diffraction Analysis, John Wiley, 333p.

60. Valange S., Beauchaud A., Barrault J., Gabelica Z., Daturi M. and Can F., J. Catal. 251 (2007) p 113

61. Adelina Ianculescu, D. Berger, M. Viviani, C. E. Gomaga, L. Mitoserui, E. Vasile, N. Dragan, D. Crisan, J. Euro. Ceram. Society 27 (2007) 3655 – 3658

62. Takada K., Tansho M., Yanase I., Inanda T., Kajiyama A., Kouguchi M., Kondo S., Watanabe M., Solid State Ion. 139 (2001) 241 – 247

63. Pontes F. M., Longo E., Varela J. A., J. Sol- Gel Sci. Tech. 53 (2010) 21-29

64. Mercurio J. P., Manier M., Frit B., Mater. Lett. 8 (1989) p 112

65. Liu G., Chen X., Gschneidner K. A.Jnr, Eyring L., Handbook Phys and Chem of Rare Earth 37 (2007) 99 – 169

66. Yi – Jing Lin, Yen – Hwei Chang, Wein – Duo Yang, Bin – Siang Tsai, J. Non – Crst. Sol 352 (2006) 789 – 794

67. Harris Q. J., Taylor D. J., Flring P. F., Page R. A., Thin Solid Films 408 (2002) 346 – 352

68. Maher G. H., Hutchins C. E., Ross S. D., J. Mater. Proc. Tech. 56 (1996) 200

69. Pechini M. P., Pat U. S.. No. 3231328, Jan. 25 (1996)

70. Ailsa Allaby and Michael Allaby "perovskite model" A dictionary of Earth Science 1999

71. ruby.colorado.edu/~smyth/min/TEM. Html 2012-05-20

72. Ohno T, Sarukawa K, Matsumura M (2001) J Phys Chem B 105:2417

73. Anatase and Rutile Mineral Data

74. Sun J, Gao L, Zhang Q (2003) J Am Ceram Soc 86:1677

66. Fujihara K, Ohno T, Matsumura M (1998) J Chem Soc Faraday Trans 94:3705

67. Fujishima A, Honda K (1972) Nature 238:37

68. Linsebigler A, Lu G, Yates JT (1995) Chem Rev 95:735

69. Ni M, Leung M, Leung D, Sumathy K (2007) Renew Sustain Energy Rev 11:401

70. Wold A (1993) Chem Mater 5:280

71. Gratzel M (2005) Inorg Chem 44:6841

72. Huang SY, Schlichthorl G, Nozik AJ, Gratzel M, Frank AJ (1997) J Phys Chem B 101:2576

73. O'Regan B, Gratzel M (1991) Nature 335:737

74. Muggli DS, DIng L (2001) Appl Catal B 32:184

75. Fujishima A, Zhang X, Tryk DA (2008) Surf Sci Rep 63:515

76. Bessekhouad Y, Robert D, Weber JV (2003) Int J Photoenergy 3:153

77. Pozzo RL, Baltanas MA, Cassano AE (1997) Catal Today 39:219

78. Matthews RW (1987) J Phys Chem 91:3328

79. Okamoto K, Yamamoto Y, Tanaka H, Tanaka M (1985) Bull Chem Soc Jpn 58:2015

80. Baram N, Starosvetsky D, Starosvetsky J, Epshtein M, Armon R, Ein-Eli Y (2007) Electrochem Commun 9:1684

81. Carneiro JO, Teixeira V, Portinha A, Magalhaes A, Countinho P, Tavares CJ (2007) Mater Sci Eng B 138:144

82. Carp O, Huisman CL, Reller A (2004) Prog Solid State Chem 21:33

83. Franch M, Peral J, Domenech X, Ayllon JA (2005) Chem Commun 14:1851

84. Haick H, Paz Y (2001) J Phys Chem B 105:3045

85. Lee SK, McIntyre S, Mills A (2004) J Photochem Photobiol A 162:203

86. Mills A, Elliot N, Hill G, Fallis D, Durrant J, Willis R (2003) Photochem Photobiol Sci 2:591

87. Mills A, Hodgen S, Lee SK (2004) Res Chem Intermed 31:295

88. Mills A, Wang J, Crow M (2006) Chemosphere 64:1032

89. Paz Y, Heller A (1997) J Mater Res 12:2759

90. Sam ED, Urgen M, Tepehan FZ, Gunay V (2004) Key Eng Mater 264:407

91. Mills A, Lepre A, Elliott N, Bhopal S, Parkin IP, O'Neill SA (2003) J Photochem Photobiol A 160:213

92. Mitoraj D, Janczyk A, Strus M, Kisch H, Stochel G, Heczko PB, Macyk W (2007) Photochem Photobiol Sci 6:642

93. Kisch H, Burgeth G, Macyk W (2004) Adv Inorg Chem 56:241

94. Bacsa RR, Kiwi J (1998) Appl Catal B 16:19

95. Zhang Q, Gao L, Guo J (2000) Appl Catal B 26:207

96. Ranjit KT, Cohen H, Willner I, Bossmann S, Braun AM (1999) J Mater Sci 34:5273. doi:10.1023/A:1004780401030

97. Herrmann JM (1999) Catal Today 53:115

98. Sclafani A, Herrmann JM (1996) J Phys Chem 100:13655

99. Gaya UI, Abdullah AH (2008) J Photochem Photobiol C 9:1